Chapter 3

# Density-functional theory for electronic excited states

John M. Herbert
*Department of Chemistry and Biochemistry, The Ohio State University, Columbus, OH, United States*

## Chapter outline



## 3.1 Overview

Following its implementation in molecular quantum chemistry codes in the early 1990s *(1–6)*, density-functional theory (DFT) quickly emerged as the most popular tool for ground-state electronic structure calculations due to its favorable balance of relatively low cost with reasonable accuracy for thermochemistry. The first excited-state implementations quickly followed *(7–12)*, based on a linear-response (LR) formalism *(13–15)* that mirrors much earlier work on time-dependent Hartree-Fock (TDHF) theory *(16)*. The historical development of TDDFT has been summarized elsewhere *(17)*. The LR formulation is now known almost universally as "time-dependent" (TD-)DFT, despite its frequency-domain formulation and implementation. In its most pedestrian applications, LR-TDDFT produces vertical excitation energies for closed-shell molecules at ground-state geometries to within a statistical accuracy of ∼0.3 eV *(18)*, at a cost that is often only a few times more than the cost of the ground-state self-consistent field (SCF) calculation and possessing the same formal scaling *(19)*. This is a useful accuracy for electronic absorption spectra. In view of its low cost, LR-TDDFT has become the de facto method for computing electronic excitation spectra of finite molecular systems, although some fundamental problems remain in its application to periodic materials *(20–22)*. LR-TDDFT is also becoming increasingly popular for photochemical applications *(23–25)*, despite some problems with the description of conical intersections *(26–28)*. In part, this popularity is due to a growing recognition that complete active-space (CAS-)SCF methods cannot be considered quantitative approaches for excited-state dynamics *(29–32)*, due to a lack of dynamical electron correlation.

This chapter provides an overview of TDDFT and other DFT-based methods for computing excitation spectra, excited-state properties, and for simulating photochemical reactions, emphasizing theory rather than applications but with some molecular examples to motivate the discussion. For those unfamiliar with the formal underpinnings of TDDFT, a natural question to ask is "what does *time* have to do with excitation energies?" In fact, one knows from basic quantum mechanics that the time evolution of a nonstationary wave function encodes the system's excitation energies via the Bohr frequencies, $\omega_{jk} = (E_j - E_k)/\hbar$, therefore the time evolution of a quantum system can be used to extract excitation energies. The existence of a time-dependent extension of DFT is formally justified by the Runge-Gross theorem *(33–39)*, which provides something akin to a time-dependent extension of the first Hohenberg-Kohn theorem for the ground state *(40)*, that is, a density-to-potential mapping. In the time-dependent case, there are important caveats about initial-state dependence and memory effects *(41–43)*. Those issues have yet to be fully resolved in a computationally feasible way, but this has not stymied the practical development and application of TDDFT.

**Theoretical and Computational Photochemistry.** https://doi.org/10.1016/B978-0-323-91738-4.00005-1

Following a perturbation to the ground state, which creates a superposition of energy eigenstates, the Fourier components of the time-dependent dipole moment are precisely the Bohr frequencies. A Fourier transform of the dipole moment function is itself an absorption spectrum *(44)*,

$$I(\omega) = \frac{1}{2\pi}\int_{-\infty}^{+\infty} \langle \boldsymbol{\mu}(0)\cdot\boldsymbol{\mu}(t)\rangle e^{-i\omega t}dt \tag{3.1}$$

Excitation energies are also encoded in the isotropic frequency-dependent polarizability, $\alpha(\omega)$, which has a sum-over-states expression

$$\alpha(\omega) = \frac{e^2}{m_e}\sum_{n>0}\frac{f_{0n}}{\omega_{n0}^2 - \omega^2} \tag{3.2}$$

where $m_e$ is the electron mass, $\omega_{n0} = (E_n - E_0)/\hbar$, and

$$f_{0n} = \left(\frac{2m_e\omega_{n0}}{3e^2\hbar}\right)|\langle 0|\hat{\boldsymbol{\mu}}|n\rangle|^2 \tag{3.3}$$

is the dimensionless dipole oscillator strength for the $|0\rangle \rightarrow |n\rangle$ transition *(44)*. The poles of response function $\alpha(\omega)$ therefore encode excitation energies, with residues that encode oscillator strengths *(19)*. In the early days of quantum chemistry, Eq. (3.2) was actually used to compute excitation energies for atoms and atomic ions *(45, 46)*, by computing $\alpha(\omega)$ as the response to an applied field, and a version of this approach would eventually reappear in the form of "real-time" TDDFT *(47, 48)*. The poles of the Kohn-Sham response function also serve this purpose *(9, 49, 50)*, and the LR formalism applied to the Kohn-Sham ground state turns this idea into a robust computational paradigm, in the form of an eigenvalue-type problem for the excitation energies *(13–15)*. Although the LR formulation exists strictly in the frequency or energy domain, the time-dependent origins of the phenomenology are suggested in the name "TDDFT."

Despite its overwhelming popularity, LR-TDDFT excitation energies do tend to be more sensitive to the details of the exchange-correlation (XC) functional as compared to ground-state properties computed with DFT. In some sense, the statistical accuracy of ~0.3 eV that is quoted above should therefore be interpreted as representative of the best-case scenario with state-of-the-art functionals, and assuming that certain systemic pathologies can be avoided. LR-TDDFT may not be the theory that we want, but it remains the best theory that we have for excited states of large and even medium-sized molecules. This theory is introduced formally in Section 3.2 and that discussion constitutes the most substantial part of this chapter, just as LR-TDDFT occupies the most significant place among excited-state DFT methods. It holds that position because it is easy to use, not significantly more expensive than ground-state DFT, and provides a slew of excited states in an automated way, starting from a ground-state SCF solution.

While the accuracy of LR-TDDFT is often quite reasonable, certain systematic problems have been identified, and excited-state Kohn-Sham procedures have been developed to circumvent these. Rather than applying LR to the ground state, these methods look for an excited-state (non-*aufbau*) solution to the SCF equations, and for this reason the excited-state Kohn-Sham approach is often called a "ΔSCF" method. Although not formally justified by the Runge-Gross theorem, the ΔSCF approach has an admirable record of rectifying the deficiencies of LR-TDDFT, again at a cost comparable to that of a ground-state DFT calculation. What is lost in the ΔSCF approach is the ability to compute a whole spectrum of states at once, making the state-specific ΔSCF procedure much more labor intensive for the user. This approach is described in Section 3.3.

Finally, it is possible to take the time dependence in TDDFT at face value and to propagate Kohn-Sham molecular orbitals (MOs) in time, following a perturbation applied to the ground-state density. This is accomplished by solving the time-dependent Kohn-Sham (TDKS) equation,

$$i\hbar\frac{d}{dt}\psi_{k\sigma}(\mathbf{r},t) = \hat{F}_\sigma\psi_{k\sigma}(\mathbf{r},t) \tag{3.4}$$

which is a one-electron analog of the time-dependent Schrödinger equation. (Here, $\sigma \in \{\alpha, \beta\}$ is a spin index.) The one-electron effective Hamiltonian in Eq. (3.4) is the Fock operator $\hat{F}_\sigma$ that comes from the ground-state Kohn-Sham eigenvalue problem that determines the MOs:

$$\hat{F}_\sigma\psi_{k\sigma}(\mathbf{r}) = \varepsilon_k\psi_{k\sigma}(\mathbf{r}) \tag{3.5}$$

The "real-time" approach to TDDFT *(51, 52)*, which is described in Section 3.4, consists in solving Eq. (3.4) by propagating the MOs in time following a perturbation to the ground state that creates a time-evolving density,

$$\rho_\sigma(\mathbf{r},t) = \sum_k^{\text{occ}} |\psi_{k\sigma}(\mathbf{r},t)|^2 \tag{3.6}$$

expressed here for $\sigma$-spin electrons. (The total charge density is $\rho = \rho_\alpha + \rho_\beta$.) This approach can be used to simulate strong-field electron dynamics *(53)*, a topic of contemporary interest in attosecond molecular science *(54–57)*. It also provides a route to broadband spectra via Fourier transform of the time-dependent dipole moment function, in a direct realization of Eq. (3.1).

This chapter assumes a basis familiarity with ground-state DFT, as represented by the SCF eigenvalue problem in Eq. (3.5), which will serve as our starting point. It should therefore be familiar that the Fock operator takes the form

$$\hat{F}_\sigma = -\frac{1}{2}\hat{\nabla}^2 + v_{\text{ext}} + v_{\text{H}} + \hat{v}_{\text{xc}}^\sigma \tag{3.7}$$

in atomic units. The quantities $v_{\text{ext}}$, $v_{\text{H}}$, and $\hat{v}_{\text{xc}}^\sigma$ are known as the external, Hartree, and XC potentials, respectively. In the field-free case, the external potential is simply the interaction of the electrons with the nuclei *(58)*,

$$v_{\text{ext}}(\mathbf{r}) = -\sum_A \frac{Z_A}{\| \mathbf{r} - \mathbf{R}_A \|} \tag{3.8}$$

More generally, $v_{\text{ext}}(\mathbf{r})$ might also contain a field-dependent contribution such as $-\boldsymbol{\mathcal{E}}(\mathbf{r},t)\cdot\mathbf{r}$ in the presence of an electric field $\boldsymbol{\mathcal{E}}(\mathbf{r},t)$. The Hartree (or Coulomb) potential $v_{\text{H}}(\mathbf{r})$ describes self-repulsion of the electrons *(58)*, equivalent to what is often called "$J$" in Hartree-Fock theory *(40, 59)*. It is a functional of the density, given by

$$v_{\text{H}}[\rho](\mathbf{r}) = \int \frac{\rho(\mathbf{r},\mathbf{r}')}{\| \mathbf{r} - \mathbf{r}' \|} d\mathbf{r}' \tag{3.9}$$

The final component of $\hat{F}_\sigma$ is $\hat{v}_{\text{xc}}^\sigma = \delta E_{\text{xc}}/\delta\rho_\sigma$, the XC operator for $\sigma$-spin electrons. In "pure" Kohn-Sham theory, this quantity should be a local potential $v_{\text{xc}}^\sigma(\mathbf{r})$ rather than an operator, but herein we allow the possibility for mixing some nonlocal Hartree-Fock exchange (HFX), as is done in the hybrid density functionals that are most useful in molecular DFT. For hybrid functionals, $\hat{v}_{\text{xc}}^\sigma$ is a nonlocal operator and this scenario is sometimes called *generalized Kohn-Sham theory (39)*. Although inconsistent with the original Kohn-Sham paradigm, the use of hybrid functionals can no longer be considered exotic in contemporary molecular DFT.

The textbook by Koch and Holthausen *(40)* is a good resource for ground-state DFT (though not for TDDFT), as are several literature overviews *(58, 60)*. Updated ground-state benchmarks, relative to the rather dated ones in Ref. *(40)*, can be found elsewhere *(61, 62)*. For TDDFT, the textbook by Ullrich *(63)*, or else overviews by Gross and coworkers *(36, 64, 65)*, provide the rigorous foundations of the theory, which are mostly omitted here. Several other reviews cover LR-TDDFT in a pedagogical way *(66–68)*. For overviews of molecular applications of LR-TDDFT, see reviews by Jacquemin and coworkers *(69–73)*, who have also reviewed accuracy benchmarks *(18)* and functional selection *(74)*.

## 3.2 Linear-response ("time-dependent") DFT

This section describes the formalism and application of LR-TDDFT, commonly known simply as "TDDFT." The starting point is the TDKS equation (3.4) that describes how the ground-state MOs $\psi_{k\sigma}$ evolve in time following a perturbation that is applied at $t = 0$. If that perturbation is taken to be a time-oscillating field at frequency ω,

$$V(t) = \frac{1}{2}(\mathcal{E}e^{-\mathrm{i}\omega t} + \mathcal{E}^* e^{+\mathrm{i}\omega t}) \tag{3.10}$$

then in the weak-field limit ($\mathcal{E} \to 0$), the response of the ground state can be computed exactly using first-order perturbation theory *(15)*. Formally, one ought to show that the poles of the frequency-dependent response function can be obtained from those of the independent-particle (Kohn-Sham) response function *(9)*, but for that exercise the reader is referred to reviews by Marques and Gross *(64, 65)*. For a derivation of LR-TDDFT based on a variational principle, see Ref. *(75)*.

### 3.2.1 Theoretical formalism

The derivation from perturbation theory starts from the equivalent Liouville-von Neumann (LvN) form of the TDKS equation, which is

$$i\hbar \frac{d\hat{P}_\sigma}{dt} = \hat{F}_\sigma \hat{P}_\sigma - \hat{P}_\sigma \hat{F}_\sigma \tag{3.11}$$

where

$$\hat{P}_\sigma(t) = \sum_k^{\text{occ}} |\psi_{k\sigma}(t)\rangle\langle\psi_{k\sigma}(t)| \tag{3.12}$$

is the time-evolving one-electron density operator for $\sigma$-spin electrons. Expanding Eq. (3.11) to first order in the perturbed Fock and density matrices, in the presence of the perturbation $V(t)$, one obtains the unperturbed LvN equation at zeroth order. This is equivalent to the ground-state Kohn-Sham eigenvalue problem in Eq. (3.5). Working equations for LR-TDDFT are obtained by equating the first-order terms *(11, 15, 66)*, as elaborated below.

### 3.2.1.1 Linear-response theory

To consider this in more detail, recognize that the perturbation $V(t)$ in Eq. (3.10) is a one-electron operator whose spatial part can be expanded in the MO basis, leaving the time dependence to be carried by $e^{\pm i\omega t}$. Introducing a set of unknown coefficients $z_{pq\sigma}$ and $z^*_{qp\sigma}$, representing real and imaginary parts of the first-order response, the first-order perturbed density matrix can be expressed as

$$P_{pq\sigma}(t) = P^{(0)}_{pq\sigma} + P^{(1)}_{pq\sigma}(t) = P^{(0)}_{pq\sigma} + \frac{1}{2}(z_{pq\sigma}e^{-i\omega t} + z^*_{qp\sigma}e^{i\omega t}) \tag{3.13}$$

where $P^{(0)}_{pq\sigma}$ is the unperturbed density matrix at $t = 0$. This change in the density matrix is accompanied by a corresponding change in the Fock matrix. Through first order, the Fock matrix is *(11)*

$$F_{pq\sigma}(t) = F^{(0)}_{pq\sigma} + V_{pq} + \sum_{rs\tau}\left(\frac{\partial F_{pq\sigma}}{\partial P_{rs\tau}}\right)P^{(1)}_{rs\tau}(t) \tag{3.14}$$

where the unperturbed Fock operator $\hat{F}^{(0)}_\sigma$ has the form given in Eq. (3.7). The first-order response of the density matrix is thus coupled to a term of the form *(11)*

$$\begin{aligned}\frac{\partial F_{pq\sigma}}{\partial P_{rs\tau}} &= (p_\sigma q_\sigma|s_\tau r_\tau) + \left(p_\sigma q_\sigma\left|\frac{\delta^2 E_{\text{xc}}}{\delta\rho_\sigma\delta\rho_\tau}\right|s_\tau r_\tau\right) \\ &= (pq|sr) + (p_\sigma q_\sigma|\hat{f}^{\sigma\tau}_{\text{xc}}|s_\tau r_\tau)\end{aligned} \tag{3.15}$$

The first term, $(p_\sigma q_\sigma|s_\tau r_\tau) = (pq|sr)$, is a Coulomb integral expressed in Mulliken notation *(59)*, while $\hat{f}^{\sigma\tau}_{\text{xc}} = \delta^2 E_{\text{xc}}/\delta\rho_\sigma\delta\rho_\tau$. The latter quantity is discussed in more detail below.

So far, the MO indices $p, q, r, s$ are arbitrary and could refer either to occupied or virtual orbitals. In fact, the idempotency condition $\hat{P}^2_\sigma = \hat{P}_\sigma$ imposes restrictions. Through first order, the idempotency condition is

$$\sum_r (P^{(0)}_{pr\sigma}P^{(1)}_{rq\sigma} + P^{(1)}_{pr\sigma}P^{(0)}_{rq\sigma}) = P^{(1)}_{pq\sigma} \tag{3.16}$$

since $\hat{P}^{(0)}_\sigma\hat{P}^{(0)}_\sigma = \hat{P}^{(0)}_\sigma$. As a matrix, $\mathbf{P}^{(0)}_\sigma$ contains only occupied-occupied and virtual-virtual blocks because the occupied-virtual block vanishes as a condition of SCF convergence *(76)*. Using $i, j, \ldots$ to index occupied MOs and $a, b, \ldots$ for virtual MOs, this means $P^{(0)}_{ia\sigma} = 0 = P^{(0)}_{ai\sigma}$, so the constraint in Eq. (3.16) implies that the only nonvanishing coefficients in $P^{(1)}_{pq\sigma}$ are $z_{ia\sigma}$ and $z_{ai\sigma}$ *(11, 66)*. Conventional LR-TDDFT notation is obtained by relabeling these coefficients as

$$x_{ia\sigma} = z_{ai\sigma} \tag{3.17a}$$

$$y_{ia\sigma} = z_{ia\sigma} \tag{3.17b}$$

Collecting these unknowns into vectors $\mathbf{x}$ and $\mathbf{y}$, one may rewrite the first-order terms in the LvN equation in matrix form as *(66–68)*

$$\begin{pmatrix}\mathbf{A} & \mathbf{B} \\ \mathbf{B}^* & \mathbf{A}^*\end{pmatrix}\begin{pmatrix}\mathbf{x}^{(n)} \\ \mathbf{y}^{(n)}\end{pmatrix} = \omega_n\begin{pmatrix}\mathbf{1} & \mathbf{0} \\ \mathbf{0} & -\mathbf{1}\end{pmatrix}\begin{pmatrix}\mathbf{x}^{(n)} \\ \mathbf{y}^{(n)}\end{pmatrix} \tag{3.18}$$

This represents a system of equations for the excitation energies $\omega_n$ and the amplitudes $x_{ia\sigma}^{(n)}$ and $y_{ia\sigma}^{(n)}$, and constitutes the basic working equation of LR-TDDFT. (The index $n$, which enumerates excited states, will usually be omitted for compactness.) The system in Eq. (3.18) is often called the *Casida equation* (*13*, *14*), although it is formally identical to the equations of TDHF theory *(16)*. The matrices **A** and **B** are known as *orbital Hessians (19)*, for reasons that are discussed below, and they originate in the derivative of $\hat{F}_\sigma$ with respect to $\hat{P}_\tau$ in Eq. (3.15). In the canonical MO basis, the matrix elements of **A** and **B** are *(19*, *66)*

$$A_{ia\sigma,jb\tau} = (\varepsilon_{a\sigma} - \varepsilon_{i\sigma})\delta_{ij}\delta_{ab}\delta_{\sigma\tau} + (ia|jb) - \alpha_{\mathrm{hfx}}(ij|ab)\delta_{\sigma\tau} + (1-\alpha_{\mathrm{hfx}})(ia|\hat{\kappa}_{\mathrm{xc}}^{\sigma\tau}|jb) \tag{3.19a}$$

$$B_{ia\sigma,jb\tau} = (ia|bj) - \alpha_{\mathrm{hfx}}(ib|aj)\delta_{\sigma\tau} + (1-\alpha_{\mathrm{hfx}})(ia|\hat{\kappa}_{\mathrm{xc}}^{\sigma\tau}|bj) \tag{3.19b}$$

where $\hat{\kappa}_{\mathrm{xc}}^{\sigma\tau} = \hat{f}_{\mathrm{xc}}^{\sigma\tau} - \alpha_{\mathrm{hfx}}(\delta^2 E_{\mathrm{HFX}}/\delta\rho_\sigma\delta\rho_\tau)$. The quantity $\alpha_{\mathrm{hfx}}$ will be used throughout this chapter to mean the coefficient of HFX (often called "exact exchange") contained in the functional $E_{\mathrm{xc}}[\rho]$, with $0 \le \alpha_{\mathrm{hfx}} \le 1$. For example, $\alpha_{\mathrm{hfx}} = 0.2$ for B3LYP, meaning 20% HFX and 80% semilocal exchange. We have chosen to separate the HFX terms in Eq. (3.19), as these can be expressed in terms of electron repulsion integrals $(ij|ab)$ and $(ib|aj)$, leaving $\hat{\kappa}_{\mathrm{xc}}^{\sigma\tau}$ as the second functional derivative of the semilocal contribution $E_{\mathrm{xc}} - E_{\mathrm{HFX}}$.

The solution $(\mathbf{x}, \mathbf{y})$ of Eq. (3.18) parameterizes the *transition density matrix* for the excitation in question. In real space, this quantity is *(10*, *15*, *19)*

$$T(\mathbf{r},\mathbf{r}') = \sum_{ia\sigma}[x_{ia\sigma}\psi_{a\sigma}(\mathbf{r})\psi_{i\sigma}^*(\mathbf{r}') + y_{ia\sigma}\psi_{i\sigma}(\mathbf{r})\psi_{a\sigma}^*(\mathbf{r}')] \tag{3.20}$$

The unknowns **x** and **y** satisfy a bi-orthogonal normalization condition *(15)*,

$$\sum_{ia\sigma}(x_{ia\sigma}^2 - y_{ia\sigma}^2) = 1 \tag{3.21}$$

which is also a feature of the much older TDHF theory *(16)*. For historical reasons, TDHF is also known as the *random-phase approximation* (RPA) *(77*, *78)*, because it can be derived within an equation-of-motion formalism for the single-particle excitation operators *(68)*, similar to the historical RPA *(77)*. However, TDHF/RPA can also be considered as a special case of LR-TDDFT corresponding to the Hartree-Fock functional, that is, $\alpha_{\mathrm{hfx}} = 1$ and $\hat{\kappa}_{\mathrm{xc}}^{\sigma\tau} \equiv 0$.

The number of unknown amplitudes in Eq. (3.18) is $2n_{\mathrm{occ}}n_{\mathrm{vir}}$, hence to solve this equation for all of the excitation energies $\omega$ would incur sixth-order cost, $\mathcal{O}(n_{\mathrm{occ}}^3 n_{\mathrm{vir}}^3)$. Because matrix-vector products such as **Ax** or **By** can be computed with only fourth-order cost, in practice Eq. (3.18) is solved iteratively for just the lowest few ($n_{\mathrm{roots}}$) eigenvalues *(7*, *10*, *79–82)*. The cost of that calculation scales as $n_{\mathrm{roots}} \times \mathcal{O}(n_{\mathrm{occ}}^2 n_{\mathrm{vir}}^2)$ *(19)*, which is typically not significantly greater than the cost of the ground-state SCF calculation if $n_{\mathrm{roots}} \sim 10$. Therefore, if ground-state DFT is feasible then LR-TDDFT is probably tractable also, at least for the lowest few excited states. It is worth noting, however, that the memory footprint to solve Eq. (3.18) is $n_{\mathrm{roots}} \times \mathcal{O}(n_{\mathrm{occ}}n_{\mathrm{vir}})$, which is significantly more than the ground-state memory requirement. This can become a problem for large systems if a large number of excited states is desired, for example, in models of semiconductors, where a band structure is emerging *(83)*. For such applications, the real-time approach that is described in Section 3.4 offers a low-memory alternative to LR-TDDFT.

Some alternative forms of the basic LR-TDDFT equation are also worth considering. We first note that the matrices **A** and **B** in Eq. (3.19) can be rewritten as

$$A_{ia\sigma,jb\tau} = (\varepsilon_{a\sigma} - \varepsilon_{i\sigma})\delta_{ij}\delta_{ab}\delta_{\sigma\tau} + K_{ia\sigma,jb\tau} \tag{3.22a}$$

$$B_{ia\sigma,jb\tau} = K_{ia\sigma,bj\tau} \tag{3.22b}$$

where **K** is a coupling matrix *(13*, *84)*,

$$K_{ia\sigma,jb\tau} = \iint \psi_{i\sigma}(\mathbf{r})\psi_{a\sigma}(\mathbf{r})\left(\frac{1}{\|\mathbf{r}-\mathbf{r}'\|} + f_{\mathrm{xc}}^{\sigma\tau}(\mathbf{r},\mathbf{r}')\right)\psi_{j\tau}(\mathbf{r}')\psi_{b\tau}(\mathbf{r}')d\mathbf{r}d\mathbf{r}' \tag{3.23}$$

with a Hartree-XC kernel *(67)*. In practice, this looks like the energy-transfer coupling *(85)* between transition densities $\rho_{ia\sigma}(\mathbf{r}) = \psi_{i\sigma}(\mathbf{r})\psi_{a\sigma}(\mathbf{r})$ and $\rho_{bj\tau}(\mathbf{r}') = \psi_{b\tau}(\mathbf{r}')\psi_{j\tau}(\mathbf{r}')$. One can therefore consider that solution of the LR equations reveals how the zeroth-order, independent-particle excitations $\psi_{i\sigma} \to \psi_{a\sigma}$ are coupled to obtain excited states of the interacting system.

Assuming that the orbitals are real, so that $\mathbf{A}^* = \mathbf{A}$ and $\mathbf{B}^* = \mathbf{B}$, then Eq. (3.18) is equivalent to a pair of equations

$$(\mathbf{A} \pm \mathbf{B})(\mathbf{x} \pm \mathbf{y}) = \omega(\mathbf{x} \mp \mathbf{y}) \tag{3.24}$$

which makes it clear that Eq. (3.18) is not a conventional eigenvalue problem. However, upon introducing new variables

$$\mathbf{z}_\pm = \sqrt{\omega}(\mathbf{A} \mp \mathbf{B})^{-1/2}(\mathbf{x} \pm \mathbf{y}) \tag{3.25}$$

which satisfy the more conventional normalization condition $\mathbf{z}_\pm^\dagger \mathbf{z}_\pm = 1$ *(86, 87)*, the LR-TDDFT equation can be transformed into either of two equivalent, Hermitian eigenvalue problems *(81, 86–89)*. These are

$$\boldsymbol{\Omega}_\pm \mathbf{z}_\pm = \omega^2 \mathbf{z}_\pm \tag{3.26}$$

where

$$\boldsymbol{\Omega}_\pm = (\mathbf{A} \mp \mathbf{B})^{1/2}(\mathbf{A} \pm \mathbf{B})(\mathbf{A} \mp \mathbf{B})^{1/2} \tag{3.27}$$

The $\boldsymbol{\Omega}_+$ version of Eq. (3.26) is especially convenient for semilocal functionals ($\alpha_{\text{hfx}} = 0$), because in that case $\mathbf{A} - \mathbf{B}$ is diagonal and one obtains a Hermitian eigenvalue problem with half the dimension of the original pseudo-eigenvalue problem in Eq. (3.18).

For a closed-shell (spin-restricted) ground state, another important transformation is

$$x_{ia}^{\pm} = (x_{ia\alpha} \pm x_{ia\beta})/\sqrt{2} \tag{3.28a}$$

$$y_{ia}^{\pm} = (y_{ia\alpha} \pm y_{ia\beta})/\sqrt{2} \tag{3.28b}$$

which affords amplitudes for singlet (+) and triplet (−) spin functions. Making use of the unitary transformation *(78)*

$$\begin{pmatrix} \mathbf{A}+\mathbf{B} & \mathbf{0} \\ \mathbf{0} & \mathbf{A}-\mathbf{B} \end{pmatrix} = \frac{1}{2}\begin{pmatrix} \mathbf{1} & \mathbf{1} \\ -\mathbf{1} & \mathbf{1} \end{pmatrix}\begin{pmatrix} \mathbf{A} & \mathbf{B} \\ \mathbf{B} & \mathbf{A} \end{pmatrix}\begin{pmatrix} \mathbf{1} & -\mathbf{1} \\ \mathbf{1} & \mathbf{1} \end{pmatrix} \tag{3.29}$$

in addition to Eq. (3.28), one obtains singlet and triplet versions of $\mathbf{A} \pm \mathbf{B}$ that function as *stability matrices* (*7*, *8*, *86*). In other words, these are Hessian matrices whose eigenvalues characterize whether the ground state is stable with respect to orbital rotations. For example, the *singlet stability matrix* is *(86)*

$$(\mathbf{A}^+ + \mathbf{B}^+)_{ia,jb} = (\varepsilon_a - \varepsilon_i)\delta_{ij}\delta_{ab} + 4(ia|jb) + 2(ia|(\hat{f}_{\text{xc}}^{\alpha\alpha} + \hat{f}_{\text{xc}}^{\beta\beta})|jb) \tag{3.30}$$

A negative eigenvalue in $\mathbf{A}^+ + \mathbf{B}^+$ indicates an instability, which manifests as a negative excitation energy from the standpoint of LR-TDDFT. This is a consequence of the *Thouless theorem (90)*, which states that orbital rotations (and therefore orbital relaxation) can always be parameterized as single excitations. Along similar lines, eigenvalues of the *triplet instability matrix (86)*

$$(\mathbf{A}^- + \mathbf{B}^-)_{ia,jb} = (\varepsilon_a - \varepsilon_i)\delta_{ij}\delta_{ab} + 2(ia|(\hat{f}_{\text{xc}}^{\alpha\alpha} - \hat{f}_{\text{xc}}^{\alpha\beta})|jb) \tag{3.31}$$

indicate whether the ground-state solution is stable with respect to spin-symmetry breaking (restricted → unrestricted relaxation) *(91)*. In the presence of an unstable reference state, the transformation in Eq. (3.25) may become problematic, which can lead to failure of certain iterative LR-TDDFT algorithms.

### 3.2.1.2 Adiabatic approximation

We have not yet discussed the key ingredient in the orbital Hessian matrices that makes LR-TDDFT different from TDHF/RPA, namely, the *exchange-correlation kernel*, $\hat{f}_{\text{xc}}^{\sigma\tau}$. A more careful application of LR theory would note that the quantities $\mathbf{A}(\omega)$ and $\mathbf{B}(\omega)$ are themselves functions of the excitation energy $\omega$ *(13–15)*. In wave function terms, this can be understood based on the fact that any exact theory of many-electron excitation energies that is formulated as an effective single-particle theory must ultimately invoke an effective Hamiltonian that is energy dependent, in order to encapsulate the effects of higher-order excitations *(14, 92, 93)*. (In many-body theory, this energy-dependent contribution is sometimes called the "self-energy" *(94)*.) Proof-of-concept models for an energy-dependent kernel $f_{\text{xc}}^{\sigma\tau}(\mathbf{r}, \mathbf{r}', \omega)$ have been put forward *(42, 43, 93, 95)*, which have close connections to many-body perturbation theory and the Bethe-Salpeter equation *(92, 93)*. However, there are no production models for molecular Hamiltonians at present.

To appreciate the nature of the approximation that is made by neglecting the energy dependence of $\hat{f}_{\mathrm{xc}}^{\sigma\tau}$, consider that this quantity arises in Eq. (3.15) as the second functional derivative of the XC energy with respect to the density, or the first derivative of the XC potential. For a time-evolving density $\rho_\sigma(\mathbf{r}, t)$, this means *(41)*

$$f_{\mathrm{xc}}^{\sigma\tau}(\mathbf{r}, \mathbf{r}', t - t') = \frac{\delta \hat{v}_{\mathrm{xc}}^{\sigma}[\rho](\mathbf{r}, t)}{\rho_\tau(\mathbf{r}', t')} \tag{3.32}$$

(This expression leaves $\hat{v}_{\mathrm{xc}}^{\sigma}$ in the form of an operator, which technically makes this an example of generalized Kohn-Sham theory *(39)*.) The time dependence in $f_{\mathrm{xc}}^{\sigma\tau}(\mathbf{r}, \mathbf{r}', t - t')$ means that this quantity depends on the whole history of the time evolution of the density *(41–43)*, imparting a frequency dependence upon Fourier transformation: $f_{\mathrm{xc}}^{\sigma\tau}(\mathbf{r}, \mathbf{r}', \omega)$. For practical purposes, it is basically a requirement to invoke the *adiabatic approximation* (*13*, *68*, *96)*, which assumes locality in time and therefore differentiates with respect to the instantaneous density *(13)*:

$$\frac{\delta \hat{v}_{\mathrm{xc}}^{\sigma}[\rho](\mathbf{r}, t)}{\rho_\tau(\mathbf{r}', t')} \approx \delta(t - t') \frac{\delta \hat{v}_{\mathrm{xc}}[\rho](\mathbf{r})}{\rho_\tau(\mathbf{r}')} \tag{3.33}$$

The "memory" of the kernel is thereby neglected, tantamount to assuming that $\hat{v}_{\mathrm{xc}}[\rho](\mathbf{r}, t)$ can be approximated using a conventional ground-state energy functional $E_{\mathrm{xc}}[\rho]$, whose functional derivative is evaluated using the time-evolving density *(96)*:

$$\hat{v}_{\mathrm{xc}}^{\sigma}(\mathbf{r}, t) = \left.\frac{\delta E_{\mathrm{xc}}[\rho]}{\delta \rho_\sigma(\mathbf{r})}\right|_{\rho_\sigma(\mathbf{r}) = \rho_\sigma(\mathbf{r}, t)} \tag{3.34}$$

Time dependence is thus carried entirely by the density and not by the functional. The frequency dependence of $\hat{f}_{\mathrm{xc}}^{\sigma\tau}$ disappears and conventional (ground-state) density functionals are all that is required for LR-TDDFT within the adiabatic approximation.

One immediate ramification of this approximation is that the LR-TDDFT equation has precisely $2n_{\mathrm{occ}}n_{\mathrm{vir}}$ solutions for the excitation energy $\omega$, coinciding with the number of unknown amplitudes $x_{ia\sigma}$ and $y_{ia\sigma}$. In wave function language, these are the "one-particle, one-hole" (1p1h) states, as in conventional configuration interaction with single excitations (CIS). States with significant double-excitation character (2p2h states) are either absent altogether *(95–99)*, or at best severely shifted *(98)*. The latter are therefore generally considered to be out of reach within the adiabatic approximation to LR-TDDFT that is ubiquitous in practical calculations *(99)*.

### 3.2.1.3 Tamm-Dancoff approximation

Given a ground-state functional $E_{\mathrm{xc}}[\rho]$, all that is required for LR-TDDFT within the adiabatic approximation are second functional derivatives

$$\hat{f}_{\mathrm{xc}}^{\sigma\tau}(\mathbf{r}, \mathbf{r}') = \frac{\delta^2 E_{\mathrm{xc}}}{\delta \rho_\sigma(\mathbf{r}) \delta \rho_\tau(\mathbf{r}')} \tag{3.35}$$

from which the matrix elements of $\mathbf{A}$ and $\mathbf{B}$ can be evaluated. Upon solution of Eq. (3.18) or one of its equivalent forms, it is often found that the amplitudes $y_{ia\sigma}$ are $10^2$–$10^3$ times smaller than the largest $x_{ia\sigma}$. Invoking the approximation $y_{ia\sigma} \approx 0$, one obtains a conventional Hermitian eigenvalue problem

$$\mathbf{A}\mathbf{x} = \omega\mathbf{x} \tag{3.36}$$

whose dimension is half that of the original LR-TDDFT pseudo-eigenvalue problem, and where the matrix $\mathbf{B}$ does not appear. The basis for this approximation can be understood from the fact that the matrix elements of $\mathbf{A}$ are typically much larger (at least along the diagonal) as compared to the matrix elements of $\mathbf{B}$, because the leading contribution to $\mathbf{A}$ is a difference in one-particle energy levels ($A_{ia\sigma,ia\sigma} = \varepsilon_{a\sigma} - \varepsilon_{i\sigma} + \cdots$). For historical reasons that are related to a similar approximation that is made in nuclear physics *(63)*, neglect of $\mathbf{y}$ is known as the *Tamm-Dancoff approximation* (TDA). For hybrid functionals, the reduction in dimension leads to a concomitant reduction in cost although for semilocal functionals the same reduction in dimensionality can be achieved using the $\boldsymbol{\Omega}_+$ version of Eq. (3.26).

For the Hartree-Fock functional ($\alpha_{\mathrm{hfx}} = 1$ and no correlation), Eq. (3.36) is equivalent to the CIS eigenvalue equation *(100)*. Excited-state wave functions in CIS are linear combinations of singly excited Slater determinants $|\Psi_{i\sigma}^{a\sigma}\rangle$,

$$|\Psi\rangle = \sum_{i}^{\mathrm{occ}} \sum_{a}^{\mathrm{vir}} \sum_{\sigma} x_{ia\sigma} |\Psi_{i\sigma}^{a\sigma}\rangle \tag{3.37}$$

and for this reason we identify the variables $x_{ia\sigma}$ as excitation amplitudes. The neglected amplitudes $y_{ia\sigma}$ represent deexcitation, insofar as TDHF/RPA was originally introduced in the nuclear and many-body physics literature as a means to add correlation to the ground state *(16, 77)*. In fact, LR-TDDFT in the form of Eq. (3.18) was introduced in molecular quantum chemistry as the "DFT random-phase approximation" *(101, 102)*. For that reason, solution of Eq. (3.18) or its equivalents, *without* invoking the TDA, is sometimes called "RPA." However, in view of a resurgence of interest in using the RPA formalism as a means for correlating the ground state *(103–110)*, it is better to refer to Eq. (3.18) as "full" LR-TDDFT, if there is a need to distinguish it from the TDA version in Eq. (3.36).

Quantitatively, the impact of the TDA on excitation energies is often <0.1 eV *(11)*, though a potentially detrimental impact is that oscillator strengths within the TDA no longer satisfy the Thomas-Reiche-Kuhn sum rule *(44)*, namely,

$$\sum_{n>0} f_{0n} = N \tag{3.38}$$

This constraint is satisfied by the full LR-TDDFT approach, at least in the complete-basis limit *(13, 15, 111)*. Some small-molecule tests suggest that errors incurred by the TDA are relatively mild (<15%) *(112)*, and perhaps not noticeable in band shapes once vibrational broadening is taken into account *(113)*.

A more important consequence of the TDA is that it decouples the excitation energy problem from the ground-state stability problem, whereas for full LR-TDDFT a triplet instability in the ground state manifests as a negative excitation energy, or as an imaginary root of the Hermitian eigenvalue problem in Eq. (3.26). This may cause problems for eigensolvers that implicitly assume $\omega > 0$. Note that triplet instabilities are associated with spin-symmetry breaking, that is, with the emergence of an unrestricted solution that is lower in energy than the restricted solution. Where they appear, these instabilities cause significant artifacts in potential energy surfaces computed using LR-TDDFT, including the appearance of spurious cusps *(84, 114–117)*. In contrast, the variational nature of the CIS-type equation, as opposed to the pseudo-eigenvalue problem that characterizes full LR-TDDFT, prevents this from happening within the TDA *(68)*.

Along similar lines, it has been appreciated for a long time that TDHF specifically is prone to triplet instabilities *(90, 91, 118–124)*. In fact, the appearance of imaginary excitation energies at equilibrium geometries of small molecules led Furche and Ahlrichs to conclude that this method is "rather useless... for the investigation of excited potential energy surfaces" *(125)*. In contrast, spin-symmetry breaking near the equilibrium geometry is often significantly mitigated when DFT is substituted for Hartree-Fock theory *(126)*. Because most molecular LR-TDDFT calculations use hybrid functionals that include some fraction of HFX, it can be expected that problems with triplet instabilities may increase as that fraction increases, which is precisely what is found in practice *(127–131)*. Similarly, in calculations using range-separated functionals, which incorporate HFX at long range in the Coulomb potential, these instabilities are sensitive to the length scale on which that mixing is introduced *(132–137)*. Invoking the TDA thus improves the accuracy of triplet excitation energies *(134–136)*. For photochemical problems, where exploration of excited-state potential energy surfaces is paramount, Casida et al. suggest that the TDA is effectively mandatory *(138)*, in order to avoid excitation energies that drop to zero (and then become imaginary) as the system moves through a Coulson-Fischer point where spin-symmetry breaking occurs. Furthermore, instabilities appear to proliferate as one moves away from the ground-state geometry on an excited potential surface *(138–140)*. For example, in the photochemical ring-opening reaction of oxirane ($C_2H_4O$), 51% of configuration space is estimated to exhibit an instability with semilocal DFT, as compared to 93% of space with B3LYP *(138)*.

### 3.2.1.4 Analytic gradients

Photochemical simulations require analytic excited-state gradients. That formalism, which is closely connected to response theory for optical properties *(141)*, is not discussed here but can be found elsewhere *(19, 125, 142–145)*. Nonadiabatic or "derivative coupling" vectors between excited states *(27, 146)*, which are needed for nonadiabatic molecular dynamics simulations *(23–27)*, have also been formulated *(147–154)*. Evaluation of the nonadiabatic couplings has the same formal complexity as evaluation of the excited-state gradient *(25, 147)*.

The gradient formalism also bears on static properties of the excited state, such as the dipole moment or atomic population analysis. The density matrix for the excited state can be written as

$$\mathbf{P}_{\text{rlx}} = \mathbf{P}_{\text{unrlx}} + \mathbf{Z} = \mathbf{P}_0 + \Delta\mathbf{P} + \mathbf{Z} \tag{3.39}$$

which is sometimes called the "relaxed" density matrix, with $\mathbf{P}_{\text{unrlx}} = \mathbf{P}_0 + \Delta\mathbf{P}$ as the "unrelaxed" contribution. Here, $\mathbf{P}_0$ represents the ground-state density matrix and the unrelaxed change upon excitation ($\Delta\mathbf{P}$) can be obtained from the amplitudes $\mathbf{x}$ and $\mathbf{y}$. The remaining contribution ($\mathbf{Z}$) represents orbital relaxation *(19, 144, 145)*.

The unrelaxed density change $\Delta\mathbf{P}$ can be separated into particle (electron) and hole contributions,

$$\Delta\mathbf{P} = \Delta\mathbf{P}^{\text{elec}} + \Delta\mathbf{P}^{\text{hole}} \tag{3.40}$$

which are given by *(125, 145, 155, 156)*

$$\Delta\mathbf{P}^{\text{elec}} = \frac{1}{2}[(\mathbf{x}+\mathbf{y})^{\dagger}(\mathbf{x}+\mathbf{y}) + (\mathbf{x}-\mathbf{y})^{\dagger}(\mathbf{x}-\mathbf{y})] \tag{3.41a}$$

$$\Delta\mathbf{P}^{\text{hole}} = -\frac{1}{2}[(\mathbf{x}+\mathbf{y})(\mathbf{x}+\mathbf{y})^{\dagger} + (\mathbf{x}-\mathbf{y})(\mathbf{x}-\mathbf{y})^{\dagger}] \tag{3.41b}$$

These expressions can be rearranged to afford *(155)*

$$(\Delta\mathbf{P}^{\text{elec}})_{ab\sigma} = \sum_{i}(x^{*}_{ia\sigma}x_{ib\sigma} + y^{*}_{ia\sigma}y_{ib\sigma}) \tag{3.42a}$$

$$(\Delta\mathbf{P}^{\text{hole}})_{ij\sigma} = -\sum_{a}(x_{ia\sigma}x^{*}_{ja\sigma} + y_{ia\sigma}y^{*}_{ja\sigma}) \tag{3.42b}$$

Note that $\Delta\mathbf{P}$ only contains occupied-occupied ($\Delta\mathbf{P}^{\text{hole}}$) and virtual-virtual ($\Delta\mathbf{P}^{\text{elec}}$) contributions to the excited-state density matrix, not occupied-virtual contributions. The latter are contained in $\mathbf{Z}$ *(19, 125)*, the evaluation of which requires solution of so-called *Z*-vector equations *(157)*. This has the same formal complexity as an excited-state gradient calculation.

Excited-state properties should be computed using the relaxed density matrix $\mathbf{P}_{\text{rlx}}$, because $\Delta\mathbf{P}$ and $\mathbf{Z}$ make similar contributions *(100, 158, 159)*. Especially when the change in density is large, as for an excitation with significant charge-transfer (CT) character, the use of the unrelaxed density matrix may lead to unacceptable errors in excited-state properties. For example, excited states of *p*-nitroaniline involving intramolecular CT character exhibit relaxed and unrelaxed dipole moments (computed using $\mathbf{P}_{\text{rlx}}$ vs. $\mathbf{P}_{\text{unrlx}}$, respectively) that differ by more than 10 D in some cases *(158)*!

### 3.2.2 Performance and practice

As discussed earlier, the formal scaling of LR-TDDFT is $n_{\text{roots}} \times \mathcal{O}(n^{4}_{\text{basis}})$ for hybrid functionals *(19)*. In practical terms, where only a few low-lying excited states are desired, this means that LR-TDDFT is generally feasible if the corresponding ground-state calculation is practical, perhaps up to about 400 atoms for single-point calculations or 150–250 atoms for excited-state geometry optimization *(70, 71)*, with more severe limitations for excited-state frequency calculations *(71, 160)*. These estimates are appropriate where basis sets of double-$\zeta$ quality are used, which is generally adequate. Triple-$\zeta$ basis sets may be considered to be converged *(67)*. This section provides an overview of other practical considerations in LR-TDDFT calculations, including selection of an XC functional. Techniques for visualizing and understanding the excited states are also discussed.

#### *3.2.2.1 Restriction of the excitation manifold*

Significant cost reduction in LR-TDDFT calculations for large molecules can be achieved by neglecting some of the amplitudes $x_{ia\sigma}$, in addition to neglecting *all* of the amplitudes $y_{ia\sigma}$. Fig. 3.1 shows examples of excitation spectra computed for $C_{60}$ and for $C_{119}H_{154}ClN_{21}O_{40}$, performed by excluding over 70% of the virtual orbitals (based on orbital energies $\varepsilon_{a\sigma}$), without adverse effects on the spectral envelope *(161)*.

Similar truncations of the excitation manifold can be used to access core-excited states *(162–165)*. There is significant interest in core excitations in contemporary quantum chemistry *(164–169)*, driven by the recent availability of tabletop laser sources with femtosecond time resolution *(170–174)*. However, core-to-valence excitations lie embedded in an ionization continuum and, at a practical level, lie above all of the valence-excited states, such that the use of iterative eigensolvers is prohibitively expensive if the spectrum must be computed starting from the lowest excitation energies. By retaining only those amplitudes $x_{ia\sigma}$ for which $i$ is a core orbital on the atom of interest, core-excited states emerge as the smallest eigenvalues and can be computed directly. This "frozen-valence occupied" approximation has historically been called *core-valence separation (175–177)*, and it introduces negligible error for K-edge excitations where $\psi_{i\sigma}$ is a 1s orbital *(177)*. Another strategy to access core-level excitations is energy windowing *(162, 178)*, in which the amplitudes $x_{ia\sigma}$ are excluded unless $\varepsilon_{a\sigma} - \varepsilon_{i\sigma}$ lies within the window of interest.

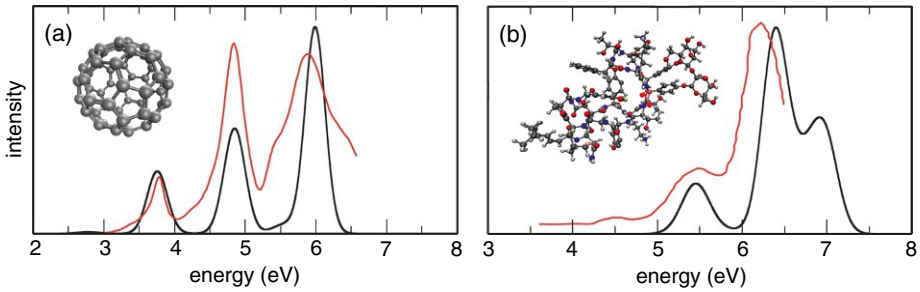


**FIG. 3.1** Electronic absorption spectra of (A) $C_{60}$ (PBE/6-31G* level) and (B) the antibiotic ramoplanin (271 atoms and 2483 basis functions, CAM-B3LYP/6-31G* level). Thin curves represent the experimental spectra and thick curves are computed from LR-TDDFT/TDA excitation energies with 0.2 eV Gaussian broadening. Core orbitals and 70% of virtual orbitals are excluded from each calculation. *(Adapted from Hanson-Heine, M. W. D.; George, M. W.; Besley, N. A. Assessment of Time-Dependent Density Functional Theory Calculations With the Restricted Space Approximation for Excited State Calculations of Large Systems. Mol. Phys.* **2018,** *116, 1452–1459, under a CC BY License.)*

### 3.2.2.2 Exchange-correlation functionals

Before considering the accuracy of LR-TDDFT, it is useful to introduce a paradigm for classifying various density-functional approximations, for which we use the taxonomy of "Jacob's ladder" *(179–181)*. At each rung on this metaphorical ladder, the functional dependence of $E_{xc}$ grows more intricate, incorporating more sophisticated functionality depending on the density, its gradients, the Laplacian, etc.: $E_{xc}[\rho_\sigma, \hat{\nabla}\rho_\sigma, \hat{\nabla}^2\rho_\sigma, \tau_\sigma, \{\psi_{a\sigma}\}]$. In a statistical sense (and *only* in a statistical sense), it is true that the best functionals on the higher rungs of the ladder outperform the best functionals on the lower rungs *(61, 182)*. These rungs map onto various inputs $\rho_\sigma, \hat{\nabla}\rho_\sigma, \hat{\nabla}^2\rho_\sigma, \ldots$ as follows.

- *Rung 1: Local density approximation (LDA)*. The baseline LDA functional comes from the uniform electron-gas model in which $E_{xc}$ is a functional of $\rho(\mathbf{r})$ only, or of $\rho_\alpha(\mathbf{r})$ and $\rho_\beta(\mathbf{r})$ if the system is spin-polarized. This approach does not afford useful accuracy for molecular quantum chemistry, with errors of 60–100 kcal/mol for atomization energies *(61, 183)* and ~20 kcal/mol for barrier heights *(61)*.
- *Rung 2: Generalized gradient approximations (GGAs)*. This class of functionals includes a dependence on the density gradients $\hat{\nabla}\rho_\sigma(\mathbf{r})$. These are often called "semilocal" approximations, to distinguish them from LDA while acknowledging that in their mathematical form, GGAs remain local in the sense that $v_{xc}^\sigma(\mathbf{r})$ is a multiplicative potential. GGA functionals significantly improve thermochemistry relative to LDA; typical errors are 10–20 kcal/mol for atomization energies *(61, 183)* and 5–15 kcal/mol for barrier heights *(61, 182)*.
- *Rung 3: Meta-GGAs (mGGAs)*. These functionals are also semilocal but incorporate additional derivatives including $\hat{\nabla}^2\rho_\sigma$ and the *kinetic energy density*,

$$\tau_\sigma(\mathbf{r}) = \sum_i^{\text{occ}} \| \hat{\nabla}\psi_{i\sigma}(\mathbf{r})\|^2 \tag{3.43}$$

  The function $\tau_\sigma(\mathbf{r})$ is related to the electron localization function *(184)*, and together with $\hat{\nabla}^2\rho_\sigma$ it can be used to express the noninteracting kinetic energy *(185)*. The best mGGA functionals improve upon GGA thermochemistry, with errors of 5–10 kcal/mol for atomization energies *(61)* and 3–6 kcal/mol for barrier heights *(61, 182)*. It is worth noting that some mGGAs introduce a considerable number of parameters *(61)*, and exhibit basis-set and grid sensitivities suggesting that they may be overfitted *(186–189)*.
- *Rung 4: Hyper-GGAs*. As originally defined by Perdew et al. *(179, 180)*, this category consists of functionals that incorporate "exact exchange and compatible correlation" *(179)*. A few genuine hyper-GGAs have been put forward *(190, 191)*, but it has proven difficult to construct correlation functionals that work well with 100% HFX. As such, the fourth rung on Jacob's ladder has effectively been redefined to mean *hybrid functionals (181)*, which incorporate some fraction of HFX ($0 < \alpha_{hfx} < 1$), in conjunction with a fraction $1 - \alpha_{hfx}$ of semilocal exchange. These functionals are sometimes further categorized as either hybrid GGAs or hybrid mGGAs, depending on the nature of the semilocal contribution. The best hybrid functionals exhibit errors <5 kcal/mol for atomization energies *(61)* and 2–4 kcal/mol in barrier heights *(61, 182)*. This has made hybrids the de facto choice for molecular quantum chemistry.
- *Rung 5: Double-hybrid functionals (192)*. These incorporate a fraction of the second-order Møller-Plesset (MP2) correlation energy in addition to fractional HFX, which introduces a dependence on the virtual MOs $\{\psi_{a\sigma}\}$, whereas functionals on the lower rungs depend only on the occupied MOs. Although double hybrids exhibit some of the best accuracy

in contemporary DFT, with errors of 1–3 kcal/mol for barrier heights *(182, 192)*, the introduction of MP2 correlation brings with it the much slower basis-set convergence of wave function methods, as well as a question of whether the orbital-dependent MP2 term should be self-consistently optimized. (Typically, it is not *(192)*.)

A comprehensive list of functionals can be found in Ref. *(61)*. The aforementioned error statistics pertain to ground-state thermochemistry, whereas accuracy for vertical excitation energies computed using LR-TDDFT is considered in the following section. For double-hybrid functionals, the formulation of LR-TDDFT *(193)* begins to look more like CIS with perturbative double excitations, a method known as CIS(D) *(194)*, which incurs a formal scaling of $n_{\text{roots}} \times \mathcal{O}(n_{\text{basis}}^5)$ and often requires a form of quasidegenerate perturbation theory *(195, 196)*. For these reasons, the application of double hybrids to excited-state problems is still in its infancy and is not discussed in this chapter.

In the context of LR-TDDFT, there is one further category of functionals that warrant mention, namely, *range-separated hybrid* (RSH) functionals. These partition the electron-electron Coulomb interaction ($r_{12}^{-1}$) into a short-range (SR) component and a long-range (LR) background, typically using the error function (erf):

$$\frac{1}{r_{12}} = \underbrace{\frac{1-[\alpha+\beta\,\mathrm{erf}(\mu r_{12})]}{r_{12}}}_{\text{SR}} + \underbrace{\frac{\alpha+\beta\,\mathrm{erf}(\mu r_{12})}{r_{12}}}_{\text{LR}} \tag{3.44}$$

This partition introduces parameters $\alpha$, $\beta$, and $\mu$. The latter is the *range-separation parameter* that determines the length scale ($\sim\mu^{-1}$) of the separation between the SR and LR components of $r_{12}^{-1}$; see Fig. 3.2. Consider a GGA or hybrid functional of the form

$$E_{\text{xc}} = \alpha E_{\text{x,HF}} + (1-\alpha)E_{\text{x,GGA}} + E_{\text{c}}^{\text{GGA}} \tag{3.45}$$

where $E_{\text{x, GGA}}$ is the semilocal GGA exchange functional and $\alpha \equiv \alpha_{\text{hfx}}$ is the coefficient of HFX. The RSH functional corresponding to Eq. (3.45) is

$$E_{\text{xc}}^{\text{RSH}} = \alpha E_{\text{x,HF}}^{\text{SR}} + (\alpha+\beta)E_{\text{x,HF}}^{\text{LR}} + (1-\alpha)E_{\text{x,GGA}}^{\text{SR}} + (1-\alpha-\beta)E_{\text{x,GGA}}^{\text{LR}} + E_{\text{c}}^{\text{GGA}} \tag{3.46}$$

where

$$E_{\text{x,GGA}}^{\text{LR}} = E_{\text{x}}^{\text{GGA}} - E_{\text{x,GGA}}^{\text{SR}} \tag{3.47}$$

Quantities labeled "SR" or "LR" in these equations are evaluated using the corresponding component of $r_{12}^{-1}$. The idea is to correct the asymptotic behavior of a semilocal potential $v_{\text{xc}}^{\sigma}(\mathbf{r})$ at long range (using HFX), while attempting to have minimal impact on the SR behavior of the GGA or hybrid GGA in question, since that functional is responsible for the favorable thermochemical predictions in the ground state. RSH functionals have become popular enough that traditional hybrids such as PBE0 or B3LYP are often called "global hybrid" (GH) functionals in contemporary parlance, to emphasize that HFX is added at all length scales in these cases. The definition of $E_{\text{x,GGA}}^{\text{LR}}$ in Eq. (3.47) is consistent with other literature *(197–199)*, although it is worth noting that this quantity is not truly long ranged. In fact, the reason that RSH functionals were introduced in the first place was to address the fact that semilocal exchange falls off too rapidly with distance *(200–202)*, leading to an insufficiently attractive interaction potential between a well-separated electron and hole *(201–203)*.

Nomenclature and usage for RSH functionals has become somewhat muddled and the remainder of this section attempts to clarify it. An RSH functional is any that uses a partition of $r_{12}^{-1}$ into SR and LR components, with Eq. (3.44) as the most common partition although other forms have been explored *(204–209)*, including variants with a three-way partition of $r_{12}^{-1}$

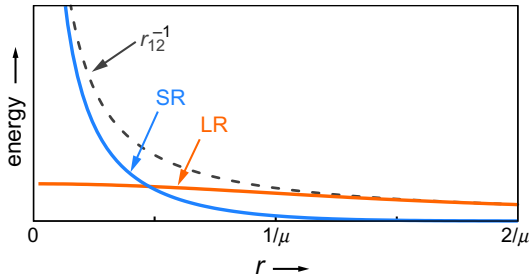


**FIG. 3.2** Partition of the electron-electron Coulomb potential $r_{12}^{-1}$ into short-range (SR) and long-range (LR) components on a length scale $\sim\mu^{-1}$, according to Eq. (3.44) with $\alpha + \beta = 1$.

into short-, middle-, and long-range contributions *(210–215)*. For many of these functionals, the range-separation parameter(s) are optimized or fitted alongside other parameters that define the functional and should not be modified. Examples include the "ωB97" class of functionals *(216–220)* and range-separated versions of the "Minnesota" functionals *(221–224)*. These functionals do not always afford correct the asymptotic behavior of the XC potential, however. For the *ansatz* in Eq. (3.44), the proper behavior requires $\alpha + \beta = 1$ but this constraint is sometimes violated in the interest of obtaining more accurate excitation energies for localized transitions. (The CAM-B3LYP functional *(225) is a popular example that violates this constraint*.)

In contrast to this empirical approach to range separation, *long-range corrected* (LRC) functionals represent a subset of RSH functionals that are constrained to include 100% HFX in the limit $r_{12} \rightarrow \infty$ *(200, 226–228)*. For a given GGA ($\alpha_{\text{hfx}} = 0$) or hybrid GGA ($\alpha_{\text{hfx}} > 0$) functional, the corresponding LRC functional is

$$E_{\text{xc}}^{\text{LRC}} = \alpha_{\text{hfx}} E_{\text{x,HF}}^{\text{SR}} + E_{\text{x,HF}}^{\text{LR}} + (1 - \alpha_{\text{hfx}}) E_{\text{x,GGA}}^{\text{SR}} + E_{\text{c}}^{\text{GGA}} \tag{3.48}$$

The parameter μ in Eq. (3.44) still controls the length scale on which LR-HFX is activated, but $\alpha + \beta = 1$ is satisfied by construction and therefore $v_{\text{xc}}^{\sigma}(r) \sim -r^{-1}$ for any $\mu > 0$. The LRC strategy is thus to graft correct asymptotic behavior onto an existing semilocal XC functional, while doing the least possible damage to that functional at short range. Nonempirical adjustment (or "tuning") of the parameter μ is often employed in this context, especially where CT states are involved. See Section 3.2.3 for additional discussion of this topic.

LRC functionals require modification of the semilocal GGA exchange functional in order to use an attenuated Coulomb potential. (HFX integrals can be modified once and for all to separate them into LR and SR contributions *(229)*.) There are several routes to modify $E_{\text{x,GGA}}$. The first of these, originally introduced by Hirao and coworkers *(200–202)*, modifies the exchange inhomogeneity factor that multiplies the electron-gas exchange energy density. The present author has suggested that these functionals should be denoted as LRC-μGGA *(230, 231)*, where "GGA" indicates the semilocal parent functional, for example, GGA = BLYP or PBE. Note that "LC" is another common abbreviation for long-range correction so that functionals such as LC-BLYP *(200)* might more descriptively be called LRC-μBLYP, in order to emphasize which SR-GGA exchange function (μBLYP) is being used.

For semilocal exchange functionals such as PBE that are based on a model for the exchange hole *(232, 233)*, an alternative strategy is to combine that model with an attenuated Coulomb potential in order to obtain $E_{\text{x,GGA}}^{\text{SR}}$ *(228, 233)*. To distinguish this from the LRC-μPBE functional constructed using Hirao's approach, the present author has suggested the nomenclature LRC-ωPBE for the model based on the PBE exchange hole *(230, 231)*, which comports with the notation for the range-separation parameter (ω) that was introduced in Ref. *(233)*. The term LC-ωPBE is synonymous with LRC-ω PBE, and LR-ωPBEh is sometimes used to indicate a short-range hybrid ($\alpha_{\text{hfx}} > 0$). In contrast, ωPBE refers only to the modified exchange functional, $E_{\text{x,PBE}}^{\text{SR}}$, and should not be used to mean the LRC functional because $E_{\text{x,PBE}}^{\text{SR}}$ is used in other capacities. For example, the HSE functional *(234)*, sometimes called HSE06 *(235)*, uses ωPBE in conjunction with SR-HFX to construct a hybrid functional that is efficient for periodic calculations.

### 3.2.2.3 Accuracy for vertical excitation energies

There have been numerous systematic surveys of the accuracy of various XC functionals for use in LR-TDDFT *(236–246)*, enough to have spawned a metareview of the benchmark studies themselves *(18)*. Two of these studies are highlighted here, to provide some sense for how various categories of functionals can be expected to perform. As usual in DFT (and even more so in LR-TDDFT), for any given molecule it is likely that one could find *some* XC functional that outperforms the statistically best approach. As such, it is only by understanding trends among functionals (and likely trying the same calculation with more than one functional) that results can be taken seriously. Both of the studies highlighted here compare vertical excitation energies to experimental data, and while that has the advantage of being a direct comparison against numbers that one might hope to simulate, it has the disadvantage that vertical excitation energies are not strictly measurable quantities and various effects including solvatochromatic shifts and vibrational averaging are folded into the comparison. Other studies have compared LR-TDDFT excitation energies against correlated wave function benchmarks *(236–239)*, which make for a much more straightforward test of the theory although unfortunately such comparisons sometimes get little traction outside of quantum chemistry circles, where comparison of theory against theory is often viewed with derision. Fortunately, the trends that are highlighted herein are reasonably similar to those obtained by comparing against ab initio benchmarks. In assessing the performance of various functionals, we will use the taxonomy of Jacob's ladder as an organizing principle. The accuracy of the best-performing LR-TDDFT functionals follows this paradigm reasonably well, with the caveat that existing hybrid mGGA functionals do not consistently outperform hybrid GGAs *(239)*.

A first set of benchmarks is depicted in Fig. 3.3, for a set of 101 transitions in 14 gas-phase molecules *(244)*. Error statistics are grouped and color coded by category, including (GH-)GGAs and (GH-)mGGAs but not RSH functionals. Errors are further separated into singlet excitations, triplet excitations, $n\pi^*$, $\pi\pi^*$, and Rydberg excitations. Examining these data, it quickly becomes apparent that the GH functionals significantly outperform the semilocal ones, across all types of data, although it is less clear whether GH-mGGA functionals are categorically superior to GH-GGAs. Perhaps surprisingly, the PBE0 and B3LYP functionals outperform most other functionals, including much newer mGGAs and some GH-mGGAs of the Minnesota type *(247)*, although M06-2X does exhibit slightly smaller errors. The B3LYP and PBE0 functionals, which for many years have served as the closest there is to a "default" setting in molecular DFT, continue to outshine many other functionals for vertical excitation energies. Other benchmarks give a slight advantage to ωB97X-D *(239)*.

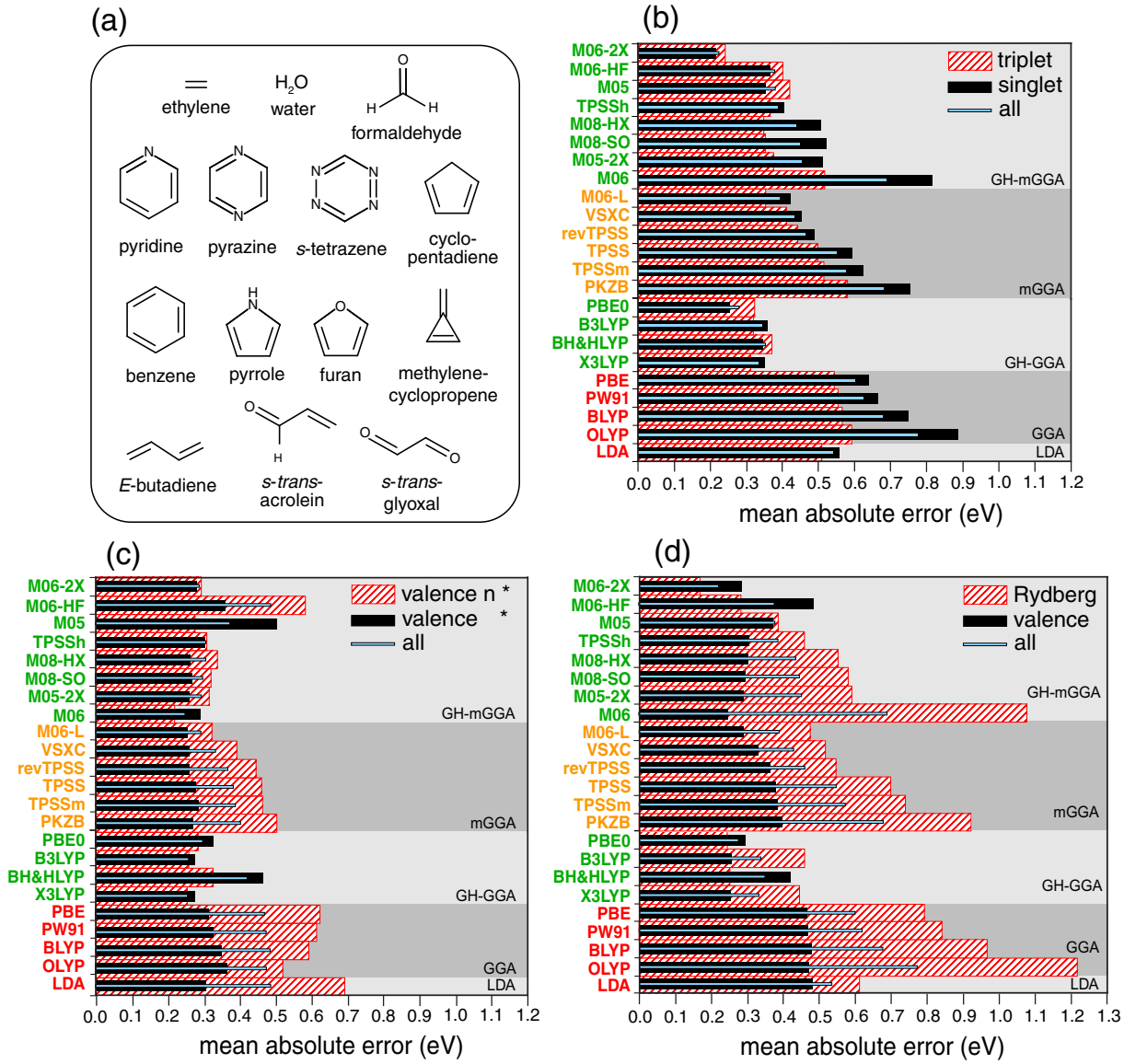


**FIG. 3.3** Errors in TDDFT/6-311++G(3df,3pd) vertical excitation energies, versus experiment. (A) Molecular data set, including 63 singlets (15 $^1\pi\pi^*$, 14 $^1n\pi^*$, 3 $^1n\sigma^*$, 1 $^1\sigma\pi^*$, and 30 Rydberg excitations) and 38 triplets (15 $^3\pi\pi^*$, 12 $^3n\pi^*$, and 11 Rydberg excitations). Error statistics are then plotted for (B) singlet versus triplet excitation energies, (C) $n\pi^*$ versus $\pi\pi^*$ excitation energies, and (D) Rydberg versus valence excitation energies. Functional names are grouped according to the taxonomy of Jacob's ladder: global hybrids, meta-GGAs (mGGAs), and GGAs. The global hybrids are further categorized according to whether they are based on GGAs (GH-GGAs) or mGGAs (GH-mGGAs). Within a given category, the functionals are ordered according to the overall MAEs for the entire data set. For ease of comparison, the horizontal scale is the same in each panel. *(Adapted with permission from Leang, S. S.; Zahariev, F.; Gordon, M. S. Benchmarking the Performance of Time-Dependent Density Functional Methods. J. Chem. Phys.* **2012**, *136, 104101; copyright 2012 American Institute of Physics.)*

The best-performing functionals (PBE0, B3LYP, and M06-2X) exhibit mean absolute errors (MAEs) of ∼0.3 eV for the entire data set. Unlike other functionals examined in Fig. 3.3, these ones do not seem to be systematically worse for $n\pi^*$ states as compared to $\pi\pi^*$ states. In contrast, none of the GGA functionals has an MAE below 0.5 eV and the semilocal mGGAs also have MAEs $\gtrsim$0.4 eV, with M06-L as the best performer among the latter. All of the semilocal functionals perform significantly worse for $n\pi^*$ excitations than they do for $\pi\pi^*$ excitations.

The comparison between Rydberg and valence excitations in Fig. 3.3D warrants special attention. With few exceptions, errors are significantly larger for the Rydberg excitations. Significant errors in Rydberg excitation energies were noted in the early molecular applications of LR-TDDFT *(248)*, leading to the understanding that these excitation energies are quite sensitive to the long-range behavior of the XC potential. That behavior is incorrect for almost all of the functionals evaluated in Fig. 3.3. Later this analysis was extended to CT excitation energies in general *(203)*, of which Rydberg excitations can be considered a special case insofar as these states involve excitation into a diffuse orbital, relatively far from the molecular core. This observation eventually led to the understanding that HFX is the only component of modern functional construction that exhibits the proper asymptotic behavior for a charge-separated state, whereas semilocal XC potentials fall off much too rapidly with distance and thus significantly underestimate both Rydberg and CT excitation energies *(84, 115, 248–252)*. It is therefore no accident that the only functionals in Fig. 3.3D for which the valence excitation error is larger than the Rydberg excitation error are precisely the ones with the largest fractions of HFX: M06-2X ($\alpha_{hfx} = 0.54$) *(253)*, M06-HF ($\alpha_{hfx} = 1.0$) *(253)*, PBE0 ($\alpha_{hfx} = 0.25$) *(254)*, and BH&HLYP ($\alpha_{hfx} = 0.5$) *(255)*.

A second statistical survey is presented in Fig. 3.4, taken from one of the largest statistical assessments of LR-TDDFT to date *(240)*: 614 singlet excitation energies in 483 solution-phase organic molecules. Vertical excitation energies have been corrected for solvent effects and compared to experimental band maxima. (For a discussion of dielectric continuum solvation models and their application to LR-TDDFT, see Ref. *(256)*.) Functionals are once again grouped by category and this larger data set makes it clear that the GH functionals generally outperform the semilocal mGGA functionals, which themselves outperform the semilocal GGAs. For most of the GH functionals, MAEs are 0.2–0.3 eV as compared to 0.4–0.5 eV for the semilocal functionals, but the mean *signed* errors (Fig. 3.4A) are much smaller for the GH functionals. Signed errors are nearly zero for PBE0 and B3LYP, indicating no systematic error in these cases. In contrast, errors are much larger for GH functionals containing a large fraction of HFX, including BMK ($\alpha_{hfx} = 0.42$) *(257)*, M05-2X ($\alpha_{hfx} = 0.56$) *(258)*, and BH&HLYP ($\alpha_{hfx} = 0.5$) *(255)*. These large-$\alpha_{hfx}$ functionals exhibit bias toward overestimation of excitation energies, whereas semilocal functionals consistently underestimate them.

Also included in Fig. 3.4 are error statistics for a set of RSH functionals. MAEs for these functionals span a wide range from 0.2 to 0.5 eV and in that sense are not better than the GH functionals. Furthermore, whereas semilocal functionals

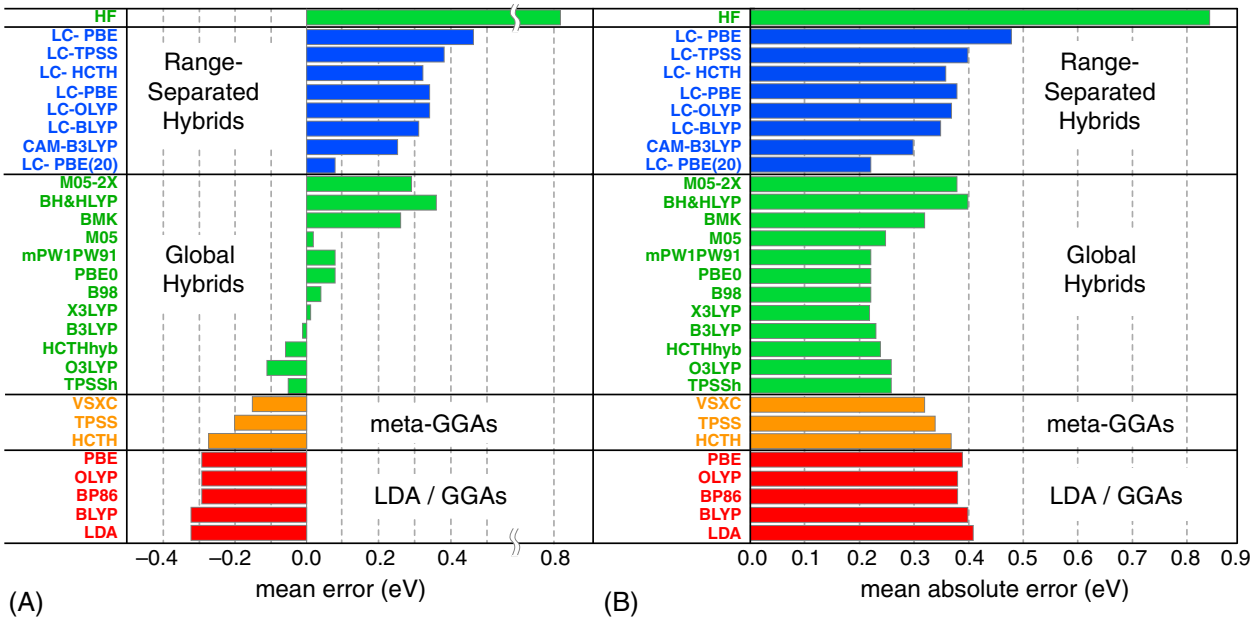


**FIG. 3.4** (A) Mean errors and (B) mean absolute errors for 614 singlet excitation energies of 483 molecules, comparing LR-TDDFT/6-311+G(2d,p) vertical excitation energies (with solvent corrections) to experimental absorption maxima, using data from Ref. *(240)*. *(Adapted with permission from Laurent, A. D.; Jacquemin, D. TD-DFT Benchmarks: A Review. Int. J. Quantum Chem.* **2013**, *113, 2019–2039; copyright 2013 John Wiley & Sons.)*

systematically underestimate excitation energies, GH functionals are largely free of that bias except when $\alpha_{\mathrm{hfx}} > 0.4$. Finally, RSH functionals systematically overestimate excitation energies, which has also been observed in more recent benchmarks for biochromophores *(236)*. Putting these observations together, it seems that some HFX is optimal, perhaps $\alpha_{\mathrm{hfx}} \approx 0.20$–$0.25$, with excitation energies that are too low for smaller values and too high for larger ones. Included the latter category are many LRC functionals that use $\alpha_{\mathrm{hfx}} = 1$ in the asymptotic limit. With that in mind, it is interesting to compare error statistics for LC-ωPBE and LC-ωPBE(20) in Fig. 3.4. The former uses a range-separation parameter $\omega = 0.4$ bohr$^{-1}$ that was optimized for ground-state properties *(259)*, whereas in LC-ωPBE(20) that parameter is set to $\omega = 0.2$ bohr$^{-1}$, leading to significant reduction in the errors. Attempts to fit ω using both ground-state properties as well as excitation energies typically lead to values in the range $\omega = 0.2$–$0.3$ bohr$^{-1}$, depending on whether short-range HFX is present or not *(226, 228, 260)*. This is consistent with the revised choice in LC-ωPBE(20).

#### 3.2.2.4 Visualization

Having computed an excitation energy, there are a variety of tools available to visualize the excited state in question. One could simply examine each pair of occupied and virtual MOs for which the amplitude $x_{ia\sigma}$ is large, but this is often tedious due to significant configuration mixing, especially in the virtual space. At the CIS level, it is easy to understand why the canonical MOs are not a good basis for visualization purposes, since Koopmans' theorem implies that the virtual MOs are reasonable orbitals for electron attachment, not excitation *(59)*. The Hartree-Fock virtual MOs feel the full repulsive potential of the $N$-electron charge density, whereas the occupied MOs feel only $N - 1$ electrons, and this makes the virtual MOs significantly more diffuse than the occupied MOs. Often, the Hartree-Fock virtual MOs are simply unbound and therefore represent discretized continuum states *(261)*, whose shapes are sensitive to small changes in basis set *(262)*. Significant configuration mixing is therefore necessary in order to obtain a localized valence excitation.

In principle, exact Kohn-Sham MOs are a much better basis for excitations *(262–264)*, since both occupied and virtual MOs are subject to the same $N$-electron potential, and in practice it is often the case that the first few Kohn-Sham virtual orbitals are bound ($\varepsilon_{a\sigma} < 0$). Hybrid functionals, however, push the virtual orbitals and their eigenvalues back toward the Hartree-Fock picture and even 20%–25% HFX can be enough to engender significant configuration mixing due simply to the diffuseness of the virtual MOs.

This type of configuration mixing is artificial, in the sense that it can be removed via orbital rotation and therefore does not represent true multiconfigurational character in the excited state. The relevant transformation of the canonical occupied MOs is a unitary matrix $\mathbf{U}_{\mathrm{o}}$ that diagonalizes $\Delta\mathbf{P}^{\mathrm{elec}}$ in Eq. (3.42a):

$$\mathbf{U}_{\mathrm{o}}(\Delta\mathbf{P}^{\mathrm{elec}})\mathbf{U}_{\mathrm{o}}^{\dagger} = \boldsymbol{\Lambda}^2 = \begin{pmatrix} \lambda_1^2 & 0 & 0 & \cdots \\ 0 & \lambda_2^2 & 0 & \cdots \\ & & \ddots & 0 \\ 0 & \cdots & 0 & \lambda_{n_{\mathrm{occ}}}^2 \end{pmatrix} \tag{3.49}$$

The $n_{\mathrm{occ}} \times n_{\mathrm{occ}}$ diagonal matrix $\boldsymbol{\Lambda}^2$ contains the eigenvalues, which are strictly nonnegative and are normalized such that $\sum_i \lambda_i^2 = 1$. The corresponding transformation of the canonical virtual MOs is

$$\mathbf{U}_{\mathrm{v}}(\Delta\mathbf{P}^{\mathrm{hole}})\mathbf{U}_{\mathrm{v}}^{\dagger} = \begin{pmatrix} -\boldsymbol{\Lambda}^2 & \mathbf{0} \\ \mathbf{0} & \mathbf{0} \end{pmatrix} \tag{3.50}$$

These two transformations define the *natural transition orbitals* (NTOs) *(265–268)*, which are the natural orbitals (eigenfunctions) of the excited-state density matrix *(268)*. They can equivalently be defined based on a singular value decomposition of the $n_{\mathrm{occ}} \times n_{\mathrm{vir}}$ matrix of amplitudes, $\mathbf{x} + \mathbf{y}$ *(266, 267)*:

$$\mathbf{U}_{\mathrm{o}}(\mathbf{x} + \mathbf{y})\mathbf{U}_{\mathrm{v}}^{\dagger} = \begin{pmatrix} \boldsymbol{\Lambda} & \mathbf{0} \\ \mathbf{0} & \mathbf{0} \end{pmatrix} \tag{3.51}$$

This form demonstrates that no more than $n_{\mathrm{occ}}$ of the singular values $\{\lambda_i\}$ are nonzero. These eigenvalues appear in pairs $(\pm\lambda_i^2)$ when $\Delta\mathbf{P}^{\mathrm{elec}}$ and $\Delta\mathbf{P}^{\mathrm{hole}}$ are diagonalized, because the natural occupation numbers of the excited-state density matrix are *(268)*

$$n_r = \begin{cases} 1 - \lambda_r^2, & 1 \leq r \leq n_{\text{occ}} \\ \lambda_r^2, & n_{\text{occ}} < r \leq 2n_{\text{occ}} \\ 0, & r > 2n_{\text{occ}} \end{cases} \tag{3.52}$$

The matrices $\mathbf{U}_\text{o}$ and $\mathbf{U}_\text{v}$ transform the canonical occupied and virtual MOs, respectively, into a set of "hole" orbitals $\{\psi_i^{\text{hole}}\}$ along with corresponding "particle" (or "electron") orbitals, $\{\psi_i^{\text{elec}}\}$. These are the NTOs, and their diminishing importance for describing the excitation in question is quantified by the values $\lambda_1^2 > \lambda_2^2 > \lambda_3^2 > \cdots$ .

NTOs provide a much more compact description of the wave function as compared to the canonical MOs, yet one that preserves the phase and nodal structure that can be helpful in qualitatively characterizing the nature of the excitation. This is illustrated in Fig. 3.5 for the $S_0 \rightarrow S_2$ excitation of a five-unit polyfluorene molecule in which a carbonyl defect in one of the terminal fluorene monomers serves to localize the excitation. That localization, however, is not obvious from the canonical MOs, which are delocalized across the length of the molecule, but arises from a coherent superposition of four different occupied MOs. Upon transformation to the NTO basis, there is only one significant singular value, with $\lambda_1^2 = 0.96$. The principle NTO pair, $\psi_1^{\text{hole}} \rightarrow \psi_1^{\text{elec}}$ in Fig. 3.5B, thus paints a picture that is 96% complete.

There is an unfortunate tendency in the literature to refer to $\psi_1^{\text{hole}}$ as the "highest-occupied NTO" (HONTO), with $\psi_1^{\text{elec}}$ then deemed the "lowest-unoccupied NTO" (LUNTO). This terminology is incorrect insofar as "highest" and "lowest" (as in HOMO and LUMO) refer to orbital energies, which are not well defined for the NTOs because the Fock matrix is not diagonal in that representation. The HONTO/LUNTO terminology should therefore be avoided so as not to conflate visual depictions of NTOs with qualitative arguments that might be based on one-electron energy levels, which are only well defined in the canonical MO basis. The term *principle transition orbitals* (or perhaps *principle NTOs*) is suggested instead, to refer to the pair of orbitals corresponding to the largest $\lambda_i$. One might therefore describe a sequence of principle NTOs (pNTOs): pNTO, pNTO $-$ 1, pNTO $-$ 2, … for $\lambda_1^2 > \lambda_2^2 > \lambda_3^2 > \cdots$ .

Another common tool to visualize an excitation is the density difference as compared to the ground state. The unrelaxed density difference

$$\Delta\rho(\mathbf{r}) = \Delta\rho_{\text{elec}}(\mathbf{r}) + \Delta\rho_{\text{hole}}(\mathbf{r}) \tag{3.53}$$

has particle and hole components that are the real-space analogs of the density matrices $\Delta\mathbf{P}^{\text{elec}}$ and $\Delta\mathbf{P}^{\text{hole}}$ in Eq. (3.41). Using the NTOs, the particle and hole densities may be expressed as

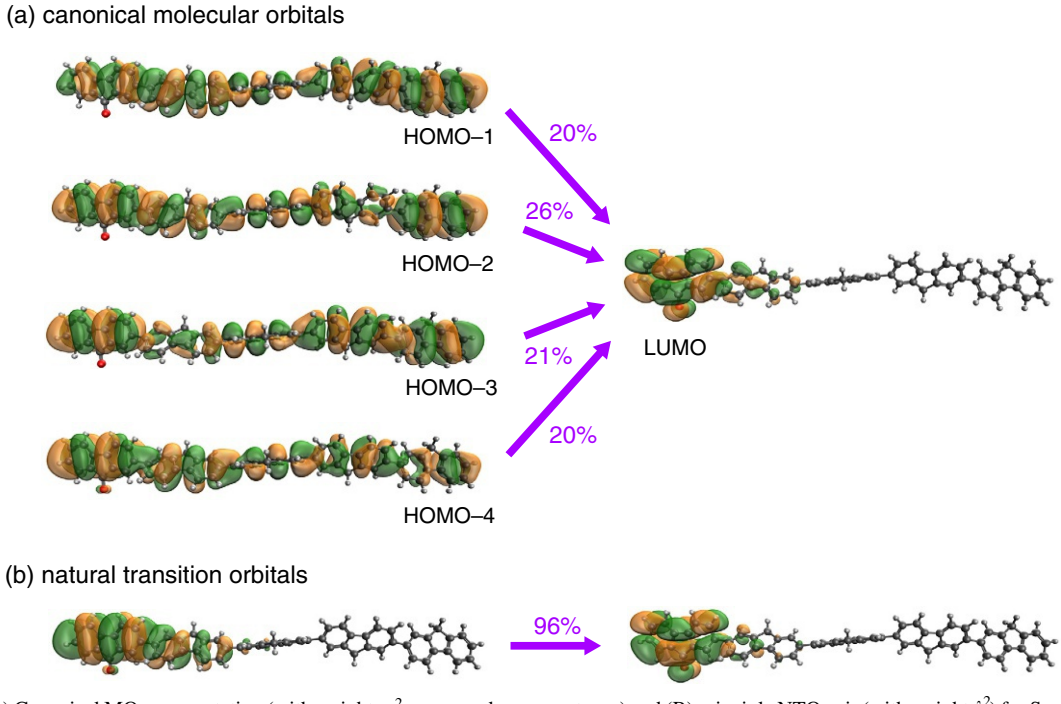


**FIG. 3.5** (A) Canonical MO representation (with weights $x_{ia}^2$ expressed as percentages) and (B) principle NTO pair (with weight $\lambda_i^2$) for $S_0 \rightarrow S_2$ excitation of a five-unit, fluorenone-terminated polyfluorene molecule in which the leftmost monomer contains a carbonyl defect that localizes the excitation. LR-TDDFT calculations were performed at the CAM-B3LYP/3-21G* level within the TDA and the unrelaxed density is analyzed.

$$\Delta\rho_{\text{elec}}(\mathbf{r}) = \sum_{i=1}^{n_{\text{occ}}} \lambda_i^2 |\psi_i^{\text{elec}}(\mathbf{r})|^2 \tag{3.54a}$$

$$\Delta\rho_{\text{hole}}(\mathbf{r}) = -\sum_{i=1}^{n_{\text{occ}}} \lambda_i^2 |\psi_i^{\text{hole}}(\mathbf{r})|^2 \tag{3.54b}$$

Note that $\Delta\rho_{\text{elec}}(\mathbf{r})$ is positive definite and $\Delta\rho_{\text{hole}}(\mathbf{r})$ is negative definite, consistent with Eq. (3.41). Because the NTOs are defined by a singular value decomposition, which distills the $n_{\text{occ}} \times n_{\text{vir}}$ matrix $\mathbf{x} + \mathbf{y}$ into the fewest number of nonzero parameters, the densities in Eq. (3.54) are often dominated by the principle NTO pair. Although it is not widely recognized, the quantities $\Delta\rho_{\text{elec}}(\mathbf{r})$ and $\Delta\rho_{\text{hole}}(\mathbf{r})$ are precisely the *attachment density* and the *detachment density*, respectively, which have long been used to visualize excited states *(269–271)*. (These were originally introduced in a different way *(269)*, based on eigenvectors of $\Delta\mathbf{P}$ that afford positive or negative eigenvalues, respectively.) In the author's view, NTOs are still the preferable description since phase information is lost upon squaring the orbitals in Eq. (3.54).

Fig. 3.6 illustrates these densities for the same $S_0 \rightarrow S_2$ excitation of polyfluorene that was examined in Fig. 3.5. Because $\lambda_1^2 \approx 1$, the particle and hole (or attachment and detachment) densities have the same information content as the principle NTO pair in Fig. 3.5B. Also shown in Fig. 3.6 is the transition density $T(\mathbf{r}) \equiv T(\mathbf{r}, \mathbf{r})$, where $T(\mathbf{r}, \mathbf{r}')$ is defined in Eq. (3.20). For an excitation $|\Psi_0\rangle \rightarrow |\Psi\rangle$, the general definition of this quantity is *(272)*

$$T(\mathbf{r}, \mathbf{r}') = N \int \Psi_0^*(\mathbf{r}', \mathbf{r}_2, \ldots, \mathbf{r}_N)\Psi(\mathbf{r}, \mathbf{r}_2, \ldots, \mathbf{r}_N) d\mathbf{r}_2 \ldots d\mathbf{r}_N \tag{3.55}$$

and for LR-TDDFT in the NTO representation it is

$$T(\mathbf{r}, \mathbf{r}') = \sum_i \lambda_i \psi_i^{\text{elec}}(\mathbf{r})[\psi_i^{\text{hole}}(\mathbf{r}')]^* \tag{3.56}$$

Thus, the NTOs distill the content of the transition density into the smallest possible number of particle-hole pairs. In that well-defined sense, the NTOs are the best orbitals for visualization purposes, and detection of more than one significant singular value $\lambda_i$ indicates unresolvable multideterminant character in the excited state. For the excitation depicted in Fig. 3.6, there is little such character, and $T(\mathbf{r}) \approx \psi_1^{\text{elec}}(\mathbf{r})\psi_1^{\text{hole}}(\mathbf{r})$ is well described by the principle NTO pair. The nature of this product accounts for the somewhat more complicated nodal structure as compared to $\Delta\rho_{\text{elec}}(\mathbf{r}) \approx |\psi_1^{\text{elec}}(\mathbf{r})|^2$ or $\Delta\rho_{\text{hole}}(\mathbf{r}) \approx |\psi_1^{\text{hole}}(\mathbf{r})|^2$.

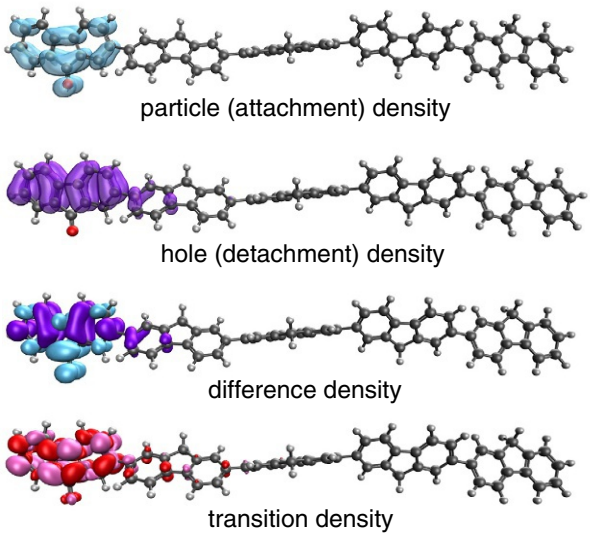


**FIG. 3.6** Visualization of the $S_0 \rightarrow S_2$ excitation of the fluorenone-terminated polyfluorene whose orbital depiction is given in Fig. 3.5, represented here in terms of difference densities. These include the particle density (or attachment density) $\Delta\rho_{\text{elec}}(\mathbf{r})$, the hole density (or detachment density) $\Delta\rho_{\text{hole}}(\mathbf{r})$, the unrelaxed difference density $\Delta\rho(\mathbf{r}) = \Delta\rho_{\text{elec}}(\mathbf{r}) + \Delta\rho_{\text{hole}}(\mathbf{r})$, and the transition density $T(\mathbf{r})$. Each isosurface encompasses 95%–97% of the density in question.

### 3.2.3 Systemic problems

The utility of LR-TDDFT lies in its combination of low cost, which facilitates calculations on systems such as $C_{119}H_{154}ClN_{21}O_{40}$ (Fig. 3.1B) or conjugated polymers (Figs. 3.5 and 3.6), along with an accuracy of ~0.3 eV for localized valence excitations. That level of accuracy requires a treatment of dynamical correlation effects, as seen from the CIS errors in Fig. 3.4 that exceed 0.8 eV, comparable to the ~1 eV of correlation energy for a pair of electrons. That is the good news. In this section, we discuss some of the bad news, namely, systematic errors that make certain types of problems extremely challenging for LR-TDDFT. Of these, the most widely discussed is severe underestimation of excitation energies for states with substantial CT character, ultimately manifesting as an explosion of spurious CT states in a sufficiently large system. A second problem concerns the topology of conical intersections that involve the ground state, which presents a problem for ab initio photochemical simulations of internal conversion following photoexcitation.

#### *3.2.3.1 Description of charge transfer*

Problems with the description of long-range CT excitations manifests in small, gas-phase molecules as Rydberg excitation energies that are systematically too low *(248)*, even when reasonable accuracy is obtained for valence excitations. This was noticed in the early studies of LR-TDDFT and was quickly diagnosed as a symptom of incorrect asymptotic decay of the XC potential in GGA functionals that existed up to that point *(249–252)*. The same problem was quickly recognized to affect CT excitation energies *(84, 115)*. Both CT and Rydberg excitations are sensitive to the long-range behavior of the potential, which should be $v_{xc}^{\sigma}(r) \sim -r^{-1}$ for a charge-neutral molecule *(273–277)*. This asymptotic behavior ought to be borne by the exchange potential because correlation dies off more quickly *(274, 278)*, but in practice so does semilocal exchange.

Consider the form of the LR-TDDFT pseudo-eigenvalue problem for an excitation between MOs $\psi_{i\sigma}$ and $\psi_{a\sigma}$ that are well separated in space, such that $\psi_{i\sigma}(\mathbf{r})\psi_{a\sigma}(\mathbf{r}) \approx 0$ everywhere. A semilocal expression for $v_{xc}^{\sigma}(\mathbf{r})$ affords a semilocal XC kernel, such that the matrix elements $(ia|\kappa_{xc}^{\sigma\tau}|jb)$ in **A** and **B** vanish in such a situation, for all $j$ and $b$. Ignoring spin by setting $\sigma = \tau$ in Eq. (3.19), this leaves

$$A_{ia,jb} \approx (\varepsilon_a - \varepsilon_i)\delta_{ij}\delta_{ab} - \alpha_{hfx}(ij|ab) \tag{3.57}$$

Only the integral $(ij|ab)$, which comes from the HFX term, survives to provide distance dependence for the $i \rightarrow a$ excitation. A pictorial illustration is provided in Fig. 3.7, which plots the distance dependence of the lowest CT excitation energy ($\omega_{CT}$) in the $(C_2H_4)\cdots(C_2F_4)$ dimer as a function of intermolecular separation *(203)*. Only Hartree-Fock theory affords the correct distance dependence for $\omega_{CT}(R)$, which varies according to the Mulliken formula *(66, 279, 280)*,

$$\omega_{CT}(R) = IE_{donor} + EA_{acceptor} - \frac{1}{R} \tag{3.58}$$

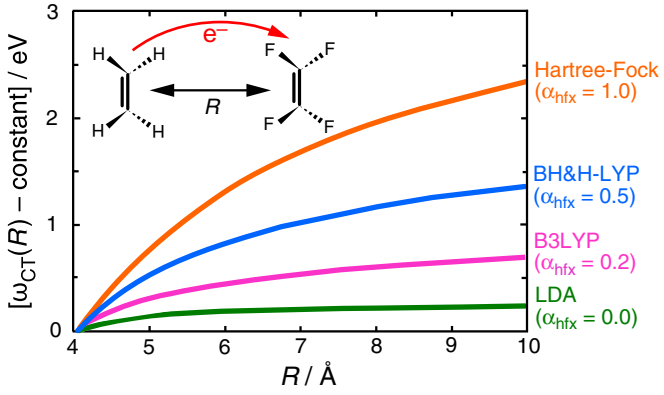


**FIG. 3.7** Distance dependence for the lowest intermolecular CT excitation in $(C_2H_4)\cdots(C_2F_4)$ computed using functionals with various fractions of HFX, as indicated. The *curves* are shifted to a common origin at $R = 4$ Å in order to emphasize the distance dependence of $\omega_{CT}(R)$, which varies asymptotical as $-\alpha_{hfx}/R$. *(Adapted with permission from Dreuw, A.; Weisman, J. L.; Head-Gordon, M. Long-Range Charge-Transfer Excited States in Time-Dependent Density Functional Theory Require Non-Local Exchange. J. Chem. Phys.* **2003***, 119, 2943–2946; copyright 2003 American Institute of Physics.)*

in atomic units. For hybrid functionals, the last term becomes $-\alpha_{\mathrm{hfx}}/R$ rather than $-1/R$, leading to a too-small penalty for long-range CT. For semilocal functionals where $\alpha_{\mathrm{hfx}} = 0$, the CT excitation energy has no distance dependence whatsoever once the donor and acceptor moieties are sufficiently far apart such that their orbitals do not overlap. This is reflected in the flat $\omega_{\mathrm{CT}}(R)$ profile for the LDA functional in Fig. 3.7. As a result, long-range CT excitation energies are almost invariably too small in LR-TDDFT unless the functional contains 100% HFX, which it usually does not because fully nonlocal exchange is somewhat unbalanced given the local nature of existing correlation functionals. The M06-HF functional is an example that does use 100% HFX, leading to reasonable performance for Rydberg states but larger errors for valence excitations (Fig. 3.3D).

Where small-molecule benchmarks are available, errors in CT excitation energies can exceed 3 eV *(228)*, but the problem gets worse in larger molecules so that value is likely limited only by the size of the benchmark systems for which reliable ab initio results are available. A consequence of this severe underestimation of CT excitation energies is the appearance of completely spurious CT excited states in large systems, especially solvated chromophores *(281–288)* but also large molecules *(159, 289, 290)*. When the system size is sufficiently large, there are inevitably well separated occupied and virtual MOs such that the orbital energy gap $\varepsilon_a - \varepsilon_i$ is small. For $\alpha_{\mathrm{hfx}} \approx 0$, the electron-hole interaction vanishes and the diagonally dominant **A** matrix consists of weakly coupled blocks corresponding to these spurious CT transitions. The kernel $f_{\mathrm{xc}}^{\sigma\sigma}(\mathbf{r}, \mathbf{r}')$ lacks the long-range exchange (or a derivative discontinuity *(63, 68, 280)*, or frequency dependence *(291)*) that is needed to provide an energetic penalty for CT, and an upshift to $\omega_{\mathrm{CT}} \approx \varepsilon_a - \varepsilon_i$ as in Eq. (3.57).

A physical example is shown in Fig. 3.8 for a model of aqueously solvated uracil *(287)*. Whereas this system ought to have only a $^1n\pi^*$ and a $^1\pi\pi^*$ state below 6 eV *(227)*, a hybrid LR-TDDFT calculation using the PBE0 functional results in numerous low-energy solvent-to-chromophore CT states, including 27 states below 6 eV for the (uracil)$(H_2O)_{25}$ cluster that is shown in Fig. 3.8 and additional states as the size of the water cluster grows *(227, 287)*. Many of these states are accidentally near degenerate with the optically bright $^1\pi\pi^*$ state and as a result these nominally dark CT states can acquire intensity from the bright state, which diminishes the intensity of the latter because total oscillator strength is conserved by the Thomas-Reiche-Kuhn sum rule, Eq. (3.38). The state $\omega_9$ in Fig. 3.8 exhibits the largest degree of $\pi\pi^*$ character *(287)*, yet due to spurious intensity borrowing it does not exhibit the largest oscillator strength and itself contains some contribution from solvent-to-chromophore CT. Fortunately, the same sum rule can be used to argue that the overall spectral envelope may still be valid upon ensemble averaging and broadening, even if some fraction of the oscillator strength has been ported onto spurious CT excitations.

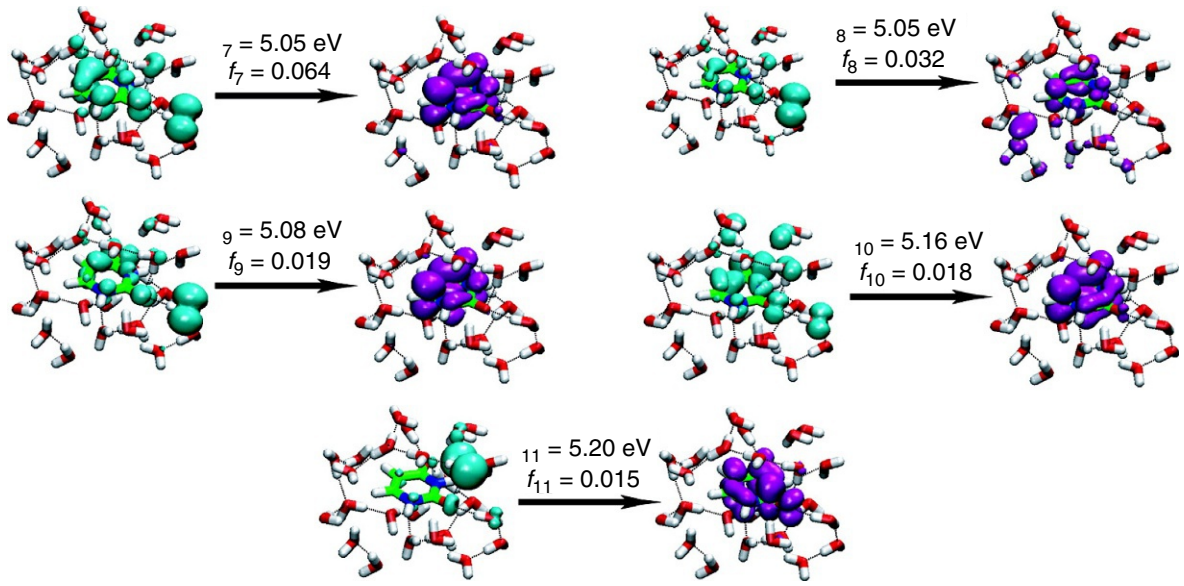


**FIG. 3.8** Selected detachment (hole) and attachment (particle) densities, for excited states of (uracil)$(H_2O)_{25}$ computed using LR-TDDFT at the PBE0/6-31+G* level. These states exhibit spurious solvent-to-chromophore CT in the spectral vicinity of the $^1\pi\pi^*$ state at $\omega \approx 5.1$ eV. Excitation energies $\omega_n$ and oscillator strengths $f_{0n}$ are shown, illustrating intensity borrowing by the spurious CT states. *(Reprinted with permission from Lange, A.; Herbert, J. M. Simple Methods to Reduce Charge-Transfer Contamination in Time-Dependent Density-Functional Calculations of Clusters and Liquids. J. Chem. Theory Comput.* **2007**, *3, 1680–1690; copyright 2007 American Chemical Society.)*

In large chromophores, such as conjugated polymers, spurious low-energy CT excitations can manifest as artificial delocalization of the excitation across the length of the chromophore *(159, 292, 293)*, whereas the CIS method predicts that exciton size eventually saturates even as conjugation length increases *(293)*. As such, there is a need to develop a metric for whether a particular excited state has too much CT character for its excitation energy to be trusted. The first such CT metric to see widespread use was the quantity $\Lambda$ defined by *(294)*

$$\Lambda = \frac{\sum_{ia\sigma}(x_{ia\sigma} + y_{ia\sigma})^2 O_{ia\sigma}}{\sum_{jb\tau}(x_{jb\tau} + y_{jb\tau})^2} \tag{3.59}$$

where

$$O_{ia\sigma} = \int |\psi_{i\sigma}(\mathbf{r})| \cdot |\psi_{a\sigma}(\mathbf{r})| d\mathbf{r} \tag{3.60}$$

measures the overlap of $|\psi_{i\sigma}(\mathbf{r})|$ and $|\psi_{a\sigma}(\mathbf{r})|$. (Absolute values are required since the occupied and virtual MOs are orthogonal.) This overlap is then weighted by the LR-TDDFT amplitudes and normalized such that $0 \leq \Lambda \leq 1$. For calculations that do not invoke the TDA, however, the denominator in Eq. (3.59) is an odd choice, given the normalization condition in Eq. (3.21), and this inconsistency has propagated into other CT metrics used in LR-TDDFT *(295, 296)*. Regarding the metric in Eq. (3.59), an early benchmark study concluded that $0.45 \leq \Lambda \leq 0.89$ for localized valence excitations, making values in this range "safe" for LR-TDDFT, whereas $0.08 \leq \Lambda \leq 0.27$ for Rydberg excitations, which are unsafe *(294)*. It was suggested that excitation energies for which $\Lambda \lesssim 0.3-0.4$ (depending on the functional) should not be trusted. Various LR-TDDFT errors have been rationalized by appeal to $\Lambda$ or similar metrics *(135, 244, 297, 298)*.

The point at which CT character becomes a problem is dependent on the manner in which it is quantified *(299)*, and several alternative CT metrics have been suggested *(294–296, 300–306)*. Ciofini and coworkers introduced a widely used "$D_{\mathrm{CT}}$ metric" *(300)*, originally defined in a rather complicated way but which ultimately measures the distance between the centroids of $\Delta\rho_{\mathrm{elec}}(\mathbf{r})$ and $\Delta\rho_{\mathrm{hole}}(\mathbf{r})$. The centroid of $\Delta\rho_{\mathrm{elec}}(\mathbf{r})$ is

$$\langle \mathbf{r}_{\mathrm{elec}} \rangle = \int \mathbf{r} \Delta\rho_{\mathrm{elec}}(\mathbf{r}) d\mathbf{r} \tag{3.61}$$

with an analogous definition for $\Delta\rho_{\mathrm{hole}}(\mathbf{r})$. If one defines

$$d^{\pm}_{\mathrm{elec/hole}} = \| \langle \mathbf{r}_{\mathrm{elec}} \rangle \pm \langle \mathbf{r}_{\mathrm{hole}} \rangle \| \tag{3.62}$$

then the distance between centroids of the electron and the hole is $d^{-}_{\mathrm{elec/hole}}$, whereas $d^{+}_{\mathrm{elec/hole}}$ is the average position of the center of mass of the exciton. The quantity $d^{-}_{\mathrm{elec/hole}}$ is equivalent to the $D_{\mathrm{CT}}$ metric but is more directly connected to the physics of the excitation. Other similar descriptors can be envisaged *(307, 308)*. For example, by defining the root-mean-square size of the electron and the hole,

$$\sigma_{\mathrm{elec}} = (\langle \mathbf{r}_{\mathrm{elec}} \cdot \mathbf{r}_{\mathrm{elec}} \rangle - \langle \mathbf{r}_{\mathrm{elec}} \rangle \cdot \langle \mathbf{r}_{\mathrm{elec}} \rangle)^{1/2} \tag{3.63a}$$

$$\sigma_{\mathrm{hole}} = (\langle \mathbf{r}_{\mathrm{hole}} \cdot \mathbf{r}_{\mathrm{hole}} \rangle - \langle \mathbf{r}_{\mathrm{hole}} \rangle \cdot \langle \mathbf{r}_{\mathrm{hole}} \rangle)^{1/2} \tag{3.63b}$$

one may define a *charge-displacement distance*,

$$d_{\mathrm{CD}} = d^{-}_{\mathrm{elec/hole}} - \frac{1}{2}(\sigma_{\mathrm{elec}} + \sigma_{\mathrm{hole}}) \tag{3.64}$$

The quantity $d_{\mathrm{CD}}$ connects directly to the properties of the exciton and is a more physically motivated version of the "electron displacement" metric introduced by Adamo and coworkers *(296)*, and one that avoids the incorrect normalization in Eq. (3.59) and is thus rigorously invariant to orbital rotations even when the TDA is not invoked. To the best of our knowledge, $d_{\mathrm{CD}}$ is introduced here for the first time but we suggest that $d^{-}_{\mathrm{elec/hole}}$ and $d_{\mathrm{CD}}$ should replace alternative CT metrics that serve essentially the same purpose.

To combat the long-range CT problem without going beyond the adiabatic approximation, LRC functionals are used to provide an XC potential with correct asymptotic behavior for an electron-hole pair. The LRC modification was introduced in Eq. (3.48) and contains an additional parameter that controls the separation between semilocal GGA exchange at short range and nonlocal HFX at long range. Fig. 3.9 shows an example of how these functionals can be used to mitigate the

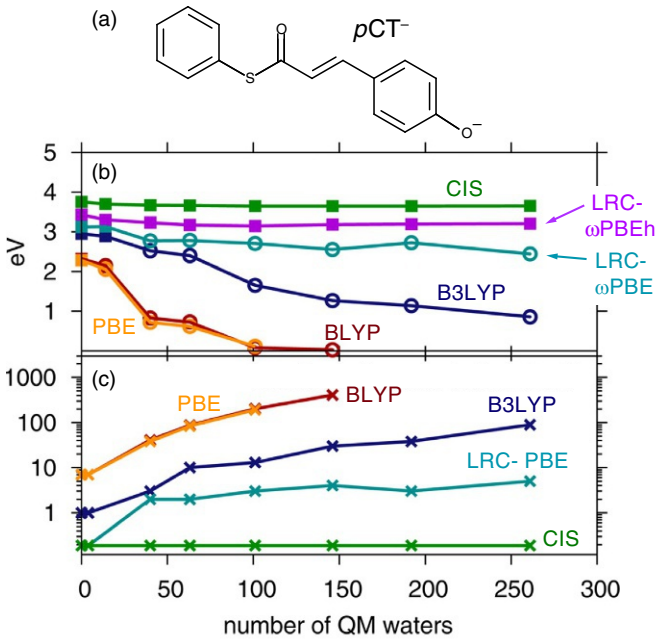


**FIG. 3.9** (A) The chromophore *trans*-thiophenyl-*p*-coumarate (*p*CT$^-$), along with (B) a plot of the lowest TDDFT/6-31G excitation energy for *p*CT$^-$(aq) as a function of the number of water molecules included in the calculation, and (C) the number of TDDFT states below 3 eV in this calculation. *(Adapted with permission from Isborn, C. M.; Mar, B. D.; Curchod, B. F. E.; Tavernelli, I.; Martínez, T. J. The Charge Transfer Problem in Density Functional Theory Calculations of Aqueously Solvated Molecules. J. Phys. Chem. B* **2013**, *117, 12189–12201; copyright 2013 American Chemical Society.)*

growth in spurious CT states around a chromophore in aqueous solution *(288)*. Whereas the number of CT states increases extremely rapidly as water molecules are added around the system, and hybrid functionals such as B3LYP only partially forestall this increase, the functionals LRC-ωPBE *(228)* and LRC-ωPBEh *(260)* control this growth completely. The LRC-ωPBEh functional is a short-range hybrid with $\alpha_{\text{hfx}} = 0.2$, whereas LRC-ωPBE is semilocal at short range ($\alpha_{\text{hfx}} = 0$), but both functionals employ 100% HFX in the long-range limit. This should be contrasted with functionals such as CAM-B3LYP *(225)*, which use range separation but sacrifice proper asymptotic behavior in an effort to obtain more accurate excitation energies for localized valence transitions. Although RSH functionals such as CAM-B3LYP and ωB97X-D are good choices in many respects for valence excitations, neither improves the accuracy of LR-TDDFT for CT excitations *(309)*. Standard double-hybrid functionals contain only a fraction of HFX and thus do not improve the situation for CT states either *(310)*, unless the LRC scheme employed *(311)*.

In the early development of LRC functionals, the range-separation parameter was often fit to minimize error in some benchmark thermochemical or excitation energy data *(200, 202, 226, 228, 259)*. However, excitation energies were found to be quite sensitive to this parameter *(226, 227, 260)*, especially for states with CT character *(227, 260)*. More recently, the community has increasingly turned to a more theoretically well-grounded "optimal tuning" strategy *(231, 312–315)*, based on the ionization energy (IE) theorem of exact DFT *(316, 317)*. That theorem simply states that $\text{IE} = -\varepsilon_{\text{HOMO}}$ for the exact Kohn-Sham functional, consistent with the fact that the IE is set by the asymptotic decay of the wave function *(261)*. This condition is violated badly by common GGA and even hybrid functionals, often by several electron volts *(318, 319)*. The optimal tuning (or "IE tuning") procedure consists in enforcing this condition for an approximate XC functional, by adjusting the range-separation parameter μ such that

$$-\varepsilon_{\text{HOMO}}(N,\mu) = \underbrace{E(N-1,\mu) - E(N,\mu)}_{\text{IE}(N,\mu)} \tag{3.65}$$

Here, IE($N$, μ) represents the ΔSCF value of the IE for the $N$-electron molecule, computed using an LRC functional with range-separation parameter μ. Alternatively, one might try to find the value of μ that comes closest to satisfying Eq. (3.65) for both the $N$-electron molecule and its $(N+1)$-electron anion, representing donor and acceptor for electron transfer. That procedure has been shown to reproduce not only CT excitation energies but also to afford Kohn-Sham gaps ($\varepsilon_{\text{LUMO}} - \varepsilon_{\text{HOMO}}$) in good agreement with fundamental gaps (IE − EA) *(197)*. The optimally tuned value of μ does exhibit a strong dependence on system size, however *(320–323)*. Strategies to mitigate this dependence have been suggested *(323–325)*.

### 3.2.3.2 Conical intersections

A different systemic problem with LR-TDDFT, which is relevant in the context of computational photochemistry, is that it predicts the wrong topology around any conical intersection that involves the ground state *(146, 326)*. The TDHF method suffers from the same deficiency, which is not a DFT artifact per se but rather a linear response artifact, arising from an unbalanced description of the ground (reference) state and the excited (response) states *(27)*. The result is that the branching space around a conical seam that involves the two lowest electronic states is necessarily one-dimensional rather than two-dimensional. (For examples, see Ref. *(146)* or *(326)*.) Even the CIS method can exhibit erratic behavior when the ground state becomes quasidegenerate with the first excited state *(26, 147)*, because in the absence of double excitations the ground- and excited-state eigenvalue problems are decoupled (according to Brillouin's theorem) *(59)*, leading to an unbalanced description *(27, 326)*. This is not a problem for conical intersections between two excited states because those states are coupled by the matrix **A**, in both CIS and LR-TDDFT.

An example of a conical intersection involving the ground state is Jahn-Teller symmetry lowering from $D_{3h}$ to $C_{2v}$, which is illustrated for the $H_3$ radical in Fig. 3.10 *(147)*. In the vicinity of the $D_{3h}$ conical intersection, the upper-state potential surface exhibits erratic behavior at both CIS and LR-TDDFT levels of theory. This warping of the potential surface around a conical intersection has consequences in nonadiabatic molecular dynamics simulations, including SCF convergence difficulties *(327)* and incorrect internal conversion timescales *(26)*. As a result, nonadiabatic trajectory surface-hopping calculations based on LR-TDDFT should probably be terminated prior to internal conversion to the ground state *(26)*.

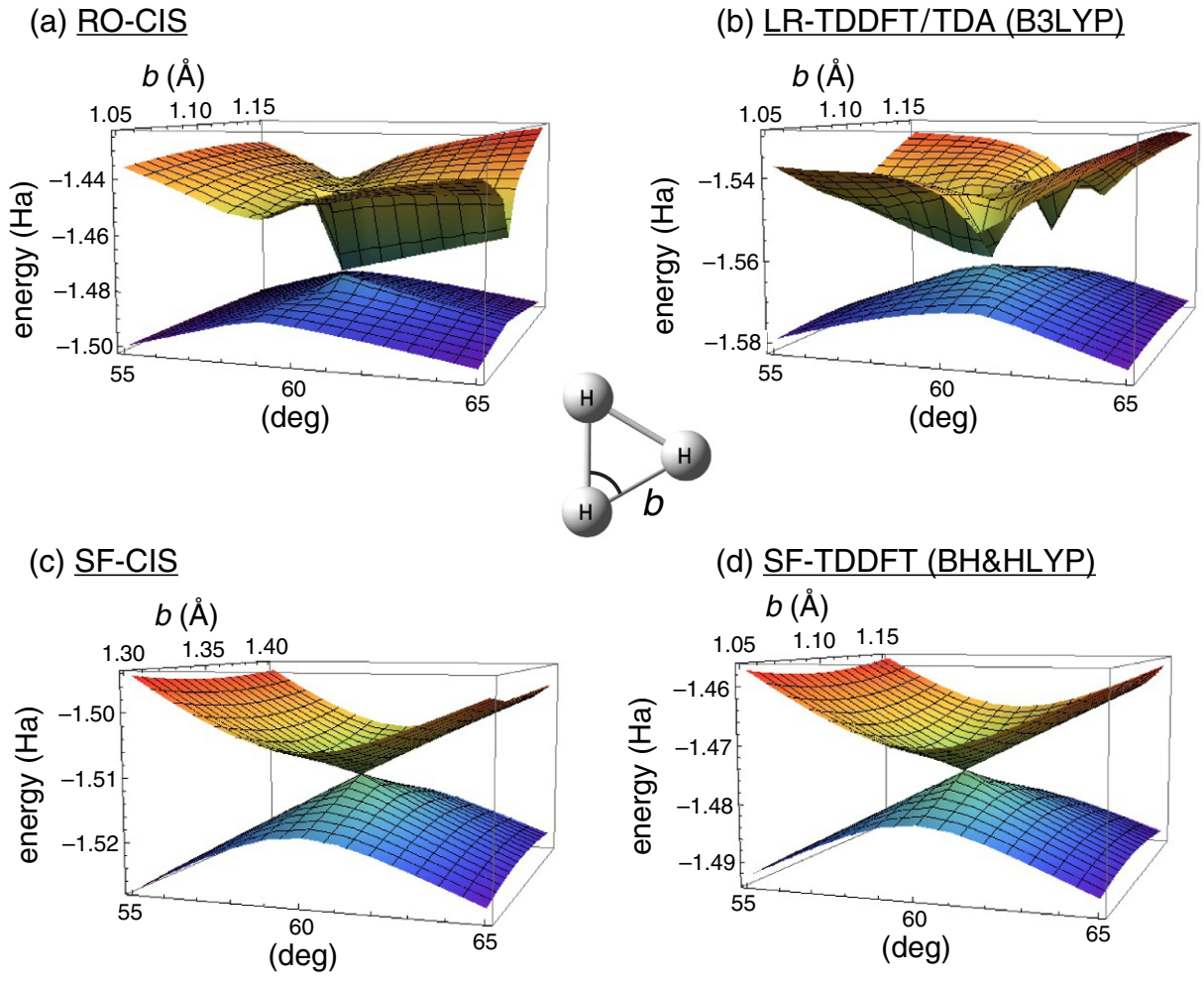


**FIG. 3.10** Potential energy surfaces for the lowest two doublet states of $H_3$ radical along a bond-length coordinate $b$ and a bond-angle coordinate θ, illustrating Jahn-Teller symmetry lowering $D_{3h} \rightarrow C_{2v}$. The methods are (A) CIS based on a restricted open-shell (RO) reference state, (B) LR-TDDFT/TDA using unrestricted B3LYP, (C) SF-CIS, and (D) SF-TDDFT using BH&HLYP. *(Reprinted with permission from Zhang, X.; Herbert, J. M. Analytic Derivative Couplings for Spin-Flip Configuration Interaction Singles and Spin-Flip Time-Dependent Density Functional Theory. J. Chem. Phys.* **2014**, *141, 064104; copyright 2014 American Institute of Physics.)*

The "spin-flip" (SF) variant of LR-TDDFT *(328)* has been suggested as a way to overcome this problem, as discussed in detail in Ref. *(27)*. Briefly, SF-TDDFT uses a sacrificial reference state that is not the ground state of interest, but rather a state with higher spin multiplicity $S+1$, for target states with total spin $S$. By combining single excitations with a single $\alpha \rightarrow \beta$ spin flip, SF-TDDFT generates both ground and excited states of multiplicity $2S+1$ as spin-flipping excitations, meaning that both are obtained as solutions to a common eigenvalue problem. This eliminates the imbalance and restores correct topology to conical intersections involving the ground state, as seen for $H_3$ in Fig. 3.10C and D. Functionals with ≈50% HFX perform well in the context of SF-TDDFT *(27, 329)*, and the Becke "half-and-half" functional BH&HLYP (with $\alpha_{\mathrm{hfx}} = 0.5$) has become the de facto standard for SF-TDDFT *(27)*.

An unfortunate side effect of SF-TDDFT is that it tends to exacerbate spin contamination *(27, 330)*, especially as one moves away from the Franck-Condon point on the potential surface and starts to enter regions of photochemical interest. This necessitates the use of state-tracking algorithms to maintain a consistent spin multiplicity *(330, 331)*. There have been various attempts to find a more theoretically appealing solution to this conundrum by adding additional determinants to the excitation space in order to restore $\hat{S}^2$ symmetry *(27)*. Methods developed along these lines include a fully spin complete version of SF-TDDFT *(330)*, which adds the minimal number of additional determinants needed to obtain $\hat{S}^2$ eigenstates (based on an equation-of-motion formalism) *(77)*, and also a "mixed-reference" spin-flip (MRSF) approach, which uses a combination of high-spin and low-spin $S+1$ reference states to generate target states with spin $S$ *(332–337)*. Although the MRSF-TDDFT excitation manifold is not formally spin-complete, in practice the spin contamination is very small *(332)*. The analytic gradient *(335)* and nonadiabatic derivative couplings *(336)* for MRSF-TDDFT have recently been formulated, facilitating nonadiabatic molecular dynamics simulations.

## 3.3 Excited-state Kohn-Sham theory: The ΔSCF approach

For periodic DFT calculations, LR-TDDFT is theoretically ill-posed if semilocal functionals are used within the adiabatic approximation *(20–22)*. Specifically, the too-rapid asymptotic decay of $v_{\mathrm{xc}}^{\sigma}(r)$ causes the lowest LR-TDDFT excitation energy to collapse to the Kohn-Sham gap, $\hbar\omega = \varepsilon_{\mathrm{LUMO}} - \varepsilon_{\mathrm{HOMO}}$ *(20, 21)*. Semilocal LR-TDDFT also does not produce bound excitons in periodic systems *(22)*, and in large (but finite) conjugated polymers, the exciton delocalization length typically extends to the length of the entire molecule *(293, 338)*. This observation can be conceptualized as incomplete cancellation of self-interaction that grows worse with system size, and infinitely worse under periodic boundary conditions *(20)*. Equivalently, it is a manifestation of the systematic underestimation of CT energies that were discussed in Section 3.2.3.

In recognition of these and other systemic problems exhibited by LR-TDDFT, there has been growing interest in "ΔSCF" approaches that attempt to determine excited-state solutions to the Kohn-Sham SCF equation *(339, 340)*. Having found such a solution, the excitation energy is computed simply as the difference relative to the ground-state energy, hence "ΔSCF." In contrast to the well-automated machinery of LR-TDDFT, these methods are less "black box," involving more effort and finesse on the part of the user, because each excited state requires a separate calculation. On the other hand, the ΔSCF approach can exploit ground-state gradient technology for geometry optimizations and vibrational frequency calculations *(341)*. For this reason, the ΔSCF procedure has sometimes been called excited-state Kohn-Sham theory *(339, 341)*.

In cases where LR-TDDFT exhibits known deficiencies, the ΔSCF approach may be more accurate and more reliable even if the formal justification (based on the Hohenberg-Kohn theorems *(40, 58)*) is absent because the system is not in its ground state. The method therefore rests upon the assumption that the description of short-range dynamical correlation depends upon the local environment of an electron and can be ported to a "non-*aufbau*" solution of the SCF equations, in which an electron has been promoted into a virtual MO. Such a state does not formally satisfy the noninteracting $v$-representability requirement of ground-state DFT *(17, 58, 68, 342)*.

Excited-state SCF solutions do contain full orbital relaxation, yet these solutions are inherently unstable because they are saddle points rather than local minima in the space of orbital rotations. Attempts to locate these non-*aufbau* solutions, each characterized by a virtual (empty) level that is lower in energy than the HOMO level, may suffer "variational collapse" to the ground state or to a lower-lying SCF solution. It is up to the user to determine that the SCF solution corresponds to the state of interest; if not, then the search must begin anew, using a different SCF convergence algorithm or a different initial guess. Several modified SCF algorithms have been developed to try to locate non-*aufbau* solutions, based on overlaps with a set of user-specified MOs *(343–346)* or else based on direct search *(347–349)*. These algorithms are described in Section 3.3.1. Examples of the ΔSCF methodology in action are presented in Section 3.3.2.

### 3.3.1 Theory

#### 3.3.1.1 General considerations

A flowchart for the SCF procedure is illustrated in Fig. 3.11. At each iteration, the occupied MOs $\{\psi_{i\sigma}\}$ are used to construct the Fock matrix $\mathbf{F}_\sigma$, which is then diagonalized to obtain new MOs. Notably, diagonalization results in $n_{\text{basis}} = n_{\text{occ}} + n_{\text{vir}}$ MOs and one must decide how to choose the occupied set. Ordinarily, the lowest eigenvalues $\varepsilon_{r\sigma}$ are selected (*aufbau* principle), resulting in the ground-state determinant upon SCF convergence. To locate an excited-state SCF solution instead, one seeds the procedure with initial-guess MOs from a ground-state calculation but with non-*aufbau* occupancies, promoting an electron from HOMO to LUMO, for example. This makes the LUMO into an occupied level and the HOMO into a virtual level, resulting in a "hole," or in other words a virtual level whose energy lies below that of the highest-occupied level. When the Fock matrix is constructed from this new set of occupied MOs and then diagonalized, the question becomes which of the new MOs should be the occupied ones, since energy levels may have shifted. The SCF procedure therefore deviates from the usual one only when it comes to selecting the occupied subset from among the $n_{\text{basis}}$ MOs. Several different options have been explored, as discussed below.

Before reviewing algorithms for locating non-*aufbau* SCF solutions, however, it is important to note some properties of those solutions that are different from ground-state properties. First, because the effective Hamiltonian $\hat{F}_\sigma[\{\psi_{i\sigma}\}]$ depends on the MOs themselves, the ground- and excited-state Slater determinants are eigenfunctions of different Hamiltonians and are therefore not orthogonal. One consequence is that the formula for oscillator strengths in terms of transition dipole matrix elements (Eq. 3.3) is not strictly valid *(350)*, as that formula is derived using the assumption that the eigenfunctions of the Hamiltonian form a complete orthonormal set *(44)*. In small-molecule tests, however, overlap integrals between ground- and excited-state determinants are found to be $\lesssim 0.1$ *(343)*.

Another general concern is that excited states are always open-shell species, even if the ground state is closed-shell, so any single-determinant approximation is certain to be spin contaminated, perhaps badly so. Indeed, single-determinant approximations for open-shell singlet states are often characterized by $\langle \hat{S}^2 \rangle \approx 1$ (in atomic units of $\hbar^2$), which is equal to the average of pure-state singlet and triplet values. A similar phenomenon occurs, for similar reasons, in the case of the spin-unrestricted Hartree-Fock wave function in the separated-atom limit *(59)*, because a spin-pure state with two half-filled orbitals can be described using a minimum of two Slater determinants. The same two determinants (with different relative signs) are needed to describe both singlet spin-coupling (total $S = 0$) as well as the $M_S = 0$ component of triplet spin-coupling ($S = 1$).

In practice, ΔSCF excitation energies for open-shell singlet excited states are often surprisingly accurate despite significant spin contamination *(343, 345, 351)*, although there are exceptions. One such exception is the $^1B_{1u}$ state of ethylene, whose underestimation by almost 2 eV is attributed to severe spin contamination *(343)*. Yamaguchi and coworkers have developed spin-projection techniques that can be used to recover spin-pure states in such cases *(352–355)*, and approximate spin purification is often used as a practical workaround in "broken-symmetry" DFT calculations of transition metal complexes *(354–356)*. For an open-shell singlet, the most common approach is to approximate the singlet energy as

$$E_{\text{singlet}} \approx 2E_{\text{mix}} - E_{\text{triplet}} \tag{3.66}$$

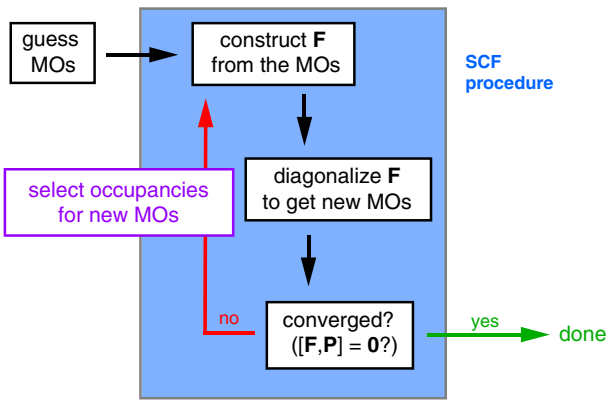


**FIG. 3.11** Flowchart illustration of the SCF algorithm. In the usual approach, occupancy selection is done according to the *aufbau* criterion, with the lowest-energy MOs chosen as the occupied set. For ΔSCF calculations, a different choice is required.

Here, $E_{\text{mix}}$ is the energy of the contaminated (mixed-spin or broken-symmetry) state that is obtained in searching for a singlet solution, whereas $E_{\text{triplet}}$ is the triplet energy for the same system, for which spin contamination is typically less severe. This procedure has a long history *(356, 357)*, and Eq. (3.66) can be viewed as an approximate form of spin projection, generalizable to cases where the target state has spin $S > 0$ *(353)*. The formula in Eq. (3.66) is sometimes implemented in a self-consistent way, that is, using Eq. (3.66) as the *ansatz* and minimizing with respect to orbital rotations. That method is known as *restricted open-shell Kohn-Sham* (ROKS) theory *(358–360)*, and it affords a common set of orbitals for both multiplicites. More often, however, Eq. (3.66) is used as an a posteriori correction scheme *(341, 361–367)*. Even then, Eq. (3.66) can easily be used in geometry optimizations (at the cost of two energy and gradient evaluations per step) and in vibrational frequency calculations *(341)*. For the aforementioned $^1B_{1u}$ state of $C_2H_4$, application of Eq. (3.66) reduces the $\Delta$SCF error (as compared to experiment) from 1.8 to 0.3 eV *(343)*.

### 3.3.1.2 Orbital-optimized non-aufbau SCF solutions

The simplest means to construct a non-*aufbau* occupied set is known as the maximum overlap method (MOM) *(343–346)*. Starting from an initial guess corresponding to non-*aufbau* occupation of the ground-state MOs, this approach uses an overlap criterion to identify the new occupied MOs at each subsequent SCF iteration. To do this, one must compute the projections $p_{r\sigma}$ of the MOs $\psi_{r\sigma}^{(n)}$ at the $n$th iteration onto a reference set of MOs. The reference set might be the MOs at the previous iteration, in which case

$$p_{r\sigma} = \left( \sum_{i}^{\text{occ}} \langle \psi_{i\sigma}^{(n-1)} | \psi_{r\sigma}^{(n)} \rangle^2 \right)^{1/2} \tag{3.67}$$

or else it could be the initial set of ground-state MOs, $\{\psi_{i\sigma}^{(0)}\}$:

$$p_{r\sigma} = \left( \sum_{i}^{\text{occ}} \langle \psi_{i\sigma}^{(0)} | \psi_{r\sigma}^{(n)} \rangle^2 \right)^{1/2} \tag{3.68}$$

The first choice (Eq. 3.67) represents the original version of the algorithm *(343)*, whereas Eq. (3.68) has been called the "initial MOM" (IMOM) algorithm and tends to have better success at converging orbital-relaxed non-*aufbau* states *(345)*. The signature of success is a "hole below the Fermi level," that is, a virtual MO whose energy is lower than the HOMO energy.

The MOM and IMOM algorithms consist simply in replacing the *aufbau* selection of occupied MOs with a selection based on the $n_{\text{occ}}$ largest values of the overlaps $p_{r\sigma}$. All other aspects of the SCF algorithm remain the same. This approach exhibits the same cost per SCF iteration as ground-state DFT and when it succeeds, the rate of convergence (measured by the number of SCF cycles) is typically on par with a conventional ground-state calculation. There are certainly cases where MOM and IMOM fail *(348, 349)*, however, typically resulting in variational collapse to the ground-state SCF solution. In such cases, more robust SCF convergence algorithms are required.

One such approach is the "$\sigma$-SCF" method *(347)*, which is based on minimizing the functional

$$\sigma_{\omega}^2[\Psi] = \langle \Psi | (\omega - \hat{F})^2 | \Psi \rangle \tag{3.69}$$

for a specified energy, $\omega$. This idea stems from recognizing that eigenstates $\hat{F}|\Psi\rangle = \omega|\Psi\rangle$ satisfy the zero-variance condition $\langle \hat{F}^2 \rangle = \langle \hat{F} \rangle^2$. The $\sigma$-SCF approach avoids variational collapse by solving a proper minimization problem, but the appearance of $\hat{F}^2$ means that four-particle operators are required and the requisite transformations endow this method with $\mathcal{O}(n_{\text{basis}}^5)$ scaling *(347)*. This makes the $\sigma$-SCF approach much more expensive than conventional SCF theory.

An alternative approach with the same formal scaling as the ground-state SCF problem is squared-gradient minimization (SGM) *(348)*. Here, the idea is to convert an inherently unstable saddle-point optimization into a search for a local minimum by optimizing an objective function equal to the squared gradient of the energy with respect to orbital rotations. A local minimum can always be converged (if slowly), whereas a saddle point can be missed, and this makes SGM more robust as compared to MOM or IMOM. While the cost remains $\mathcal{O}(n_{\text{basis}}^3)$, it is 2–3 times more expensive per SCF iteration as compared to a conventional SCF calculation, due to the cost of constructing the objective function *(348)*. It is also known that the squared gradient $\| \hat{\nabla} V(\mathbf{x}) \|^2$ of a function $V(\mathbf{x})$ may contain minima that do not correspond to stationary points of the original function *(368–371)*. From the standpoint of trying to locate an orbital-relaxed excited-state Slater determinant, these are spurious solutions.

A middle way between MOM and SGM is state-targeted energy projection (STEP) *(349)*, which does not increase the cost per SCF iteration yet shows much more robust convergence behavior as compared to MOM or IMOM. The STEP approach constructs a projection operator onto the virtual space,

$$\hat{Q}_\sigma = \sum_a^{\text{vir}} |\psi_{a\sigma}\rangle\langle\psi_{a\sigma}| \tag{3.70}$$

where the summation runs over some or all of the virtual MOs. The matrix representation of $\hat{Q}_\sigma$ is $\mathbf{Q}_\sigma = \mathbf{C}_\sigma\mathbf{C}_\sigma^\dagger$, where $\mathbf{C}_\sigma$ consists of column vectors corresponding to whichever MOs are included in Eq. (3.70). The Fock matrix is then modified according to

$$\mathbf{F}'_\sigma = \mathbf{F}_\sigma + \eta\mathbf{S}\mathbf{Q}_\sigma\mathbf{S} \tag{3.71}$$

where $\mathbf{S}$ is the atomic orbital (AO) overlap matrix. The effect of the additional term is to shift all of the orbitals that are included in Eq. (3.70) by an energy $\eta$. By preselecting a virtual MO from the ground-state calculation that will be occupied in the first iteration of STEP, one can modify the Fock matrix to shift other virtual orbitals (including a lower-energy one that was occupied in the ground state but whose electron was promoted) to energies above the non-*aufbau* orbital. For example, upon HOMO → LUMO promotion, the original HOMO is unoccupied and should be included in Eq. (3.70), whereas the LUMO becomes occupied and should be excluded from $\hat{Q}_\sigma$. The STEP algorithm is a form of level shifting that tends to ensure that the SCF algorithm converges to the "closest" stationary point in the space of MO coefficients, which therefore resemble the initial guess *(349)*. Like MOM and IMOM, STEP can be used in conjunction with ground-state gradient technology to perform geometry optimizations and vibrational frequency calculations.

### 3.3.1.3 Transition potential methods

The ΔSCF methods described so far each involve state-specific orbital optimization, meaning that the SCF procedure must be iterated to convergence separately for each excited state of interest. This has the advantage of including full orbital relaxation effects (beyond linear response), but the disadvantage that there is no guarantee that an excited state resembling the one of interest can actually be found. A simpler (if cruder) approach was devised long ago by Slater *(372, 373)*, and forms the basis of several popular techniques for estimating X-ray excitation energies from Kohn-Sham eigenvalues *(374–380)*.

To understand Slater's method, imagine that $E(\{n_i\})$ is the energy of a single-determinant wave function with orbital occupation numbers $\{n_i\}$, some of which might be fractional. Expanding the energy as a Taylor series around a reference energy $E_0 = E(\{n_i^0\})$, keeping the orbitals fixed, one obtains

$$E = E_0 + \sum_i (n_i - n_i^0)\frac{\partial E}{\partial n_i} + \frac{1}{2}\sum_{i,j}(n_i - n_i^0)(n_j - n_j^0)\frac{\partial^2 E}{\partial n_i \partial n_j} + \cdots \tag{3.72}$$

According to the Slater-Janak theorem *(381)*, the first derivative is an orbital eigenvalue: $\varepsilon_i = \partial E/\partial n_i$. Now consider promotion of one electron from an occupied MO to a virtual MO. It suffices to deal with just a pair of occupancies $(n_i, n_a)$, in terms of which the transition in question can be abbreviated as $(1, 0) \rightarrow (0, 1)$. If a fractional-occupancy state with $n_i = 1/2 = n_a$ is used for the reference state $\{n_i^0\}$, then using Eq. (3.72) to compute the excitation energy $\Delta E = E(0, 1) - E(1, 0)$ leads to an estimate

$$\Delta E_{\text{STM}} \approx \varepsilon_a\left(\frac{1}{2}, \frac{1}{2}\right) - \varepsilon_i\left(\frac{1}{2}, \frac{1}{2}\right) \tag{3.73}$$

where the approximation neglects terms of order $(n_j - n_j^0)^3$ *(375)*. This forms the basis of the *Slater transition method* (STM), wherein an SCF calculation is carried out for the fractional-occupancy state $(n_i = 1/2, n_a = 1/2)$ and then the energy difference $\Delta E = \varepsilon_a - \varepsilon_i$ affords an estimate of the excitation energy.

Variants of STM have historically been popular for X-ray spectroscopy *(374–380)*, particularly in the context of periodic DFT calculations for which LR-TDDFT with semilocal functionals is problematic *(21)*. In principle, this method requires a separate SCF calculation for each excitation of interest, and while it is generally easy to converge the X-ray "edge" in this way (i.e., a core → LUMO transition), higher-lying states will require a convergence algorithm that can avoid variational collapse. Moreover, this state-by-state approach leads to nonorthogonal MOs and therefore exhibits the same ambiguities regarding oscillator strengths as the ΔSCF method *(350)*. For these reasons, it is common to omit the 1/2 electron in the virtual space (with only pragmatic justification), leaving $n_i = 1/2$ in the core-excited MO. This variant

of the procedure has been called the transition potential (TP) method *(378, 380,382–385)*. By neglecting to occupy any core-excited virtual states at all, this approach sidesteps the issue of nonorthogonality, at least for a given choice of $n_i$. Oscillator strengths can be computed in a straightforward way from matrix elements $|\langle\Psi_0|\hat{\boldsymbol{\mu}}|\Psi_i^a\rangle|^2$ constructed from the orbitals obtained from the fractional-occupancy SCF calculation.

Modifications to the formula in Eq. (3.73) have also been proposed *(378, 386–388)*, sometimes involving more than one SCF calculation with differing fractional occupancies, or by combining eigenvalues of both the neutral molecule and its cation or anion *(389, 390)*. These modifications represent attempts to eliminate higher-order errors in Eq. (3.72). An example is the "generalized STM" (gSTM) method *(378, 380,386)*, which replaces Eq. (3.73) with

$$\Delta E_{\mathrm{gSTM}} = \frac{1}{4}[\varepsilon_a(1,0) - \varepsilon_i(1,0)] + \frac{3}{4}\left[\varepsilon_a\left(\frac{1}{3},\frac{2}{3}\right) - \varepsilon_i\left(\frac{1}{3},\frac{2}{3}\right)\right] \tag{3.74}$$

This is based on an alternative approximation for the integral

$$\begin{aligned}\Delta E &= \int_1^0 \frac{dE(n_i=\xi, n_a=1-\xi)}{d\xi}d\xi \\ &= \int_1^0 [\varepsilon_i(n_i=\xi, n_a=1-\xi) - \varepsilon_a(n_i=\xi, n_a=1-\xi)]d\xi\end{aligned} \tag{3.75}$$

The original STM in Eq. (3.73) corresponds to a midpoint approximation for this integral *(378, 379,386)*. The gSTM approach requires two separate SCF calculations, one with ($n_i = 1$, $n_a = 0$) and the other with ($n_i = 1/3$, $n_a = 2/3$).

Variants that set $n_i = 0$ (removing the entirety of the core electron) have also been suggested and are sometimes called *full core hole* (FCH) methods *(374–378)*. The TP approach is then a *half core hole* (HCH) method. Although the FCH approach deviates significantly from Slater's original idea, it can be conceptualized as an attempt to restore charge balance, once the 1/2 electron in the virtual space has been abandoned for reasons of convenience. The *excited core hole* (XCH) approach *(391)* is yet another variant that creates a charge-neutral state (which is important for periodic DFT calculations) by placing the excited electron in the LUMO and using the full virtual spectrum from that calculation *(378, 380,391)*:

$$\Delta E_{\mathrm{XCH}} = \varepsilon_a(n_i = 0, n_{\mathrm{LUMO}} = 1) - \varepsilon_i(n_i = 0, n_{\mathrm{LUMO}} = 1) \tag{3.76}$$

Together, these STM- and TP-type procedures are known as *occupancy-constrained* ΔSCF methods. In that context, there has been some discussion of "many-electron" effects on oscillator strengths for X-ray transitions *(392, 393)*. What "many-electron" means in this context is multideterminant character in the final state, which is of course included automatically in a LR-TDDFT calculation.

### 3.3.2 Examples

The primary purpose of this chapter is to survey methods rather than applications but we will highlight a few recent applications of the ΔSCF approach in order demonstrate that it can be an elegant and low-cost alternative in cases where LR-TDDFT performs poorly, such as for CT states *(339, 394)*. Whereas LR-TDDFT systematically (and sometimes dramatically) underestimates CT excitation energies, the same excitation energies are systematically overestimated by the uncorrelated CIS method *(395)*. At the CIS level, a long-range excitation uses up the one occupied → virtual excitation that is included in the *ansatz* and leaves no excitations to facilitate orbital relaxation around either the electron or the hole, hence the overestimation. LR-TDDFT and CIS may therefore bracket the correct answer for a CT state but these upper and lower bounds can be several electron volts apart *(260)*! The ΔSCF approach includes full orbital relaxation and is also less sensitive to the asymptotic behavior of the XC potential. There has also been some preliminary work on the description of conical intersections and nonadiabatic dynamics using ΔSCF methods *(340, 396)*.

States with double-excitation character represent another categorical failure of LR-TDDFT within the adiabatic approximation *(99)*, with the most famous example being the optically dark $S_1(2^1A_g^-)$ state in carotenoids *(397–399)*, or the analogous $2^1A_g^-$ state in butadiene and other conjugated polyenes *(400–404)*. Doubly excited states can be captured accurately using ΔSCF methods *(339, 348, 349)*, as shown for a few examples in Fig. 3.12. For these challenging cases, taken from a benchmark data set of double excitations *(405)*, several mGGA and hybrid functionals prove to be significantly more accurate than the CC3 method, which includes triple excitations and is generally close to CCSD(T) in quality *(406)*, with similar scaling *(407)*. For the full data set from Ref. *(405)*, the hybrid GGA functional ωB97X-V achieves a mean absolute

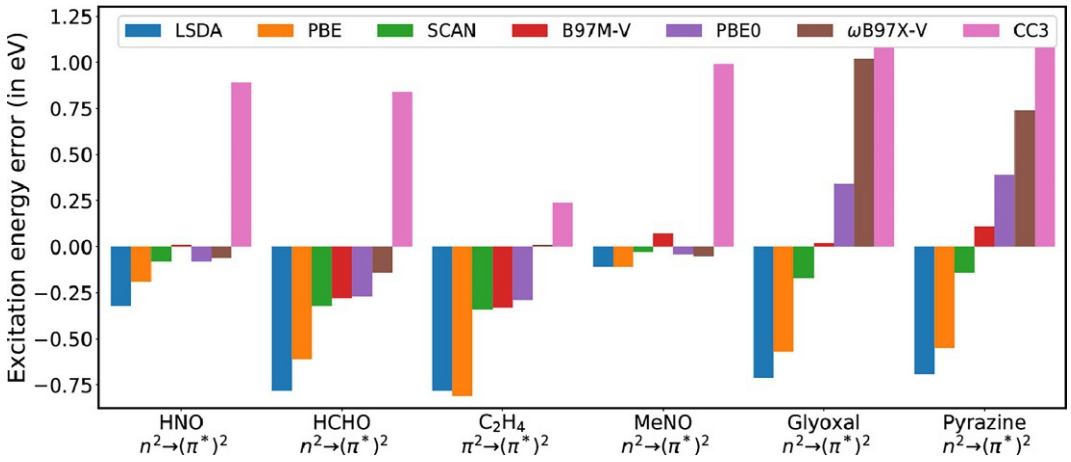


**FIG. 3.12** Errors in doubly excited states at the ΔSCF/aug-cc-pVTZ level vs. benchmarks from Ref. *(405)*. CC3 values are also provided, for comparison. *(Reprinted with permission from Hait, D.; Head-Gordon, M. Orbital Optimized Density Functional Theory for Electronic Excited States. J. Phys. Chem. Lett.* **2021**, *12, 4517–4529; copyright 2021 American Chemical Society.)*

error (MAE) of 0.6 eV and a maximum error of 1.1 eV, whereas for CC3 the MAE is 1.0 eV and the maximum error is 1.8 eV *(349)*. The mGGA functional B97M-V does even better, with an MAE of 0.15 eV and a maximum error of 0.46 eV *(349)*.

The ΔSCF methodology can also be used to compute an electronic absorption spectrum, although this must be done one state at a time by converging a sequence of non-*aufbau* determinants representing individual excited states, and there is no guarantee that some states are not accidentally omitted. A successful example is shown in Fig. 3.13, reproducing the absorption spectrum of the chlorophyll *a* molecule that was only recently measured in the gas phase *(408, 409)*. Using a STEP-based ΔSCF procedure, the major peaks in that spectrum can be identified with transitions among the frontier MOs *(349)*, confirming the basic picture of Gouterman's four-orbital model *(410)*. LR-TDDFT calculations of the same molecule require twice as many states in order to resolve the spectrum up to 300 nm. Many of these states have near-zero oscillator strengths *(408)*, suggesting possible contamination by spurious CT states.

Core-valence excitation energies are fertile ground for ΔSCF techniques. These states appear at photon energies $\hbar\omega > 200$ eV and therefore it is not feasible to reach them by iterative solution of an eigenvalue problem starting from the lowest excitation energies. The frozen-valence approximation is one way to reach these states in LR-TDDFT, which is very accurate for K-edge transitions *(177)* but may be questionable for L- or M-edge excitations. Fortunately, core-to-LUMO excitations are relatively easy to locate using MOM *(344)*. Table 3.1 shows some error statistics for a benchmark set

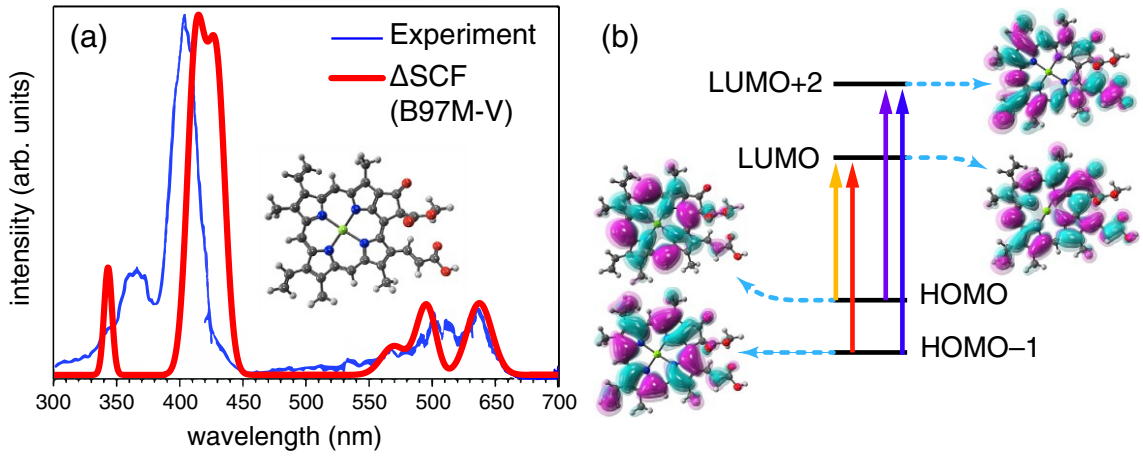


**FIG. 3.13** (A) Absorption spectrum of chlorophyll *a* computed via STEP-based ΔSCF calculations at the B97M-V/def2-TZVP level, spin-purified according to Eq. (3.66) and superimposed on a gas-phase experimental spectrum from Ref. *(408)*. (B) Pictorial representation of Gouterman's four-orbital model. *(Reprinted with permission from Carter-Fenk, K.; Herbert, J.M. State-Targeted Energy Projection: A Simple and Robust Approach to Orbital Relaxation of Non-*Aufbau *Self-Consistent Field Solutions. J. Chem. Theory Comput. 2020, 16, 5067–5082; copyright 2020 American Chemical Society.)*

**TABLE 3.1 Error statistics (in eV) for ROKS calculations of core-level excitation energies, including relativistic corrections.**

| | K edge[a] | | $L_{2,3}$ edges[b] | |
|---|---|---|---|---|
| Functional | *Mean* | *RMSE* | *Mean* | *RMSE* |
| LDA | −4.3 | 4.4 | | |
| PBE | −0.9 | 0.9 | | |
| B97M-V | 1.8 | 1.8 | | |
| SCAN | 0.1 | 0.2 | 0.1 | 0.2 |
| PBE0 | −0.6 | 0.6 | | |
| ωB97X-V | 0.3 | 0.4 | −0.2 | 0.4 |

Data from Ref. *(411)*, using the SGM algorithm and aug-cc-pCVTZ basis set.
[a] *Data set includes 40 transitions for C, N, O, and F atoms. Error is defined with respect to experiment, with atom-specific scalar relativistic effects included in the calculation.*
[b] *Including spin-orbit effects.*

of K- and L-edge transitions *(411)*. Except for the LDA functional, all of the errors are $<2$ eV and several functionals achieve errors $<0.5$ eV, in excitation energies that are hundreds of electron volts. Notably, some of these same functionals also afford accurate L-edge transition energies, if spin-orbit interactions are included in order to describe the splitting of the 2p subshell into $2p_{1/2}$ and $2p_{3/2}$ states *(164)*. This splitting can be quite large, for example, ≈13 eV for Fe(II) *(412, 413)*. Errors of $<0.5$ eV are also possible for heavier elements using ROKS with relativistic corrections *(414)*.

This excellent performance is perhaps somewhat surprising due to the substantially different self-interaction errors in core versus valence orbitals *(415, 416)*. "Optimal tuning" of LRC functionals (Section 3.2.3), in which the range-separation parameter is adjusted to set $\varepsilon_{\mathrm{HOMO}} = -\mathrm{IE}$, can be understood as an attempt to cancel the self-interaction error associated with the HOMO, but that is likely to leave residual self-interaction in the much more compact core orbitals. These errors are exposed in ΔSCF calculations of core-level electron binding energies (for X-ray photoelectron spectroscopy), where many functionals afford errors $\gtrsim$10 eV for transition metals *(417)*. Even the SCAN functional, which performs well for core-excited states of second-row atoms (Table 3.1), affords errors of ∼1 eV for core-level binding energies *(418)*. In several cases, Hartree-Fock theory proves to be more accurate than standard functionals that include correlation, even upon accounting for relativistic corrections *(417, 419)*. This is consistent with other results indicating that the restricted open-shell (RO-)CIS method is a reasonable level of theory for M- and L-edge spectra of solid-state transition metal oxides, despite its lack of correlation effects, provided that spin-orbit corrections are included *(420)*. Resolution of this apparent paradox remains an open question.

For second-row atoms, errors in both core-level IEs *(344, 419, 421)* and also core-level excitation energies *(344, 349, 411)* are comparatively small when using the ΔSCF approach, although even for these elements Hartree-Fock theory is competitive with DFT *(421)*, suggesting that orbital relaxation is much more important than correlation. These rather small errors should be contrasted with much larger ones encountered when LR-TDDFT is applied to the same states using the frozen-valence approximation. Table 3.2 shows results for two different molecules (HF and $CH_4$) using two different functionals (SCAN and ωB97X-V) that both perform well in ΔSCF benchmarks. In contrast to the sub-eV errors obtained using the ΔSCF approach, LR-TDDFT calculations exhibit errors in excess of 10 eV for the carbon K-edge transition and ∼20 eV for the fluorine K-edge transition. For K-edge transitions of Mn(II) at $\hbar\omega \sim 6540$ eV, LR-TDDFT errors of ≈32 eV are obtained using B3LYP, and errors using the GGA functional BP86 are ≈62 eV *(422)*. Errors are even larger for heavier elements *(423)*. Notably, the sign of the errors in Table 3.2 points to underestimation of the excitation energy, consistent with too-soft asymptotic decay of the potential for a transition with CT character from a very compact 1s orbital to a radially diffuse LUMO. LRC functionals perform much better in this capacity *(424, 425)*.

That said, the *precision* of core excitation energies computed using LR-TDDFT is rather good even if the accuracy is not *(425)*, meaning that chemical shifts can be obtained even if absolute excitation energies must be shifted to match experiment. It is the magnitude of the required shifts that is somewhat unnerving. This inspired work on RSH functionals that partition $r_{12}^{-1}$ into short-, middle-, and long-range components *(211–214)*, with the intention to use a larger fraction of exact exchange ($\alpha_{\mathrm{hfx}} \approx 0.87$) at a length scale $\mu^{-1} \approx 0.24$ Å *(426)*. These "short-range corrected" (SRC) functionals work rather well for X-ray calculations using LR-TDDFT *(213)*, although they are empirically parameterized specifically for that

**TABLE 3.2 K-edge excitation energies (in eV) computed in various ways.**

| Method | Functional | Molecule | | Error[b] | |
|---|---|---|---|---|---|
| | | *HF* | $CH_4$ | *HF* | $CH_4$ |
| LR-TDDFT | SCAN | 666.1 | 273.8 | −21.3 | −14.2 |
| ΔSCF +ASP[a] | SCAN | 687.1 | 287.9 | −0.3 | −0.1 |
| ROKS | SCAN | 687.0 | 288.0 | −0.4 | 0.0 |
| LR-TDDFT | ωB97X-V | 668.7 | 276.5 | −18.7 | −11.5 |
| ΔSCF +ASP[a] | ωB97X-V | 687.2 | 288.5 | −0.2 | 0.5 |
| ROKS | ωB97X-V | 687.1 | 288.5 | −0.3 | 0.5 |
| Experiment | | 687.4 | 288.0 | – | – |

Data are from Ref. *(411)*, aug-cc-pCVTZ basis set.
[a]*Using approximate spin projection (ASP), Eq. (3.66).*
[b]*With respect to experiment.*

purpose and may not be good functionals for other applications such as ground-state thermochemistry or valence excitation energies. Furthermore, the SRC functionals are *not* LRC functionals in the sense of Eq. (3.48), because they do not go to a limit of 100% HFX as $r_{12} \rightarrow \infty$. Alternatively, proper LRC functionals have been developed to describe core-level excitations *(211)*.

As illustrated by the porphyrin spectrum in Fig. 3.13 and other examples *(339)*, accurate electronic absorption spectra can be computed via ΔSCF calculations that are carried out in a state-by-state manner. However, this does present something of a nuisance as compared to automatic generation of numerous excitation energies in a LR-TDDFT calculation. Some of the TP and occupancy-constrained ΔSCF approaches that were described in Section 3.3.1 bypass this annoyance by using orbital eigenvalues from one or two fractional-occupancy SCF calculations to obtain the entire spectrum of excitation energies. These methods are assessed (vs. experiment) in Fig. 3.14, for a data set of K-edge transitions *(378)*. Following the notation of Ref. *(378)*, these methods are characterized as either "explicit" or "implicit," with explicit methods involving occupancy constraints that are applied state by state, as suggested by the original Slater method, whereas the implicit methods place no electron at all into the virtual space, which makes for a very simple computational scheme. The "neutral implicit" methods follow the paradigm of the XCH approach *(391)*, placing an electron (or a fraction of an electron) into the LUMO only; it is often possible to optimize a core-to-LUMO SCF solution without specialized algorithms. Finally, the "ground state" results in Fig. 3.14 represent a control experiment in which the ground-state eigenvalue difference

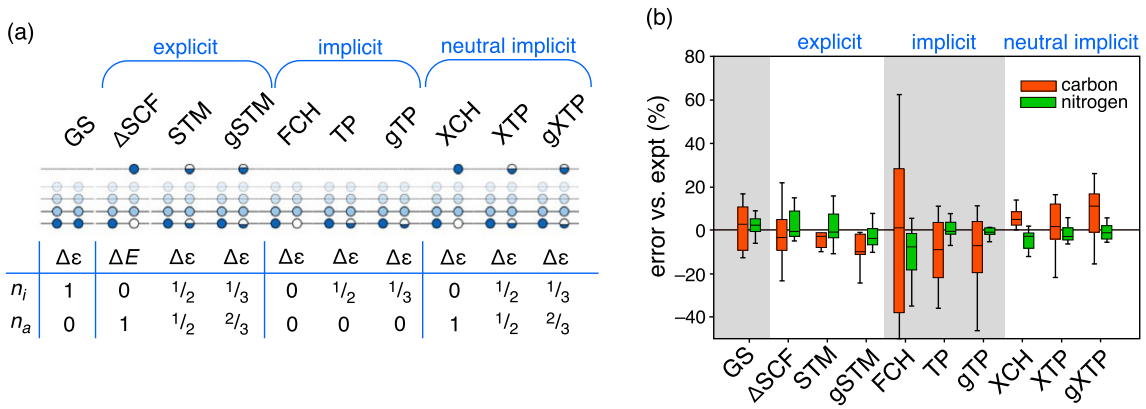


**FIG. 3.14** (A) Pictorial view of TP-type methods based on Kohn-Sham eigenvalues, classified into "explicit" methods that require a separate SCF calculation for each excited state versus "implicit" methods that do not. (B) Percent error for each method (vs. experiment), applying the PBE functional to a data set of K-edge excitation energies. Box plots extend from the 25th to the 75th error percentile with the median value indicated, while the whiskers show the largest outliers. *(Adapted with permission from Michelitsch, G. S.; Reuter, K. Efficient Simulation of Near-Edge X-Ray Absorption Fine Structure (NEXAFS) in Density-Functional Theory: Comparison of Core-Level Constraining Approaches. J. Chem. Phys.* **2019**, *150, 074104; copyright 2019 American Institute of Physics.)*

$\varepsilon_{\mathrm{LUMO}} - \varepsilon_{1s}$ is used to approximate the K-edge transition energy. That method fares surprisingly well, or perhaps the other approaches should be said to fare surprisingly poorly. If the user desires to avoid state-by-state optimization of an occupancy-constrained determinant, then the XCH approach would seem to be the best option.

## 3.4 Time-dependent Kohn-Sham theory: "Real-time" TDDFT

The cost of the ΔSCF approaches described in Section 3.3 is typically no more than a few times the cost of ground-state DFT, depending somewhat on the algorithm that is used to converge the non-*aufbau* SCF solution. With the exception of the $\sigma$-SCF method, the algorithms described in that section each possess the same $\mathcal{O}(n_{\mathrm{basis}}^3)$ scaling as the ground-state calculation. However, these methods must be applied in a state-by-state manner, constructing a different initial guess for each state of interest. This limits their applicability to problems where only a small number of states is desired or required, whereas using LR-TDDFT it is possible to obtain a large number of states in an automated fashion, at least for medium-sized molecules. Systems with a dense manifold of excited states (e.g., semiconductors) can create significant storage bottlenecks for the trial vectors that are required by the iterative eigensolver in LR-TDDFT and the appearance of spurious CT states in condensed-phase applications of LR-TDDFT exacerbates its cost, even if the effect of these states on the overall spectral envelope is close to nil *(287, 427)*. In situations such as these, where proliferation of states (whether real or spurious) makes the iterative diagonalization cost-prohibitive, the TDKS approach may be advantageous. Using this method, a broadband spectrum can be computed from the oscillating dipole moment function obtained from time-dependent electron dynamics.

### 3.4.1 Theory

The TDKS approach is also known as "real-time" (RT-)TDDFT *(51, 52)*, to distinguish it from LR-TDDFT. Starting from the ground-state Kohn-Sham determinant, an external electric field $\boldsymbol{E}(\mathbf{r}, t)$ is turned on at $t = 0$, either as an impulse or as a continuous wave, and the resulting perturbation creates a time-evolving superposition state whose Fourier components encode the excitation energies. This is analogous to propagation of a nonstationary wave packet according to the time-dependent Schrödinger equation. Similar to that situation, the time-dependent MOs $\psi_{k\sigma}(\mathbf{r}, t)$ are complex-valued for $t > 0$. Unlike the many-electron time-dependent Schrödinger equation, the effective Hamiltonian $\hat{F}$ in Kohn-Sham theory depends on its own time-evolving eigenfunctions, and $\hat{F}(t)$ does not commute with $\hat{F}(t')$ for $t \neq t'$. Therefore, the time evolution operator

$$\hat{U}(t_2, t_1) = \exp\left[\frac{-\mathrm{i}(t_2 - t_1)}{\hbar}\hat{H}\right] \tag{3.77}$$

for time-independent Hamiltonian $\hat{H}$ must be generalized to

$$\hat{U}(t_2, t_1) = \hat{\mathcal{T}} \exp\left[-\mathrm{i}\int_{t_1}^{t_2} \hat{F}(t)dt\right] \tag{3.78}$$

for TDKS calculations, where $\hat{\mathcal{T}}$ is a time-ordering operator. This leads to the so-called Magnus expansion that generalizes the time-independent Baker-Campbell-Hausdorff expansion *(428–430)*.

A variety of time-propagation algorithms have been developed for TDKS simulations *(52, 430–434)*, the simplest of which is a "modified-midpoint" algorithm *(432)*. This is a type of explicit Euler integration scheme that requires only one Fock matrix construction per time step. Denoting the Fock and density matrices in the orthonormal MO basis as $\mathbf{F}$ and $\mathbf{P}$, respectively, the Fock matrix $\mathbf{F}$ is first propagated forward in time by a half step, $(\Delta t)/2$. At each subsequent instant in time, $t_n = n\Delta t$, the matrix representation of the propagator is constructed according to

$$\mathbf{U}_n = \exp[-\mathrm{i}(\Delta t)\mathbf{F}_{n+1/2}] \tag{3.79}$$

again in the MO basis *(430)*. The MO density matrix is then propagated from $t_{n-1/2}$ to $t_{n+1/2}$ according to

$$\mathbf{P}_{n+1/2} = \mathbf{U}_n \mathbf{P}_{n-1/2} \mathbf{U}_n^{\dagger} \tag{3.80}$$

(Spin indices are omitted as these equations are valid for either spin.) Construction of $\mathbf{U}_n$ requires diagonalization of the Fock matrix, which is not a problem in Gaussian basis sets but is not feasible in plane-wave basis sets or on a grid; see Ref. *(431)* for a discussion of alternatives when $\mathbf{F}$ is too large to diagonalize. For Gaussian basis calculations, self-consistent

propagators based on predictor-corrector algorithms have also been developed *(430, 435)*. These may require more than one Fock build per time step but allow for the use of somewhat larger time steps as well as for automatic detection of time steps that are too long, which is not always obvious from the usual criterion of checking to make sure that fluctuations in the total energy are bounded *(430)*.

For the modified-midpoint algorithm that is encapsulated by Eqs. (3.79) and (3.80), the cost of a single time step is comparable to the cost of a single SCF cycle of the ground-state calculation. The storage requirement is also modest, amounting to a few complex-valued matrices of dimension $n_{\text{basis}} \times n_{\text{basis}}$. This should be contrasted with the storage requirement for iterative solution of the LR-TDDFT pseudo-eigenvalue problem, which is $\mathcal{O}(n_{\text{roots}} n_{\text{occ}} n_{\text{vir}})$ with a prefactor that reflects the number of iterations and therefore the size of the iterative subspace. The modified-midpoint approach works well provided that the time step $\Delta t$ is sufficiently small and values ranging from 0.01 to 0.50 a.u. are typical, where $1\text{a.u.} \approx 2.42 \times 10^{-17}\text{s} = 24.2$ attoseconds. (The time for one orbit in the Bohr model of the hydrogen atom is $2\pi$ times this value, which establishes a timescale for electronic motion.) The maximum acceptable value of $\Delta t$ is limited not only by stability of the time integration but also by the excitation energies that one desires to access, as discussed below.

Unlike LR-TDDFT, which operates by definition in the limit of a vanishingly weak external field, the TDKS approach is nonperturbative and in principle can be used to simulate electron dynamics in strong laser fields, for example, to simulate nonlinear optical properties of materials *(436)*, or to make contact with emerging attosecond spectroscopies *(57)* that create electronic wave packets that are out of equilibrium with the nuclei and thus outside of the Born-Oppenheimer approximation *(53–56)*. In practice, there are various issues related to the use of the adiabatic approximation *(291, 437, 438)*, meaning the use of ground-state functionals with no memory, such that the time dependence is carried solely by the time-evolving density, $E_{\text{xc}}[\rho(\mathbf{r},t)]$. On the other hand, within the adiabatic approximation the initial-state dependence vanishes since the XC kernel is fully specified in terms of the instantaneous time-evolving density *(439)*. The topic of strong-field electron dynamics and how it can be described using TDKS calculations is not considered here, except to note that there have been successful TDKS simulations of strong-field photoionization *(440–451)*, and also of high harmonic generation *(452–460)*, both in Gaussian-orbital representations of the density. Unlike the grid-based treatments that are common in atomic physics, Gaussian-based methods are scalable to molecules. However, self-interaction error is known to significantly suppress strong-field ionization rates *(461)*. Much of the aforementioned work has thus been performed at the TD-CIS level, where self-interaction is not a concern and the exchange potential has the correct asymptotic form.

This section focuses on the use of TDKS simulations to obtain broadband spectra. Within the electric dipole approximation, which is also invoked in LR-TDDFT insofar as oscillator strengths are proportional to transition dipole matrix elements, the absorption spectrum corresponds to the dipole strength function *(163, 462)*

$$S(\omega) = \left(\frac{4\pi\omega}{3c}\right) \Im\mathfrak{m}[\alpha_{xx}(\omega)+\alpha_{yy}(\omega)+\alpha_{zz}(\omega)] \tag{3.81}$$

where for example

$$\alpha_{xy}(\omega) = \frac{\partial \mu_x(\omega)}{\partial \mathcal{E}_y(\omega)} \tag{3.82}$$

is an element of the dynamic polarizability tensor, $\boldsymbol{\alpha}(\omega)$. The quantities $\mu_x(\omega)$ and $\mathcal{E}_y(\omega)$ are the Fourier transforms of the time-dependent dipole moment and the external electric field, respectively, although for an impulsive $\delta$-function pulse the denominator in Eq. (3.82) can be replaced by the field amplitude while the numerator is replaced by

$$\mu(\omega) = \int_0^\infty w(t)\mu(t)e^{-\mathrm{i}\omega t}dt \tag{3.83}$$

Here, $w(t)$ is a windowing or padding function, as in standard signal processing *(52)*. To obtain a linear absorption spectrum, the external field $\boldsymbol{\varepsilon}(\mathbf{r}, t)$ should be weak, impulsive, and off-resonant, and should contain components in all three Cartesian directions in order to excite states of all symmetries, effectively averaging over molecular orientations. With an appropriately chosen integration time step, this procedure reproduces the same spectrum that is obtained using LR-TDDFT, if *all* of the LR-TDDFT excitations within the energy window of interest are included *(430, 462)*. The TDKS approach affords the entire broadband spectrum from a single Fourier transform (Eq. 3.83) following sufficient time propagation, but it is not straightforward to assign the features in the TDKS spectrum to transitions between specific MOs. Techniques to do so have been developed, based on identifying individual Fourier modes in the dipole moment matrix (expressed in the MO basis) at a specific transition frequency *(463–467)*. This does require some postprocessing and some insight regarding the important MOs. Time-dependent generalization of the NTO basis has also been proposed *(468)*.

The cost of the time steps needed to propagate the Kohn-Sham MOs in time, and thus to obtain the time-evolving density and dipole moment function, is comparable to the cost of a single ground-state SCF cycle but many time steps are required. A typical simulation time might be 30 fs to obtain a fully converged spectrum *(430)*, but with $\Delta t = 0.1$a.u. $= 2.4$ as (1as $= 10^{-18}$ s), this represents $>10^5$ time steps. Recently, Padé approximant techniques have been introduced in order to obtain $\mu(\omega)$ based on a short time series of input data $\mu(t)$ *(52, 465)*. Using this approach, spectra that are well converged (with respect to LR-TDDFT results) can be obtained in $<10$ fs of time propagation and rough spectra can be obtained with as little as 3–5 fs *(163)*. The time step $\Delta t$ dictates the spectral window that can be accessed, via the usual time-energy uncertainty relationship $(\Delta E)(\Delta t) \gtrsim \hbar$ that comes from the Fourier transform. In practice, the spectrum is only reliably converged up the Nyquist frequency $f_{\text{Ny}} = \pi/(\Delta t)$, and perhaps only up to a fraction of that value *(163, 430)*. This implies that especially small time steps are required for X-ray applications. A time step $\Delta t = 0.1$ a.u., for example, corresponds to a Nyquist frequency $\hbar f_{\text{Ny}} = 854$ eV, which is well above the K edge for second-row elements (C, N, O, etc.) but not for third-row elements. The K edge for elements Al–Cl lies above 1500 eV.

### 3.4.2 Examples

As an example of a broadband spectrum of interest in materials science, Fig. 3.15 presents X-ray spectra at the $L_{2,3}$ edge of $\alpha$-quartz, computed using several different TDDFT methods *(469)*. Starting from the lowest valence excitations, a LR-TDDFT calculation with $n_{\text{roots}} = 300$ reproduces the first two features in the experimental spectrum (labeled "A" and "B") but is unable to resolve the higher-energy features. (The calculations do not include spin-orbit coupling and thus

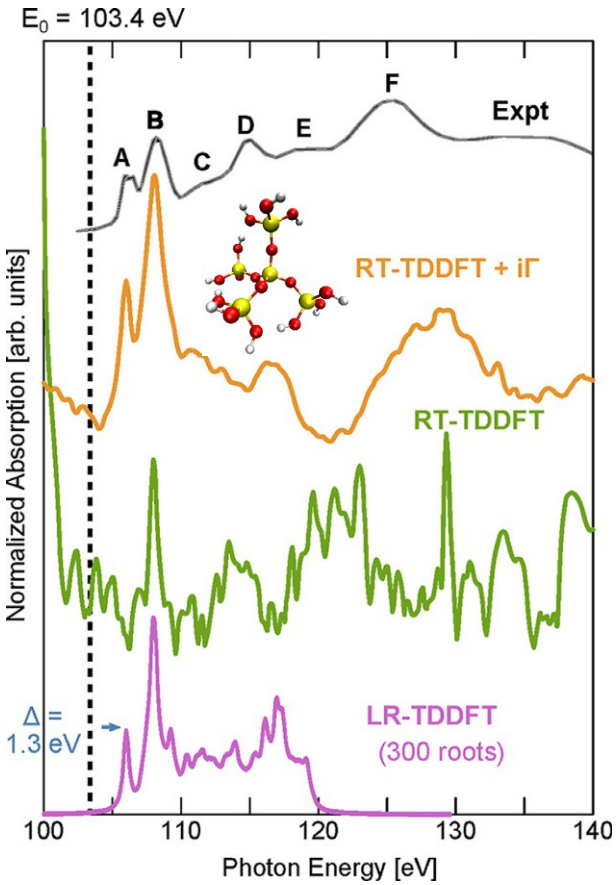


**FIG. 3.15** Experimental X-ray absorption spectra of $\alpha$-quartz at the $L_{2,3}$ edge *(470)*, along with LR- and RT-TDDFT calculations using a cluster model $Si_5O_{16}H_{12}$ of the bulk material (as shown), with modified hydrogen charges to enforce charge neutrality *(469)*. The spectrum labeled "RT-TDDFT + iΓ" includes phenomenological lifetime parameters for the virtual orbitals. All calculations were performed with an optimally tuned version of LRC-ωPBEh. *The dashed line* labeled $E_0$ is the experimental ionization energy of Si(2p). *(Reprinted with permission from Fernando, R. G.; Balhoff, M. C.; Lopata, K. X-Ray Absorption in Insulators With Non-Hermitian Real-Time Time-Dependent Density Functional Theory. J. Chem. Theory Comput.* **2015**, *11*, *646–654; copyright 2015 American Chemical Society.)*

do not reproduce the doublet for peak A, which arises due to the 0.6 eV splitting of the $2p_{3/2}$ and $2p_{1/2}$ levels *(470)*.) Although the most intense feature (peak B) is evident in the RT-TDDFT spectrum, at a peak position that precisely matches the corresponding LR-TDDFT spectrum, the RT-TDDFT spectrum is quite noisy and other features in it are obscured by this noise.

That noise is actually a basis-set artifact arising from the absence of proper continuum states (or the inability to describe ionization within a finite-basis approximation), which has the effect of artificially trapping metastable excitations that lie above the ionization threshold *(469, 471)*. A solution to this problem is to incorporate phenomenological lifetimes for the unbound MOs, meaning those with $\varepsilon_{p\sigma} > 0$. This procedure is described in Ref. *(471)* and corresponds to a modification $\varepsilon_{p\sigma} \rightarrow \varepsilon_{p\sigma} + i\Gamma$ in the MO basis, where $\Gamma^{-1}$ is a phenomenological lifetime that is modeled as a function of energy, decreasing exponentially above the vacuum level. As seen in Fig. 3.15, this "iΓ" modification removes the noise from the RT-TDDFT spectrum, such that most of the experimental features become evident even at energies far above what can feasibly be reached with LR-TDDFT. This does require some phenomenological modeling, however.

When computing K-edge X-ray spectra using high-quality basis sets, similar artifacts can manifest as spurious preedge features that are not seen in compact basis sets where the density of levels $\varepsilon_{p\sigma}$ is more sparse. In a molecule that contains both nitrogen and oxygen, for example, excitations from N(1s) core orbitals to the highest-energy virtual MOs can manifest as spurious preedge features at the *oxygen* K-edge *(163, 472)*, as shown in Fig. 3.16. These artifacts appear despite the fact that the nitrogen K-edge lies >100 eV below the oxygen K-edge! These intruder peaks could potentially be mitigated via heuristic lifetime models for the unbound states, as described earlier, although a simpler fix is to modify the time-dependent dipole moment matrix in the MO basis. That matrix is

$$D_{jk\sigma,x}(t) = -e\langle\psi_{j\sigma}(t)|\hat{x}|\psi_{k\sigma}(t)\rangle \tag{3.84}$$

for the $x$ component. The time-dependent dipole moment function that is needed in Eq. (3.83) is then

$$\mu_x(t) = \mathrm{tr}(\mathbf{P}_\alpha \mathbf{D}_{\alpha,x} + \mathbf{P}_\beta \mathbf{D}_{\beta,x}) \tag{3.85}$$

By eliminating the rows and columns of $\mathbf{D}_{\sigma,x}$ that correspond to occupied MOs other than the ones of interest, prior to computing the Fourier transform in Eq. (3.83), the undesired resonances can be removed from the spectrum *(472)*. For the oxygen K edge, this means retaining only those rows and columns where either $j$ or $k$ refers to a O(1s) orbital. This is precisely analogous to the frozen-valence truncation of the LR-TDDFT excitation manifold that is used to obtain core-level spectra (Section 3.2.2), and may have similar limitations for L- and M-edge spectra. For the oxygen K edge, Fig. 3.16 shows that this procedure affords a spectrum in good agreement with LR-TDDFT, free of contamination by

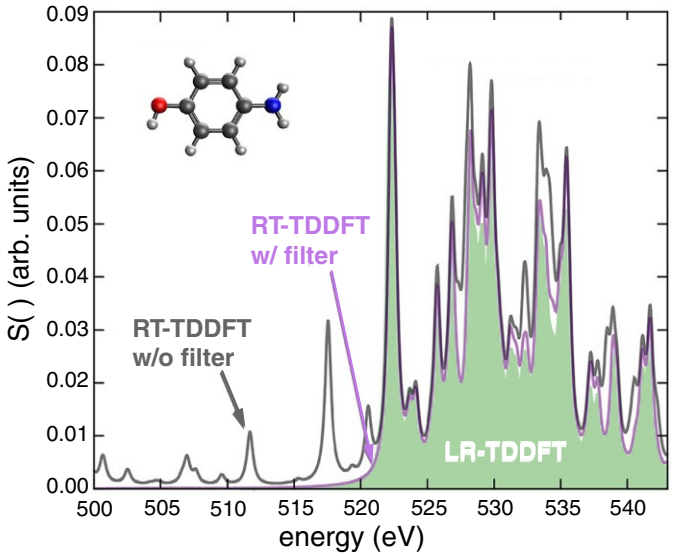


**FIG. 3.16** Absorption spectrum of 4-aminophenol at the oxygen K edge (PBE0/def2-TZVP level), illustrating the appearance of preedge intruder peaks in the RT-TDDFT spectrum without filtering that are not present in the LR-TDDFT spectrum, which is shaded. These intruders can be suppressed in the RT-TDDFT spectrum by filtering the dipole moment function. *(Reproduced with permission from Yang, M.; Sissay, A.; Chen, M.; Lopata, K. Intruder Peak-Free Transient Inner-Shell Spectra Using Real-Time Simulations. J. Chem. Theory Comput.* **2022**, *18, 992–1002; copyright 2022 American Chemical Society.)*

N(1s) excitations. This filtering procedure does require the user to decide in advance which edges are of interest, although all of the edges can be filtered (without significant overhead) in a single TDKS calculation.

The TDKS approach has been extended to compute excited-state absorption spectra *(439, 473)*, using an excited-state density prepared via LR-TDDFT for the initial density at $t = 0$. Because the initial state is nonstationary, this requires that the "field-on" simulation be referenced to a time-evolving "field-off" simulation *(439)*. This approach has recently been applied to simulate emerging transient X-ray experiments *(474–477)*, carried out at free-electron laser facilities using X-ray pulses with femtosecond time resolution. As an example, it is possible to follow metal-to-metal CT dynamics in the mixed-valence $[(CN)_5Fe^{II}CNRu^{III}(NH_3)_5]^-$ compound, which occur on a ~60 fs timescale following excitation at 800 nm, using time-resolved X-ray emission spectroscopy at the iron K edge ($2p_{3/2} \rightarrow 1s$ transition at 7114 eV) *(477)*.

## Acknowledgment

The author's work on excited-state DFT has been supported for many years by the US National Science Foundation, at present under grant no. CHE-1955282.

## References

1. Pople, J. A.; Gill, P. M. W.; Johnson, B. G. Kohn-Sham Density-Functional Theory Within a Finite Basis Set. *Chem. Phys. Lett.* **1992**, *199*, 557–560.
2. Gill, P. M. W.; Johnson, B. G.; Pople, J. A.; Frisch, M. J. The Performance of the Becke-Lee-Yang-Parr (B-LYP) Density Functional Theory With Various Basis Sets. *Chem. Phys. Lett.* **1992**, *197*, 499–505.
3. Johnson, B. G.; Gill, P. M. W.; Pople, J. A. Preliminary Results on the Performance of a Family of Density Functional Methods. *J. Chem. Phys.* **1992**, *97*, 7846–7848.
4. Johnson, B. G.; Gill, P. M. W.; Pople, J. A. The Performance of a Family of Density Functional Methods. *J. Chem. Phys.* **1993**, *98*, 5612–5626.
5. Murray, C. W.; Laming, G. J.; Handy, N. C.; Amos, R. D. Kohn-Sham Bond Lengths and Frequencies Calculated With Accurate Quadrature and Large Basis Sets. *Chem. Phys. Lett.* **1992**, *199*, 551–556.
6. Laming, G. J.; Handy, N. C.; Amos, R. D. Kohn-Sham Calculations on Open-Shell Diatomic Molecules. *Mol. Phys.* **1993**, *80*, 1121–1134.
7. Weiss, H.; Ahlrichs, R.; Häser, M. A Direct Algorithm for Self-Consistent-Field Linear Response Theory and Application to $C_{60}$: Excitation Energies, Oscillator Strengths, and Frequency-Dependent Polarizabilities. *J. Chem. Phys.* **1993**, *99*, 1262–1270.
8. Bauernschmitt, R.; Ahlrichs, R. Treatment of Electronic Excitations Within the Adiabatic Approximation of Time Dependent Density Functional Theory. *Chem. Phys. Lett.* **1996**, *256*, 454–464.
9. Petersilka, M.; Gossmann, U. J.; Gross, E. K. U. Excitation Energies From Time-Dependent Density-Functional Theory. *Phys. Rev. Lett.* **1996**, *76*, 1212–1215.
10. Stratmann, R. E.; Scuseria, G. E.; Frisch, M. J. An Efficient Implementation of Time-Dependent Density-Functional Theory for the Calculation of Excitation Energies of Large Molecules. *J. Chem. Phys.* **1998**, *109*, 8218–8224.
11. Hirata, S.; Head-Gordon, M. Time-Dependent Density Functional Theory Within the Tamm-Dancoff Approximation. *Chem. Phys. Lett.* **1999**, *314*, 291–299.
12. Grabo, T.; Petersilka, M.; Gross, E. K. U. Molecular Excitation Energies From Time-Dependent Density Functional Theory. *J. Mol. Struct. (Theochem)* **2000**, *501–502*, 353–367.
13. Casida, M. E. Time-Dependent Density Functional Response Theory for Molecules. In *Recent Advances in Density Functional Methods, Part I*; Chong, D. P., Ed.; Recent Advances in Computational Chemistry, Vol. I; World Scientific: River Edge, NJ, 1995; pp. 155–192. Chapter 5.
14. Casida, M. E. Time-Dependent Density Functional Response Theory of Molecular Systems: Theory, Computational Methods, and Functionals. In *Theoretical and Computational Chemistry*; Seminario, J. M., Ed.; Recent Developments and Applications of Modern Density Functional Theory, Vol. 4; Elsevier: Amsterdam, 1996; pp. 391–439.
15. Furche, F. On the Density Matrix Based Approach to Time-Dependent Density Functional Response Theory. *J. Chem. Phys.* **2001**, *114*, 5982–5992.
16. McLachlan, A.; Ball, M. Time-Dependent Hartree-Fock Theory for Molecules. *Rev. Mod. Phys.* **1964**, *36*, 844–855.
17. Maitra, N. T. Perspective: Fundamental Aspects of Time-Dependent Density Functional Theory. *J. Chem. Phys.* **2016**, *144*, 220901.
18. Laurent, A. D.; Jacquemin, D. TD-DFT Benchmarks: A Review. *Int. J. Quantum Chem.* **2013**, *113*, 2019–2039.
19. Furche, F.; Rappoport, D. Density Functional Methods for Excited States: Equilibrium Structure and Electronic Spectra. In *Computational Photochemistry*; Olivucci, M., Ed.; Theoretical and Computational Chemistry, Vol. 16; Elsevier: Amsterdam, 2005; pp. 93–128. Chapter 3.
20. Hirata, S.; Head-Gordon, M.; Bartlett, R. J. Configuration Interaction Singles, Time-Dependent Hartree-Fock, and Time-Dependent Density Functional Theory for the Electronic Excited States of Extended Systems. *J. Chem. Phys.* **1999**, *111*, 10774–10786.
21. Casida, M. E. Time-Dependent Density-Functional Theory for Molecules and Molecular Solids. *J. Mol. Struct. (Theochem)* **2009**, *914*, 3–18.
22. Ullrich, C. A.; Yang, Z. H. Excitons in Time-Dependent Density-Functional Theory. In *Density-Functional Methods for Excited States*; Ferré, N., Filatov, M., Eds.; *Topics in Current Chemistry*, Vol. 368; Springer International Publishing: Switzerland, 2016; pp. 185–218.

23. Tapavicza, E.; Bellchambers, G. D.; Vincent, J. C.; Furche, F. Ab Initio Non-Adiabatic Molecular Dynamics. *Phys. Chem. Chem. Phys.* **2013**, *15*, 18336–18348.
24. Barbatti, M.; Crespo-Otero, R. Surface Hopping Dynamics With DFT Excited States. In *Density-Functional Methods for Excited States*; Ferré, N., Filatov, M., Huix-Rotllant, M., Eds.; Topics in Current Chemistry, Vol. 368; Springer International Publishing: Switzerland, 2016; pp. 415–444.
25. Parker, S. M.; Roy, S.; Furche, F. Multistate Hybrid Time-Dependent Density Functional Theory With Surface Hopping Accurately Captures Ultrafast Thymine Photodeactivation. *Phys. Chem. Chem. Phys.* **2019**, *21*, 18999–19010.
26. Zhang, X.; Herbert, J. M. Nonadiabatic Dynamics With Spin-Flip Versus Linear-Response Time-Dependent Density Functional Theory: A Case Study for the Protonated Schiff Base $C_5H_6NH_2^+$. *J. Chem. Phys.* **2021**, *155*, 124111.
27. Herbert, J. M.; Mandal, A. Spin-Flip TDDFT for Photochemistry. In *Time-Dependent Density-Functional Theory: Nonadiabatic Molecular Dynamics*; Zhu, C., Ed, 1st; Jenny Stanford, 2023; pp. 361–404. Chapter 10.
28. Huix-Rotllant, M.; Nikiforov, A.; Thiel, W.; Filatov, M. Description of Conical Intersections With Density Functional Methods. In *Density-Functional Methods for Excited States*; Ferré, N., Filatov, M., Huix-Rotllant, M., Eds.; Topics in Current Chemistry, Vol. 368; Springer International Publishing: Switzerland, 2016; pp. 445–476.
29. Gozem, S.; Huntress, M.; Schapiro, I.; Lindh, R.; Granovsky, A. A.; Angeli, C.; Olivucci, M. Dynamic Electron Correlation Effects on the Ground State Potential Energy Surface of a Retinal Chromophore Model. *J. Chem. Theory Comput.* **2012**, *8*, 4069–4080.
30. Gozem, S.; Melaccio, F.; Lindh, R.; Krylov, A. I.; Granovsky, A. A.; Angeli, C.; Olivucci, M. Mapping the Excited State Potential Energy Surface of a Retinal Chromophore With Multireference and Equation-of-Motion Coupled-Cluster Methods. *J. Chem. Theory Comput.* **2013**, *9*, 4495–4506.
31. Gozem, S.; Melaccio, F.; Valentini, A.; Filatov, M.; Huix-Rotllant, M.; Ferré, N.; Frutos, L. M.; Angeli, C.; Krylov, A. I.; Granovsky, A. A.; Lindh, R.; Olivucci, M. Shape of Multireference, Equation-of-Motion Coupled-Cluster, and Density Functional Theory Potential Energy Surfaces at a Conical Intersection. *J. Chem. Theory Comput.* **2014**, *10*, 3074–3084.
32. Park, W.; Lee, S.; Huix-Rotllant, M.; Filatov, M.; Choi, C. H. Impact of the Dynamic Electron Correlation on the Unusually Long Excited-State Lifetime of Thymine. *J. Phys. Chem. Lett.* **2021**, *12*, 4339–4346.
33. Runge, E.; Gross, E. K. U. Density-Functional Theory for Time-Dependent Systems. *Phys. Rev. Lett.* **1984**, *52*, 997–1000.
34. Gross, E. K. U.; Ullrich, C. A.; Gossmann, U. J. Density Functional Theory of Time-Dependent Systems. In *Density Functional Theory*; Gross, E. K. U., Dreizler, R. M., Eds.; Plenum Press: New York, 1995; pp. 149–171.
35. van Leeuwen, R. Mapping From Densities to Potentials in Time-Dependent Density-Functional Theory. *Phys. Rev. Lett.* **1999**, *82*, 3863–3866.
36. Gross, E. K. U.; Maitra, N. T. Introduction to TDDFT. In *Fundamentals of Time-Dependent Density Functional Theory*; Marques, M. A. L., Maitra, N. T., Nogueira, F. M. S., Gross, E. K. U., Rubio, A., Eds.; Lecture Notes in Physics, Vol. 837; Springer-Verlag: Heidelberg, 2012; pp. 53–97. Chapter 1.
37. Ruggenthaler, M.; van Leeuwen, R. Beyond the Runge-Gross Theorem. In *Fundamentals of Time-Dependent Density Functional Theory*; Marques, M. A. L., Maitra, N. T., Nogueira, F. M. S., Gross, E. K. U., Rubio, A., Eds.; Lecture Notes in Physics, Vol. 837; Springer-Verlag: Berlin, 2012; pp. 187–210. Chapter 9.
38. Ruggenthaler, M.; Penz, M.; van Leeuwen, R. Existence, Uniqueness, and Construction of the Density-Potential Mapping in Time-Dependent Density-Functional Theory. *J. Phys. Condens. Matt.* **2015**, *27*, 203202.
39. Baer, R.; Kronik, L. Time-Dependent Generalized Kohn-Sham Theory. *Eur. Phys. J. B* **2018**, *91*, 170.
40. Koch, W.; Holthausen, M. C. *A Chemist's Guide to Density Functional Theory*, 2nd ed.; Wiley-VCH: New York, 2001.
41. Gross, E. K. U.; Burke, K. Basics. In *Time-Dependent Density Functional Theory*; Marques, M. A. L., Ullrich, C. A., Nogueira, F., Rubio, A., Burke, K., Gross, E. K. U., Eds.; *Lecture Notes in Physics*, Vol. 706; Springer-Verlag: Berlin, 2006; pp. 1–17. Chapter 1.
42. Maitra, N. T. Initial-State Dependence and Memory. In *Time-Dependent Density Functional Theory*; Marques, M. A. L., Ullrich, C. A., Nogueira, F., Rubio, A., Burke, K., Gross, E. K. U., Eds.; *Lecture Notes in Physics*, Vol. 706; Springer-Verlag: Berlin, 2006; pp. 61–74. Chapter 4.
43. Maitra, N. T. Memory: History, Initial-State Dependence, and Double-Excitations. In *Fundamentals of Time-Dependent Density Functional Theory*; Marques, M. A. L., Maitra, N. T., Nogueira, F. M. S., Gross, E. K. U., Rubio, A., Eds.; Lecture Notes in Physics, Vol. 837; Springer-Verlag: Berlin, 2012; pp. 167–184. Chapter 8.
44. McHale, J. L. *Molecular Spectroscopy*; Prentice Hall: Upper Saddle River, NJ, 1999.
45. Moitra, R. K.; Mukherjee, P. K. Self Consistent Calculation of Dynamic Multipole Polarizabilities and Excited State Wave Functions of Open Shell Ions: Li Sequence. *Int. J. Quantum Chem.* **1972**, *6*, 211–224.
46. Roy, H. P.; Gupta, A.; Mukherjee, P. K. Frequency-Dependent Polarizability of Open-Shell Atomic Systems. *Int. J. Quantum Chem.* **1975**, *9*, 75–81.
47. Yabana, K.; Bertsch, G. F. Application of the Time-Dependent Local Density Approximation to Optical Activity. *Phys. Rev. A* **1999**, *60*, 1271–1279.
48. Yabana, K.; Nakatsukasa, T.; Iwata, J. I.; Bertsch, G. F. Real-Time, Real-Space Implementation of the Linear Response Time-Dependent Density Functional Theory. *Phys. Stat. Sol. B* **2006**, *243*, 1121–1138.
49. Zangwill, A.; Soven, P. Density-Functional Approach to Local-Field Effects in Finite Systems: Photoabsorbtion in the Rare Gases. *Phys. Rev. A* **1980**, *21*, 1561–1572.
50. Ullrich, C. A. Excitation Energies in Time-Dependent (Current-) Density-Functional Theory: A Simple Perspective. *J. Chem. Theory Comput.* **2009**, *5*, 859–865.
51. Provorse, M. R.; Isborn, C. M. Electron Dynamics With Real-Time Time-Dependent Density Functional Theory. *Int. J. Quantum Chem.* **2016**, *116*, 739–749.
52. Li, X.; Govind, N.; Isborn, C.; DePrince, I. I. I.; A.E.; Lopata, K. Real-Time Time-Dependent Electronic Structure Theory. *Chem. Rev.* **2020**, *120*, 9951–9993.

53. Ullrich, C. A.; Bandrauk, A. D. Atoms and Molecules in Strong Laser Fields. In *Fundamentals of Time-Dependent Density Functional Theory*; Marques, M. A. L., Maitra, N. T., Nogueira, F. M. S., Gross, E. K. U., Rubio, A., Eds.; Lecture Notes in Physics, Vol. 837; Springer-Verlag: Berlin, 2012; pp. 351–371. Chapter 18.
54. Lépine, F. Short-Pulse Physics. In *Fundamentals of Time-Dependent Density Functional Theory*; Marques, M. A. L., Maitra, N. T., Nogueira, F. M. S., Gross, E. K. U., Rubio, A., Eds.; Lecture Notes in Physics, Vol. 837; Springer-Verlag: Berlin, 2012; pp. 3–14. Chapter 1.
55. Nisoli, M.; Decleva, P.; Calegari, F.; Palacios, A.; Martín, F. Attosecond Electron Dynamics in Molecules. *Chem. Rev.* **2017**, *117*, 10760–10825.
56. Palacios, A.; Martín, F. The Quantum Chemistry of Attosecond Molecular Science. *WIREs Comput. Mol. Sci.* **2020**, *10*, e1430.
57. Ramasesha, K.; Leone, S. R.; Neumark, D. M. Real-Time Probing of Electron Dynamics Using Attosecond Time-Resolved Spectroscopy. *Annu. Rev. Phys. Chem.* **2016**, *67*, 41–63.
58. Capelle, K. A Bird's-Eye View of Density-Functional Theory. *Braz. J. Phys.* **2006**, *36*, 1318–1343.
59. Szabo, A.; Ostlund, N. S. *Modern Quantum Chemistry*; Macmillan: New York, 1982.
60. von Barth, U. Basic Density-Functional Theory—An Overview. *Phys. Scr.* **2004**, *T109*, 9–39.
61. Mardirossian, N.; Head-Gordon, M. Thirty Years of Density Functional Theory in Computational Chemistry: An Overview and Extensive Assessment of 200 Density Functionals. *Mol. Phys.* **2017**, *115*, 2315–2372.
62. Jacobsen, H.; Cavallo, L. Directions for Use of Density Functional Theory: A Short Instruction Manual for Chemists. In *Handbook of Computational Chemistry*; Leszczynski, J., Ed.; Vol. 1; Springer International Publishing: Switzerland, 2017; pp. 225–267. Chapter 6.
63. Ullrich, C. *Time-Dependent Density-Functional Theory: Concepts and Applications*; Oxford University Press: New York, 2012.
64. Marques, M. A. L.; Gross, E. K. U. Time-Dependent Density Functional Theory. In *A Primer in Density Functional Theory*; Fiolhais, C., Nogueira, F., Marques, M. A. L., Eds.; Lecture Notes in Physics, Vol. 620; Springer-Verlag: Berlin, 2003; pp. 144–184. Chapter 4.
65. Marques, M. A. L.; Gross, E. K. U. Time-Dependent Density Functional Theory. *Annu. Rev. Phys. Chem.* **2004**, *55*, 427–455.
66. Dreuw, A.; Head-Gordon, M. Single-Reference Ab Initio Methods for the Calculation of Excited States of Large Molecules. *Chem. Rev.* **2005**, *105*, 4009–4037.
67. Elliott, P.; Furche, F.; Burke, K. Excited States From Time-Dependent Density Functional Theory. In *Reviews in Computational Chemistry*; Lipkowitz, K. B., Cundari, T. R., Eds.; Wiley-VCH: New York, 2009; pp. 91–165. Chapter 3.
68. Casida, M. E.; Huix-Rotllant, M. Progress in Time-Dependent Density-Functional Theory. *Annu. Rev. Phys. Chem.* **2012**, *63*, 287–323.
69. Jacquemin, D.; Perpète, E. A.; Ciofini, I.; Adamo, C. Accurate Simulation of Optical Properties in Dyes. *Acc. Chem. Res.* **2009**, *42*, 326–334.
70. Adamo, C.; Jacquemin, D. The Calculations of Excited-State Properties With Time-Dependent Density Functional Theory. *Chem. Soc. Rev.* **2013**, *42*, 845–856.
71. Laurent, A. D.; Adamo, C.; Jacquemin, D. Dye Chemistry With Time-Dependent Density Functional Theory. *Phys. Chem. Chem. Phys.* **2014**, *16*, 14334–14356.
72. Jacquemin, D.; Adamo, C. Computational Molecular Electronic Spectroscopy With TD-DFT. In *Density-Functional Methods for Excited States*; Ferré, N., Filatov, M., Eds.; *Topics in Current Chemistry*, Vol. 368; Springer: Switzerland, 2016; pp. 347–376.
73. Santoro, F.; Jacquemin, D. Going Beyond the Vertical Approximation With Time-Dependent Density Functional Theory. *WIREs Comput. Mol. Sci.* **2016**, *6*, 460–486.
74. Charaf-Eddin, A.; Planchat, A.; Mennucci, B.; Adamo, C.; Jacquemin, D. Choosing a Functional for Computing Absorption and Fluorescence Band Shapes With TD-DFT. *J. Chem. Theory Comput.* **2013**, *9*, 2749–2760.
75. Ziegler, T.; Seth, M.; Krykunov, M.; Autschbach, J.; Wang, F. On the Relation Between Time-Dependent and Variational Density Functional Theory Approaches for the Deterimination of Excitation Energies and Transition Moments. *J. Chem. Phys.* **2009**, *130*, 154102.
76. Herbert, J. M.; Head-Gordon, M. Curvy-Steps Approach to Constraint-Free Extended-Lagrangian *Ab Initio* Molecular Dynamics, Using Atom-Centered Basis Functions: Convergence Toward Born-Oppenheimer Trajectories. *J. Chem. Phys.* **2004**, *121*, 11542–11556.
77. Rowe, D. J. Equations-of-Motion Method and the Extended Shell Model. *Rev. Mod. Phys.* **1968**, *40*, 153–166.
78. Oddershede, J.; Jørgensen, P.; Yeager, D. L. Polarization Propagator Methods in Atomic and Molecular Calculations. *Comput. Phys. Rep.* **1984**, *2*, 33–92.
79. Olsen, J.; Jensen, H. J. A.; Jørgensen, P. Solution of the Large Matrix Equations Which Occur in Response Theory. *J. Comput. Phys.* **1988**, *74*, 265–282.
80. Furche, F.; Krull, B. T.; Nguyen, B. D.; Kwon, J. Accelerating Molecular Property Calculations With Nonorthonormal Krylov Space Methods. *J. Chem. Phys.* **2016**, *144*, 174105.
81. Vecharynski, E.; Brabec, J.; Shao, M.; Govind, N.; Yang, C. Efficient Block Preconditioned Eigensolvers for Linear Response Time-Dependent Density Functional Theory. *Comput. Phys. Commun.* **2017**, *221*, 42–52.
82. Zhou, Z.; Parker, S. M. Accelerating Molecular Property Calculations With Semiempirical Preconditioning. *J. Chem. Phys.* **2021**, *155*, 204111.
83. Gao, M.; Paul, S.; Schwieters, C. D.; You, Z. Q.; Shao, H.; Herbert, J. M.; Parquette, J. R.; Jaroniec, C. P. An Structural Model for a Self-Assembled Nanotube Provides Insight into Its Exciton Dynamics. *J. Phys. Chem. C* **2015**, *119*, 13948–13956.
84. Casida, M. E. Jacob's Ladder for Time-Dependent Density-Functional Theory: Some Rungs on the Way to Photochemical Heaven. In *Low-Lying Potential Energy Surfaces*; Hoffmann, M. R., Dyall, K. G., Eds.; ACS Symposium Series, Vol. 828; American Chemical Society: Washington, DC, 2002; pp. 199–220. Chapter 9.
85. You, Z. Q.; Hsu, C. P. Theory and Calculation for the Electronic Coupling in Excitation Energy Transfer. *Int. J. Quantum Chem.* **2014**, *114*, 102–115.
86. Furche, F.; Ahlrichs, R.; Wachsmann, C.; Weber, E.; Sobanski, A.; Vögtle, F.; Grimme, S. Circular Dichroism of Helicenes Investigated by Time-Dependent Density Functional Theory. *J. Am. Chem. Soc.* **2000**, *122*, 1717–1724.
87. Luzanov, A. V.; Zhikol, O. A. Electron Invariants and Excited State Structural Analysis for Electronic Transitions Within CIS, RPA, and TDDFT Models. *Int. J. Quantum Chem.* **2010**, *110*, 902–924.

88. Ullah, N.; Rowe, D. J. Properties of Real RPA Matrices and a Simple Diagonalization Procedure. *Nucl. Phys. A* **1971**, *A163*, 257–264.
89. McCurdy, C. W.; Cusachs, L. C. Simplification of the RPA Secular Equation. *J. Chem. Phys.* **1971**, *55*, 1994–1995.
90. Thouless, D. J. Stability Conditions and Nuclear Rotations in the Hartree-Fock Theory. *Nucl. Phys.* **1960**, *21*, 225–232.
91. Čížek, J.; Paldus, J. Stability Conditions for the Solutions of the Hartree-Fock Equations for Atomic and Molecular Systems. Application to the Pi-Electron Model of Cyclic Polyenes. *J. Chem. Phys.* **1967**, *47*, 3976–3985.
92. Casida, M. E.; Huix-Rotllant, M. Many-Body Perturbation Theory (MBPT) and Time-Dependent Density-Functional Theory (TD-DFT): MBPT Insights About What Is Missing in, and Corrections to, the TD-DFT Adiabatic Approximation. In *Density-Functional Methods for Excited States*; Ferré, N., Filatov, M., Eds.; *Topics in Current Chemistry*, Vol. 368; Springer International Publishing: Switzerland, 2016; pp. 1–60.
93. Authier, J.; Loos, P. F. Dynamical Kernels for Optical Excitations. *J. Chem. Phys.* **2020**, *153*, 184105.
94. Ortiz, J. V. Interpreting Bonding and Spectra With Correlated, One-Electron Concepts From Electron Propagator Theory. *Annu. Rep. Comput. Chem.* **2017**, *13*, 139–182.
95. Maitra, N. T.; Zhang, F.; Cave, R. J.; Burke, K. Double Excitations Within Time-Dependent Density Functional Theory Linear Response. *J. Chem. Phys.* **2004**, *120*, 5932–5937.
96. Burke, K.; Werschnik, J.; Gross, E. K. U. Time-Dependent Density Functional Theory: Past, Present, and Future. *J. Chem. Phys.* **2005**, *123*, 062206.
97. Tozer, D. J.; Handy, N. C. On the Determination of Excitation Energies Using Density Functional Theory. *Phys. Chem. Chem. Phys.* **2000**, *2*, 2117–2121.
98. Thiele, M.; Kümmel, S. Photoabsorption Spectra From Adiabatically Exact Time-Dependent Density-Functional Theory in Real Time. *Phys. Chem. Chem. Phys.* **2009**, *11*, 4631–4639.
99. Elliott, P.; Goldson, S.; Canahui, C.; Maitra, N. T. Perspective on Double-Excitations in TDDFT. *Chem. Phys.* **2011**, *391*, 110–119.
100. Foresman, J. B.; Head-Gordon, M.; Pople, J. A.; Frisch, M. J. Toward a Systematic Molecular Orbital Theory for Excited States. *J. Phys. Chem.* **1992**, *96*, 135–149.
101. Casida, M. E.; Jamorski, C.; Bohr, F.; Guan, J.; Salahub, D. R. Optical Properties From Density-Functional Theory. In *Nonlinear Optical Materials*; Karna, S. P., Yeates, A. T., Eds.; *ACS Symposium Series*, Vol. 628; American Chemical Society: Washington, DC, 1996; pp. 145–163. Chapter 8.
102. Jamorski, C.; Casida, M. E.; Salahub, D. R. Dynamic Polarizabilities and Excitation Spectra From a Molecular Implementation of Time-Dependent Density-Functional Response Theory: $N_2$ as a Case Study. *J. Chem. Phys.* **1996**, *104*, 5134–5147.
103. Scuseria, G. E.; Henderson, T. M.; Sorensen, D. C. The Ground State Correlation Energy of the Random Phase Approximation From a Ring Coupled Cluster Doubles Approach. *J. Chem. Phys.* **2008**, *129*, 231101.
104. Jansen, G.; Liu, R. F.; Ángyán, J. G. On the Equivalence of Ring-Coupled Cluster and Adiabatic Connection Fluctuation-Dissipation Theorem Random Phase Approximation Correlation Energy Expressions. *J. Chem. Phys.* **2010**, *133*, 154106.
105. Heßelmann, A.; Görling, A. Random-Phase Approximation Correlation Methods for Molecules and Solids. *Mol. Phys.* **2011**, *109*, 2473–2500.
106. Ren, X.; Rinke, P.; Joas, C.; Scheffler, M. Random-Phase Approximation and Its Applications in Computational Chemistry and Materials Science. *J. Mater. Sci.* **2012**, *47*, 7447–7471.
107. Eshuis, H.; Bates, J. E.; Furche, F. Electron Correlation Methods Based on the Random Phase Approximation. *Theor. Chem. Acc.* **2012**, *131*, 1084.
108. Scuseria, G. E.; Henderson, T. M.; Bulik, I. W. Particle-Particle and Quasiparticle Random Phase Approximations: Connections to Coupled Cluster Theory. *J. Chem. Phys.* **2013**, *139*, 104113.
109. Chen, G. P.; Voora, V. K.; Agee, M. M.; Balasubramani, S. G.; Furche, F. Random-Phase Approximation Methods. *Annu. Rev. Phys. Chem.* **2017**, *68*, 421–445.
110. Berkelbach, T. C. Communication: Random-Phase Approximation Excitation Energies From Approximate Equation-of-Motion Coupled-Cluster Doubles. *J. Chem. Phys.* **2018**, *149*, 041103.
111. Harris, R. A. Oscillator Strengths and Rotational Strengths in Hartree-Fock Theory. *J. Chem. Phys.* **1969**, *50*, 3947–3951.
112. Herbert, J. M.; Jacobson, L. D. Structure of the Aqueous Electron: Assessment of One-Electron Pseudopotential Models in Comparison to Experimental Data and Time-Dependent Density Functional Theory. *J. Phys. Chem. A* **2011**, *115*, 14470–14483.
113. Chantzis, A.; Laurent, A. D.; Adamo, C.; Jacquemin, D. Is the Tamm-Dancoff Approximation Reliable for the Calculation of Absorption and Fluorescence Band Shapes? *J. Chem. Theory Comput.* **2013**, *9*, 4517–4525.
114. Cai, Z. L.; Reimers, J. R. Application of Time-Dependent Density-Functional Theory to the $^3\Sigma_u^-$ First Excited State of $H_2$. *J. Chem. Phys.* **2000**, *112*, 527–530.
115. Casida, M. E.; Gutierrez, F.; Guan, J.; Gadea, F. X.; Salahub, D.; Daudey, J. P. Charge-Transfer Correction for Improved Time-Dependent Local Density Approximation Excited-State Potential Energy Curves: Analysis Within the Two-Level Model With Illustration for $H_2$ and LiH. *J. Chem. Phys.* **2000**, *114*, 7062–7071.
116. Myneni, H.; Casida, M. E. On the Calculation of $\Delta\langle \hat{S}^2 \rangle$ for Electronic Excitations in Time-Dependent Density-Functional Theory. *Comput. Phys. Commun.* **2017**, *213*, 72–91.
117. Hait, D.; Rettig, A.; Head-Gordon, M. Beyond the Coulson-Fischer Point: Characterizing Single Excitation CI and TDDFT for Excited States in Single Bond Dissociations. *Phys. Chem. Chem. Phys.* **2019**, *21*, 21761–21775.
118. Ball, M. A.; McLachlan, A. D. Time-Dependent Hartree-Fock Theory. II. The Electron-Pair Bond. *Mol. Phys.* **1964**, *7*, 501–513.
119. Koutecký, J. Unrestricted Hartree-Fock Solutions for Closed-Shell Molecules. *J. Chem. Phys.* **1967**, *46*, 2443–2445.
120. Dunning, T. H., Jr.; McKoy, V. Nonempirical Calculations on Excited States: The Formaldehyde Molecule. *J. Chem. Phys.* **1968**, *48*, 5263–5270.
121. Jordan, K. D. Use of Unrestricted Hartree-Fock Wave Functions in RPA Calculations. *Int. J. Quantum Chem. Symp.* **1973**, *7*, 491–504.

122. Matsuoka, O.; Ito, H. Random-Phase-Approximation Calculations on Triplet Spectra of Conjugated Molecules. *Theor. Chem. Acc.* **1975**, *39*, 111–118.
123. Niyogi, R. G.; Sannigrahi, A. B. On the Triplet Instability in Semiempirical RPA Calculations of Conjugated Hydrocarbons. *Int. J. Quantum Chem.* **1978**, *14*, 337–340.
124. Chambaud, G.; Levy, B.; Millie, P. Ab Initio Hartree-Fock Instabilities in Closed-Shell Molecular Systems. *Theor. Chem. Acc.* **1978**, *48*, 103–118.
125. Furche, F.; Ahlrichs, R. Adiabatic Time-Dependent Density Functional Methods for Excited State Properties. *J. Chem. Phys.* **2002**, *117*, 7433–7447.
126. Bauernschmitt, R.; Ahlrichs, R. Stability Analysis for Solutions of the Closed Shell Kohn-Sham Equation. *J. Chem. Phys.* **1996**, *104*, 9047–9052.
127. Goddard, J. D.; Orlova, G. Density Functional Theory With Fractionally Occupied Frontier Orbitals and the Instabilities of the Kohn-Sham Solutions for Defining Radical Transition States: Ring-Opening Reactions. *J. Chem. Phys.* **1999**, *111*, 7705–7712.
128. Orlova, G.; Goddard, J. D. Singularities in the Behavior of Density Functionals in Predictions of Singlet Biradicals: The 1,2-Dichalcogenins. *J. Chem. Phys.* **2000**, *112*, 10085–10094.
129. Orlova, G.; Goddard, J. D. Is Density Functional Theory Free of Spatial Symmetry Breaking? The Case of the Linear Carbon Radical Cations: $C_3^+$, $C_5^+$, $C_7^+$, and $C_9^+$. *Chem. Phys. Lett.* **2002**, *363*, 486–491.
130. Orlova, G.; Goddard, J. D. Practical Failures From the Inclusion of Exact Exchange: How Much Exact Exchange is Appropriate? *Mol. Phys.* **2002**, *100*, 483–497.
131. Lutnæs, O. B.; Helgaker, T.; Jaszuński, M. Spin-Spin Coupling Constants and Triplet Instabilities in Kohn-Sham Theory. *Mol. Phys.* **2010**, *108*, 2579–2590.
132. Cui, G.; Yang, W. Challenges With Range-Separated Exchange-Correlation Functionals in Time-Dependent Density Functional Theory Calculations. *Mol. Phys.* **2010**, *108*, 2745–2750.
133. Sears, J. S.; Koerzdoerfer, T.; Zhang, C. R.; Brédas, J. L. Communication: Orbital Instabilities and Triplet States From Time-Dependent Density Functional Theory and Long-Range Corrected Functionals. *J. Chem. Phys.* **2011**, *135*, 151103.
134. Peach, M. J. G.; Williamson, M. J.; Tozer, D. J. Influence of Triplet Instabilities in TDDFT. *J. Chem. Theory Comput.* **2011**, *7*, 3578–3585.
135. Peach, M. J. G.; Tozer, D. J. Overcoming Low Orbital Overlap and Triplet Instability Problems in TDDFT. *J. Phys. Chem. A* **2012**, *116*, 9783–9789.
136. Peach, M. J. G.; Warner, N.; Tozer, D. J. On the Triplet Instability in TDDFT. *Mol. Phys.* **2013**, *111*, 1271–1274.
137. Bokareva, O. S.; Grell, G.; Bokarev, S. I.; Kühn, O. Tuning Range-Separated Density Functional Theory for Photocatalytic Water Splitting Systems. *J. Chem. Theory Comput.* **2015**, *11*, 1700–1709.
138. Casida, M. E.; Ipatov, A.; Cordova, F. Linear-Response Time-Dependent Density Functional Theory for Open-Shell Molecules. In *Time-Dependent Density Functional Theory*; Marques, M. A. L., Ullrich, C. A., Nogueira, F., Rubio, A., Burke, K., Gross, E. K. U., Eds.; *Lecture Notes in Physics*, Vol. 706; Springer-Verlag: Berlin, 2006; pp. 243–257. Chapter 16.
139. Cordova, F.; Doriol, L. J.; Ipatov, A.; Casida, M. E.; Filippi, C.; Vela, A. Troubleshooting Time-Dependent Density-Functional Theory for Photochemical Applications: Oxirane. *J. Chem. Phys.* **2007**, *127*, 164111.
140. Tapavicza, E.; Tavernelli, I.; Rothlisberger, U.; Filippi, C.; Casida, M. E. Mixed Time-Dependent Density-Functional Theory/Classical Trajectory Surface Hopping Study of Oxirane Photochemistry. *J. Chem. Phys.* **2008**, *129*, 124108.
141. Parker, S. M.; Furche, F. Response Theory and Molecular Properties. In *Frontiers in Quantum Chemistry*; Wójcik, M. J., Nakatsuji, H., Kirtman, B., Ozaki, Y., Eds.; Springer: Singapore, 2018; pp. 69–86. Chapter 4.
142. Van Caillie, C.; Amos, R. D. Geometric Derivatives of Excitation Energies Using SCF and DFT. *Chem. Phys. Lett.* **1999**, *308*, 249–255.
143. Van Caillie, C.; Amos, R. D. Geometric Derivatives of Density Functional Theory Excitation Energies Using Gradient-Corrected Functionals. *Chem. Phys. Lett.* **2000**, *317*, 159–164.
144. Liu, F.; Gan, Z.; Shao, Y.; Hsu, C. P.; Dreuw, A.; Head-Gordon, M.; Miller, B. T.; Brooks, B. R.; Yu, J. G.; Furlani, T. R.; Kong, J. A Parallel Implementation of the Analytic Nuclear Gradient for Time-Dependent Density Functional Theory Within the Tamm-Dancoff Approximation. *Mol. Phys.* **2010**, *108*, 2791–2800.
145. Rappoport, D.; Hutter, J. Excited-State Properties and Dynamics. In *Fundamentals of Time-Dependent Density Functional Theory*; Marques, M. A. L., Maitra, N. T., Nogueira, F. M. S., Gross, E. K. U., Rubio, A., Eds.; Lecture Notes in Physics, Vol. 837; Springer-Verlag: Berlin, 2012; pp. 317–336. Chapter 16.
146. Herbert, J. M.; Zhang, X.; Morrison, A. F.; Liu, J. Beyond Time-Dependent Density Functional Theory Using Only Single Excitations: Methods for Computational Studies of Excited States in Complex Systems. *Acc. Chem. Res.* **2016**, *49*, 931–941.
147. Zhang, X.; Herbert, J. M. Analytic Derivative Couplings for Spin-Flip Configuration Interaction Singles and Spin-Flip Time-Dependent Density Functional Theory. *J. Chem. Phys.* **2014**, *141*, 064104.
148. Zhang, X.; Herbert, J. M. Analytic Derivative Couplings in Time-Dependent Density Functional Theory: Quadratic Response Theory Versus Pseudo-Wavefunction Approach. *J. Chem. Phys.* **2015**, *142*, 064109.
149. Li, Z.; Liu, W. First-Order Nonadiabatic Coupling Matrix Elements Between Excited States: A Lagrangian Formulation at the CIS, RPA, TD-HF, and TD-DFT Levels. *J. Chem. Phys.* **2014**, *141*, 014110.
150. Ou, Q.; Fatehi, S.; Alguire, E.; Shao, Y.; Subotnik, J. E. Derivative Couplings Between TD-DFT Excited States Obtained by Direct Differentiation in the Tamm-Dancoff Approximation. *J. Chem. Phys.* **2014**, *141*, 024114.
151. Ou, Q.; Bellchambers, G. D.; Furche, F.; Subotnik, J. E. First-Order Derivative Couplings Between Excited States From Adiabatic TDDFT Response Theory. *J. Chem. Phys.* **2015**, *142*, 064114.
152. Alguire, E. C.; Ou, Q.; Subotnik, J. E. Calculating Derivative Couplings Between Time-Dependent Hartree-Fock Excited States With Pseudo-Wavefunctions. *J. Phys. Chem. B* **2015**, *119*, 7140–7149.

153. Ou, Q.; Alguire, E. C.; Subotnik, J. E. Derivative Couplings Between Time-Dependent Density Functional Theory Excited States in the Random-Phase Approximation Based on Pseudo-Wavefunctions: Behavior Around Conical Intersections. *J. Phys. Chem. B* **2015**, *119*, 7150–7161.
154. Wang, Z.; Wu, C.; Liu, W. NAC-TDDFT: Time-Dependent Density Functional Theory for Nonadiabatic Couplings. *Acc. Chem. Res.* **2021**, *54*, 3288–3297.
155. Ipatov, A.; Cordova, F.; Doriol, L. J.; Casida, M. E. Excited-State Spin-Contamination in Time-Dependent Density-Functional Theory for Molecules With Open-Shell Ground States. *J. Mol. Struct. (Theochem)* **2009**, *914*, 60–73.
156. Chen, D.; Liu, J.; Ma, H.; Zeng, Q.; Liang, W. Analytical Derivative Techniques for TDDFT Excited-State Properties: Theory and Application. *Sci. China Chem.* **2014**, *57*, 48–57.
157. Handy, N. C.; Schaefer, I. I. I.; H.F. On the Evaluation of Analytic Energy Derivatives for Correlated Wave Functions. *J. Chem. Phys.* **1984**, *81*, 5031–5033.
158. Ronca, E.; Angeli, C.; Belpassi, L.; De Angelis, F.; Tarantelli, F.; Pastore, M. Density Relaxation in Time-Dependent Density Functional Theory: Combining Relaxed Density Natural Orbitals and Multireference Perturbation Theories for an Improved Description of Excited States. *J. Chem. Theory Comput.* **2014**, *10*, 4014–4024.
159. Maschietto, F.; Campetella, M.; Frisch, M. J.; Scalmani, G.; Adamo, C.; Ciofini, I. How Are the Charge Transfer Descriptors Affected by the Quality of the Underpinning Electronic Density? *J. Comput. Chem.* **2018**, *39*, 735–742.
160. Jacquemin, D.; Planchat, A.; Adamo, C.; Mennucci, B. TD-DFT Assessment of Functionals for Optical 0-0 Transitions in Solvated Dyes. *J. Chem. Theory Comput.* **2012**, *8*, 2359–2372.
161. Hanson-Heine, M. W. D.; George, M. W.; Besley, N. A. Assessment of Time-Dependent Density Functional Theory Calculations With the Restricted Space Approximation for Excited State Calculations of Large Systems. *Mol. Phys.* **2018**, *116*, 1452–1459.
162. Besley, N. A. Fast Time-Dependent Density Functional Theory Calculations of the X-Ray Absorption Spectroscopy of Large Systems. *J. Chem. Theory Comput.* **2016**, *12*, 5018–5025.
163. Zhu, Y.; Alam, B.; Herbert, J. M. Broadband X-Ray Absorption Spectra From Time-Dependent Kohn-Sham Calculations. 10.26434/chemrxiv.14766960.v1.
164. Kasper, J. M.; Stetina, T. F.; Jenkins, A. J.; Li, X. Ab Initio Methods for L-Edge X-Ray Absorption Spectroscopy. *Chem. Phys. Rev.* **2020**, *1*, 011304.
165. Besley, N. A. Modeling of the Spectroscopy of Core Electrons With Density Functional Theory. *WIREs Comput. Mol. Sci.* **2021**, *12*, e1527.
166. Norman, P.; Dreuw, A. Simulating X-Ray Spectroscopies and Calculating Core-Excited States of Molecules. *Chem. Rev.* **2018**, *118*, 7208–7248.
167. Besley, N. A. Density Functional Theory Based Methods for the Calculation of X-Ray Spectroscopy. *Acc. Chem. Res.* **2020**, *53*, 1306–1315.
168. Bokarev, S. I.; Kühn, O. Theoretical X-Ray Spectroscopy of Transition Metal Compounds. *WIREs Comput. Mol. Sci.* **2020**, *10*, e1433.
169. Rankine, C. D.; Penfold, T. J. Progress in the Theory of X-Ray Spectroscopy: From Quantum Chemistry to Machine Learning and Ultrafast Dynamics. *J. Phys. Chem. A* **2021**, *125*, 4276–4293.
170. Depresseux, A.; Oliva, E.; Gautier, J.; Tissandier, F.; Nejdl, J.; Kozlova, M.; Maynard, G.; Goddet, J. P.; Tafzi, A.; Lifschitz, A.; Kim, H. T.; Jacquemot, S.; Malka, V.; Phuoc, K. T.; Thaury, C.; Rousseau, P.; Iaquaniello, G.; Lefrou, T.; Flacco, A.; Vodungbo, B.; Lambert, G.; Rousse, A.; Zeitoun, P.; Sebban, S. Table-Top Femtosecond X-Ray Laser by Collisional Ionization Gating. *Nat. Photonics* **2015**, *9*, 817–822.
171. Kleine, C.; Ekimova, M.; Goldsztejn, G.; Raabe, S.; Strüber, C.; Ludwig, J.; Yarlagadda, S.; Eisebitt, S.; Vrakking, M. J. J.; Elsaesser, T.; Nibbering, E. T. J.; Rouzée, A. Soft X-Ray Absorption Spectroscopy of Aqueous Solutions Using a Table-Top Femtosecond Soft X-Ray Source. *J. Phys. Chem. Lett.* **2019**, *10*, 52–58.
172. Schoenlein, R.; Elsaesser, T.; Holldack, K.; Huang, Z.; Kapteyn, H.; Murnane, M.; Woerner, M. Recent Advances in Ultrafast X-Ray Sources. *Phil. Trans. R. Soc. A* **2019**, *377*, 20180384.
173. Geneaux, R.; Marroux, H. J. B.; Guggenmos, A.; Neumark, D. M.; Leone, S. R. Transient Absorption Spectroscopy Using High Harmonic Generation: A Review of Ultrafast X-Ray Dynamics in Molecules and Solids. *Phil. Trans. R. Soc. A* **2019**, *377*, 20170463.
174. Smith, A. D.; Balčiūnas, T.; Chang, Y. P.; Schmidt, C.; Zinchenko, K.; Nunes, F. B.; Rossi, E.; Svoboda, V.; Yin, Z.; Wolf, J. P.; Wörner, H. J. Femtosecond Soft-X-Ray Absorption Spectroscopy of Liquids With a Water-Window High-Harmonic Source. *J. Phys. Chem. Lett.* **2020**, *11*, 1981–1988.
175. Cederbaum, L. S.; Domcke, W.; Schirmer, J. Many-Body Theory of Core Holes. *Phys. Rev. A* **1980**, *22*, 206–222.
176. Barth, A.; Cederbaum, L. S. Many-Body Theory of Core-Valence Excitations. *Phys. Rev. A* **1981**, *23*, 1038–1061.
177. Herbst, M. F.; Fransson, T. Quantifying the Error of the Core-Valence Separation Approximation. *J. Chem. Phys.* **2020**, *153*, 054114.
178. Liang, W.; Fischer, S. A.; Frisch, M. J.; Li, X. Energy-Specific Linear Response TDHF/TDDFT for Calculating High-Energy Excited States. *J. Chem. Theory Comput.* **2011**, *7*, 3540–3547.
179. Perdew, J. P.; Schmidt, K. Jacob's Ladder of Density Functional Approximations for the Exchange-Correlation Energy. In *Density Functional Theory and Its Applications to Materials*; Van Doren, V., Van Alsenoy, C., Geerlings, P., Eds.; *AIP Conference Proceedings*, Vol. 577; American Institute of Physics, 2001; pp. 1–20.
180. Perdew, J. P.; Ruzsinszky, A.; Tao, J.; Staroverov, V. N.; Scuseria, G. E.; Csonka, G. I. Prescription for the Design and Selection of Density Functional Approximations: More Constraint Satisfaction With Fewer Fits. *J. Chem. Phys.* **2005**, *123*, 062201.
181. Perdew, J. P. Climbing the Ladder of Density Functional Approximations. *MRS Bull.* **2013**, *38*, 743–750.
182. Goerigk, L.; Hansen, A.; Bauer, C.; Ehrlich, S.; Najibi, A.; Grimme, S. A Look at the Density Functional Theory Zoo With the Advanced GMTKN55 Database for General Main Group Thermochemistry Kinetics, and Noncovalent Interactions. *Phys. Chem. Chem. Phys.* **2017**, *19*, 32184–32215.
183. Ernzerhof, M.; Scuseria, G. E. Assessment of the Perdew-Burke-Ernzerhof Exchange-Correlation Functional. *J. Chem. Phys.* **1999**, *110*, 5029–5036.
184. Becke, A. D.; Edgecombe, K. E. A Simple Measure of Electron Localization in Atomic and Molecular Systems. *J. Chem. Phys.* **1990**, *92*, 5397–5403.
185. Perdew, J. P.; Constantin, L. A. Laplacian-Level Density Functionals for the Kinetic Energy Density and Exchange-Correlation Energy. *Phys. Rev. B* **2007**, *75*, 155109.

186. Mardirossian, N.; Head-Gordon, M. Characterizing and Understanding the Remarkably Slow Basis Set Convergence of Several Minnesota Density Functionals for Intermolecular Interaction Energies. *J. Chem. Theory Comput.* **2013**, *9*, 4453–4461.
187. Goerigk, L. Testing London-Dispersion Effects With the Latest Minnesota Density Functionals: Problems and Possible Solutions. *J. Phys. Chem. Lett.* **2015**, *6*, 3891–3896.
188. Mardirossian, N.; Head-Gordon, M. How Accurate Are the Minnesota Density Functionals for Noncovalent Interactions, Isomerization Energies, Thermochemistry, and Barrier Heights Involving Molecules Composed of Main-Group Elements? *J. Chem. Theory Comput.* **2016**, *12*, 4303–4325.
189. Dasgupta, S.; Herbert, J. M. Standard Grids for High-Precision Integration of Modern Density Functionals: SG-2 and SG-3. *J. Comput. Chem.* **2017**, *38*, 869–882.
190. Perdew, J. P.; Staroverov, V. N.; Tao, J.; Scuseria, G. E. Density Functional With Full Exact Exchange, Balanced Nonlocality of Correlation, and Constraint Satisfaction. *Phys. Rev. A* **2008**, *78*, 052513.
191. Haunschild, R.; Odashima, M. M.; Scuseria, G. E.; Perdew, J. P.; Capelle, K. Hyper-Generalized-Gradient Functionals Constructed From the Lieb-Oxford Bound: Implementation Via Local Hybrids and Thermochemical Assessment. *J. Chem. Phys.* **2012**, *136*, 184102.
192. Goerigk, L.; Grimme, S. Double-Hybrid Density Functionals. *WIREs Comput. Mol. Sci.* **2014**, *4*, 576–600.
193. Grimme, S.; Neese, F. Double-Hybrid Density Functional Theory for Excited Electronic States of Molecules. *J. Chem. Phys.* **2007**, *127*, 154116.
194. Head-Gordon, M.; Rico, R. J.; Oumi, M.; Lee, T. J. A Doubles Correction to Electronic Excited States From Configuration Interaction in the Space of Single Substitutions. *Chem. Phys. Lett.* **1994**, *219*, 21–29.
195. Head-Gordon, M.; Oumi, M.; Maurice, D. Quasidegenerate Second-Order Perturbation Corrections to Single-Excitation Configuration Interaction. *Mol. Phys.* **1999**, *96*, 593–602.
196. Casanova, D.; Rhee, Y. M.; Head-Gordon, M. Quasidegenerate Scaled Opposite Spin Second Order Perturbation Theory Corrections to Single Excitation Configuration Interaction. *J. Chem. Phys.* **2008**, *128*, 164106.
197. Kronik, L.; Kümmel, S. Dielectric Screening Meets Optimally Tuned Density Functionals. *Adv. Mater.* **2018**, *30*, 1706560.
198. Manna, A. K.; Refaely-Abramson, A.; Reilly, A. M.; Tkatchenko, A.; Neaton, J. B.; Kronik, L. Quantitative Prediction of Optical Absorption in Molecular Solids From an Optimally Tuned Screened Range-Separated Hybrid Functional. *J. Chem. Theory Comput.* **2018**, *14*, 2919–2929.
199. Bhandari, S.; Cheung, M.; Geva, E.; Kronik, L.; Duneitz, B. D. Fundamental Gaps of Condensed-Phase Organic Semiconductors From Single-Molecule Calculations Using Polarization-Consistent Optimally Tuned Screened Range-Separated Hybrid Functionals. *J. Chem. Theory Comput.* **2018**, *14*, 6287–6294.
200. Iikura, H.; Tsuneda, T.; Yanai, T.; Hirao, K. A Long-Range Correction Scheme for Generalized-Gradient-Approximation Exchange Functionals. *J. Chem. Phys.* **2001**, *115*, 3540–3544.
201. Tawada, Y.; Tsuneda, T.; Yanagisawa, S.; Yanai, T.; Hirao, K. A Long-Range Corrected Time-Dependent Density Functional Theory. *J. Chem. Phys.* **2004**, *120*, 8425–8433.
202. Song, J. W.; Hirosawa, T.; Tsuneda, T.; Hirao, K. Long-Range Corrected Density Functional Calculations of Chemical Reactions: Redetermination of Parameter. *J. Chem. Phys.* **2007**, *126*, 154105.
203. Dreuw, A.; Weisman, J. L.; Head-Gordon, M. Long-Range Charge-Transfer Excited States in Time-Dependent Density Functional Theory Require Non-Local Exchange. *J. Chem. Phys.* **2003**, *119*, 2943–2946.
204. Baer, R.; Neuhauser, D. Density Functional Theory With Correct Long-Range Asymptotic Behavior. *Phys. Rev. Lett.* **2005**, *94*, 043002.
205. Song, J. W.; Tokura, S.; Sato, T.; Watson, M. A.; Hirao, K. An Improved Long-Range Corrected Hybrid Exchange-Correlation Functional Including a Short-Range Gaussian Attenuation (LCgau-BOP). *J. Chem. Phys.* **2007**, *127*, 154109.
206. Akinaga, Y.; Ten-no, S. Range-Separation by the Yukawa Potential in Long-Range Corrected Density Functional Theory With Gaussian-Type Basis Functions. *Chem. Phys. Lett.* **2008**, *462*, 348–351.
207. Chai, J. D.; Head-Gordon, M. Optimal Operators for Hartree-Fock Exchange From Long-Range Corrected Hybrid Density Functionals. *Chem. Phys. Lett.* **2008**, *467*, 176–178.
208. Song, J. W.; Yamashita, K.; Hirao, K. Communication: A New Hybrid Exchange Correlation Functional for Band-Gap Calculations Using a Short-Range Gaussian Attenuation (Gaussian-Perdue-Burke-Ernzerhof ). *J. Chem. Phys.* **2011**, *135*, 071103.
209. Song, J. W.; Yamashita, K.; Hirao, K. Gaussian Attenuation Hybrid Scheme Applied to the Ernzerhof-Perdew Exchange Hole Model (Gau-PBEh). *J. Chem. Phys.* **2012**, *137*, 244105.
210. Henderson, T. M.; Izmaylov, A. F.; Scuseria, G. E.; Savin, A. The Importance of Middle-Range Hartree-Fock-Type Exchange for Hybrid Density Functionals. *J. Chem. Phys.* **2007**, *127*, 221103.
211. Song, J. W.; Watson, M. A.; Nakata, A.; Hirao, K. Core-Excitation Energy Calculations With a Long-Range Corrected Hybrid Exchange-Correlation Functional Including a Short-Range Gaussian Attenuation (LCgau-BOP). *J. Chem. Phys.* **2008**, *129*, 184113.
212. Song, J. W.; Watson, M. A.; Hirao, K. An Improved Long-Range Corrected Hybrid Functional With Vanishing Hartree-Fock Exchange at Zero Interelectronic Distance (LC2gau-BOP). *J. Chem. Phys.* **2009**, *131*, 144108.
213. Besley, N. A.; Peach, M. J. G.; Tozer, D. J. Time-Dependent Density Functional Theory Calculations of Near-Edge X-Ray Absorption Fine Structure With Short-Range Corrected Functionals. *Phys. Chem. Chem. Phys.* **2009**, *11*, 10350–10358.
214. Besley, N. A.; Asmuruf, F. A. Time-Dependent Density Functional Theory Calculations of the Spectroscopy of Core Electrons. *Phys. Chem. Chem. Phys.* **2010**, *12*, 12024–12039.
215. Chan, B.; Kawashima, Y.; Hirao, K. The reHISS Three-Range Exchange Functional With an Optimal Variation of Hartree-Fock and Its Use in the reHISSB-D Density Functional Theory Method. *J. Comput. Chem.* **2018**, *40*, 29–38.
216. Chai, J. D.; Head-Gordon, M. Long-Range Corrected Hybrid Density Functionals With Damped Atom-Atom Dispersion Corrections. *Phys. Chem. Chem. Phys.* **2008**, *10*, 6615–6620.
217. Chai, J. D.; Head-Gordon, M. Long-Range Corrected Double-Hybrid Density Functionals. *J. Chem. Phys.* **2009**, *131*, 174105.

218. Mardirossian, N.; Head-Gordon, M. ωB97X-V: A 10-Parameter, Range-Separated Hybrid, Generalized Gradient Approximation Density Functional With Nonlocal Correlation, Designed by a Survival-of-the-Fittest Strategy. *Phys. Chem. Chem. Phys.* **2014**, *16*, 9904–9924.
219. Mardirossian, N.; Head-Gordon, M. ωB97M-V: A Combinatorially Optimized, Range-Separated Hybrid, Meta-GGA Density Functional With VV10 Nonlocal Correlation. *J. Chem. Phys.* **2016**, *144*, 214110.
220. Mardirossian, N.; Head-Gordon, M. Survival of the Most Transferable at the Top of Jacob's Ladder: Defining and Testing the ωB97M(2) Double Hybrid Density Functional. *J. Phys. Chem.* **2018**, *148*, 241736.
221. Peverati, R.; Truhlar, D. G. Improving the Accuracy of Hybrid Meta-GGA Density Functionals by Range Separation. *J. Phys. Chem. Lett.* **2011**, *2*, 2810–2817.
222. Verma, P.; Wang, Y.; Ghosh, S.; He, X.; Truhlar, D. G. Revised M11 Exchange-Correlation Functional for Electronic Excitation Energies and Ground-State Properties. *J. Phys. Chem. A* **2019**, *123*, 2966–2990.
223. Lin, Y. S.; Tsai, C. W.; Li, G. D.; Chai, J. D. Long-Range Corrected Hybrid Meta-Generalized-Gradient Approximations With Dispersion Corrections. *J. Chem. Phys.* **2012**, *136*, 154109.
224. Lin, Y. S.; Li, G. D.; Mao, S. P.; Chai, J. D. Long-Range Corrected Hybrid Density Functionals With Improved Dispersion Corrections. *J. Chem. Theory Comput.* **2013**, *9*, 263–272.
225. Yanai, T.; Tew, D. P.; Handy, N. C. A New Hybrid Exchange-Correlation Functional Using the Coulomb-Attenuating Method (CAM-B3LYP). *Chem. Phys. Lett.* **2004**, *393*, 51–57.
226. Rohrdanz, M. A.; Herbert, J. M. Simultaneous Benchmarking of Ground- and Excited-State Properties With Long-Range-Corrected Density Functional Theory. *J. Chem. Phys.* **2008**, *129*, 034107.
227. Lange, A. W.; Rohrdanz, M. A.; Herbert, J. M. Charge-Transfer Excited States in a π-Stacked Adenine Dimer, as Predicted Using Long-Range-Corrected Time-Dependent Density Functional Theory. *J. Phys. Chem. B* **2008**, *112*, 6304–6308.
228. Rohrdanz, M. A.; Martins, K. M.; Herbert, J. M. A Long-Range-Corrected Density Functional That Performs Well for Both Ground-State Properties and Time-Dependent Density Functional Theory Excitation Energies, Including Charge-Transfer Excited States. *J. Chem. Phys.* **2009**, *130*, 054112.
229. Gill, P. M. W.; Adamson, R. D. A Family of Attenuated Coulomb Operators. *Chem. Phys. Lett.* **1996**, *261*, 105–110.
230. Richard, R. M.; Herbert, J. M. Time-Dependent Density-Functional Description of the $^1L_a$ State in Polycyclic Aromatic Hydrocarbons: Charge-Transfer Character in Disguise? *J. Chem. Theory Comput.* **2011**, *7*, 1296–1306.
231. Alam, B.; Morrison, A. F.; Herbert, J. M. Charge Separation and Charge Transfer in the Low-Lying Excited States of Pentacene. *J. Phys. Chem. C* **2020**, *124*, 24653–24666.
232. Ernzerhof, M.; Perdew, J. P. Generalized Gradient Approximation to the Angle- and System-Averaged Exchange Hole. *J. Chem. Phys.* **1998**, *109*, 3313–3320.
233. Henderson, T. M.; Janesko, B. G.; Scuseria, G. E. Generalized Gradient Approximation Model Exchange Holes for Range-Separated Hybrids. *J. Chem. Phys.* **2008**, *128*, 194105.
234. Heyd, J.; Scuseria, G. E.; Ernzerhof, M. Hybrid Functionals Based on a Screened Coulomb Potential. *J. Chem. Phys.* **2003**, *118*, 8207–8215.
235. Krukau, A. V.; Vydrov, O. A.; Izmaylov, A. F.; Scuseria, G. E. Influence of the Exchange Screening Parameter on the Performance of Screened Hybrid Functionals. *J. Chem. Phys.* **2006**, *125*, 224106.
236. Shao, Y.; Mei, Y.; Sundholm, D.; Kaila, V. R. I. Benchmarking the Performance of Time-Dependent Density Functional Theory Methods on Biochromophores. *J. Chem. Theory Comput.* **2020**, *16*, 587–600.
237. Kim, J.; Hong, K.; Hwang, S. Y.; Ryu, S.; Choi, S.; Kim, W. Y. Effects of the Locality of a Potential Derived From Hybrid Density Functionals on Kohn-Sham Orbitals and Excited States. *Phys. Chem. Chem. Phys.* **2017**, *19*, 10177–10186.
238. Silva-Junior, M. R.; Schreiber, M.; Sauer, S. P. A.; Thiel, W. Benchmarks of Electronically Excited States: Basis Set Effects on CASPT2 Results. *J. Chem. Phys.* **2010**, *133*, 174318.
239. Liang, J.; Feng, X.; Hait, D.; Head-Gordon, M. Revisiting the Performance of Time-Dependent Density Functional Theory for Electronic Excitations: Assessment of 43 Popular and Recently Developed Functionals From Rungs One to Four. *J. Chem. Theory Comput.* **2022**, *18*, 3460–3473.
240. Jacquemin, D.; Wathelet, V.; Perpéte, E. A.; Adamo, C. Extensive TD-DFT Benchmark: Singlet-Excited States of Organic Molecules. *J. Chem. Theory Comput.* **2009**, *5*, 2420–2435.
241. Jacquemin, D.; Perpète, E. A.; Ciofini, I.; Adamo, C. Assessment of Functionals for TD-DFT Calculations of Singlet-Triplet Transitions. *J. Chem. Theory Comput.* **2010**, *6*, 1532–1537.
242. Caricato, M.; Trucks, G. W.; Frisch, M. J.; Wiberg, K. B. Electronic Transition Energies: A Study of the Performance of a Large Range of Single Reference Density Functional and Wave Function Methods on Valence and Rydberg States Compared to Experiment. *J. Chem. Theory Comput.* **2010**, *6*, 370–383.
243. Fabian, J. TDDFT-Calculations of Vis/NIR Absorbing Compounds. *Dyes Pigm.* **2010**, *84*, 36–53.
244. Leang, S. S.; Zahariev, F.; Gordon, M. S. Benchmarking the Performance of Time-Dependent Density Functional Methods. *J. Chem. Phys.* **2012**, *136*, 104101.
245. Wang, Y.; Jin, X.; Yu, H. S.; Truhlar, D. G.; He, X. Revised M06-L Functional for Improved Accuracy on Chemical Reaction Barrier Heights, Noncovalent Interactions, and Solid-State Physics. *Proc. Natl. Acad. Sci. USA* **2017**, *114*, 8487–8492.
246. Loos, P. F.; Jacquemin, D. Evaluating 0-0 Energies With Theoretical Tools: A Short Review. *ChemPhotoChem* **2019**, *3*, 684–696.
247. Zhao, Y.; Truhlar, D. G. Density Functionals With Broad Applicability in Chemistry. *Acc. Chem. Res.* **2008**, *41*, 157–167.
248. Tozer, D. J.; Amos, R. D.; Handy, N. C.; Roos, B. O.; Serrano-Andrés, L. Does Density Functional Theory Contribute to the Understanding of Excited States of Unsaturated Organic Compounds? *Mol. Phys.* **1999**, *97*, 859–868.

249. van Leeuwen, R.; Baerends, E. J. Exchange-Correlation Potential With Correct Asymptotic Behavior. *Phys. Rev. A* **1994**, *49*, 2421–2431.
250. Tozer, D. J.; Handy, N. C. Improving Virtual Kohn-Sham Orbitals and Eigenvalues: Application to Excitation Energies and Static Polarizabilities. *J. Chem. Phys.* **1998**, *109*, 10180–10189.
251. Schipper, P. R. T.; Gritsenko, O. V.; van Gisbergen, S. J. A.; Baerends, E. J. Molecular Calculations of Excitation Energies and (Hyper)Polarizabilities With a Statistical Average of Orbital Model Potentials. *J. Chem. Phys.* **2000**, *112*, 1344–1352.
252. Grüning, M.; Gritsenko, O. V.; van Gisbergen, S. J. A.; Baerends, E. J. Shape Corrections to Exchange-Correlation Potentials by Gradient-Regulated Seamless Connection of Model Potentials for Inner and Outer Region. *J. Chem. Phys.* **2001**, *114*, 652–660.
253. Zhao, Y.; Truhlar, D. G. The M06 Suite of Density Functionals for Main Group Thermochemistry, Thermochemical Kinetics, Noncovalent Interactions, Excited States, and Transition Elements: Two New Functionals and Systematic Testing of Four M06-Class Functionals and 12 Other Functionals. *Theor. Chem. Acc.* **2008**, *120*, 215–241.
254. Adamo, C.; Barone, V. Toward Reliable Density Functional Methods Without Adjustable Parameters: The PBE0 Model. *J. Chem. Phys.* **1999**, *110*, 6158–6170.
255. Becke, A. D. A New Mixing of Hartree-Fock and Local Density-Functional Theories. *J. Chem. Phys.* **1993**, *98*, 1372–1377.
256. Herbert, J. M. Dielectric Continuum Methods for Quantum Chemistry. *WIREs Comput. Mol. Sci.* **2021**, *11*, e1519.
257. Boese, A. D.; Martin, J. M. L. Development of Density Functionals for Thermochemical Kinetics. *J. Chem. Phys.* **2004**, *121*, 3405–3416.
258. Zhao, Y.; Schultz, N. E.; Truhlar, D. G. Design of Density Functionals by Combining the Method of Constraint Satisfaction With Parameterization for Thermochemistry, Thermochemical Kinetics, and Noncovalent Interactions. *J. Chem. Theory Comput.* **2006**, *2*, 364–382.
259. Vydrov, O. A.; Scuseria, G. E. Assessment of a Long-Range Corrected Hybrid Functional. *J. Chem. Phys.* **2006**, *125*, 234109.
260. Lange, A. W.; Herbert, J. M. Both Intra- and Interstrand Charge-Transfer Excited States in B-DNA Are Present at Energies Comparable to, or Just Above, the $^1\pi\pi^*$ Excitonic Bright States. *J. Am. Chem. Soc.* **2009**, *131*, 3913–3922.
261. Herbert, J. M. The Quantum Chemistry of Loosely-Bound Electrons. In Parill, A. L., Lipkowitz, K., Eds.; *Reviews in Computational Chemistry*, Vol. 28; Wiley-VCH: Hoboken, NJ, 2015; pp. 391–517. Chapter 8.
262. Baerends, E. J.; Gritsenko, O. V.; van Meer, R. The Kohn-Sham Gap, the Fundamental Gap and the Optical Gap: The Physical Meaning of Occupied and Virtual Kohn-Sham Orbital Energies. *Phys. Chem. Chem. Phys.* **2013**, *15*, 16408–16425.
263. Refaely-Abramson, S.; Sharifzadeh, S.; Govind, N.; Autschbach, J.; Neaton, J. B.; Baer, R.; Kronik, L. Quasiparticle Spectra From a Nonempirical Optimally Tuned Range-Separated Hybrid Density Functional. *Phys. Rev. Lett.* **2012**, *109*, 226405.
264. van Meer, R.; Gritsenko, O. V.; Baerends, E. J. Physical Meaning of Virtual Kohn-Sham Orbitals and Orbital Energies: An Ideal Basis for the Description of Molecular Excitations. *J. Chem. Theory Comput.* **2014**, *10*, 4432–4441.
265. Luzanov, A. V.; Sukhorukov, A. A.; Umanskii, V. E. Application of Transition Density Matrix for Analysis of Excited States. *Theor. Exp. Chem.* **1974**, *10*, 354–361.
266. Martin, R. L. Natural Transition Orbitals. *J. Chem. Phys.* **2003**, *118*, 4775–4777.
267. Mayer, I. Using Singular Value Decomposition for a Compact Presentation and Improved Interpretation of the CIS Wave Functions. *Chem. Phys. Lett.* **2007**, *437*, 284–286.
268. Surján, P. R. Natural Orbitals in CIS and Singular-Value Decomposition. *Chem. Phys. Lett.* **2007**, *439*, 393–394.
269. Head-Gordon, M.; Graña, A. M.; Maurice, D.; White, C. A. Analysis of Electronic Transitions as the Difference of Electron Attachment and Detachment Densities. *J. Phys. Chem.* **1995**, *99*, 14261–14270.
270. Etienne, T.; Assfeld, X.; Monari, A. Toward a Quantitative Assessment of Electron Transitions' Charge-Transfer Character. *J. Chem. Theory Comput.* **2014**, *10*, 3896–3905.
271. Etienne, T. Theoretical Insights into the Topology of Molecular Excitons From Single-Reference Excited States Calculation Methods. In *Excitons*; Pyshkin, S. L., Ed.; IntechOpen, 2018; pp. 31–54. Chapter 3.
272. Plasser, F.; Wormit, M.; Dreuw, A. New Tools for the Systematic Analysis and Visualization of Electronic Excitations. I. Formalism. *J. Chem. Phys.* **2014**, *140*, 024106.
273. Levy, M.; Perdew, J. P.; Sahni, V. Exact Differential Equation for the Density and Ionization Energy of a Many-Particle System. *Phys. Rev. A* **1984**, *30*, 2745–2748.
274. Almbladh, C. O.; Pedroza, A. C. Density-Functional Exchange-Correlation Potentials and Orbital Eigenvalues for Light Atoms. *Phys. Rev. A* **1984**, *29*, 2322–2330.
275. Almbladh, C. O.; von Barth, U. Exact Results for the Charge and Spin Densities, Exchange-Correlation Potentials, and Density-Functional Eigenvalues. *Phys. Rev. B* **1985**, *31*, 3231–3244.
276. Chermette, H.; Lembarki, A.; Razafinjanahary, H.; Rogemond, F. Gradient-Corrected Exchange Potential Functional With the Correct Asymptotic Behaviour. *Adv. Quantum Chem.* **1999**, *33*, 105–130.
277. Perdew, J. P.; Kurth, S. Density Functionals for Non-Relativistic Coulomb Systems in the New Century. In *Primer in Density Functional Theory*; Fiolhais, C., Nogueira, F., Marques, M. A. L., Eds.; Lecture Notes in Physics, Vol. 620; Springer-Verlag, 2003; pp. 1–55.
278. Almbladh, C. O.; von Barth, U. Density-Functional Theory and Excitation Energies. In *Density Functional Methods in Physics*; Dreizler, R. M., da Providência, J., Eds.; NATO Advanced Science Institutes Series, Vol. 123; Springer, 1985; pp. 209–232.
279. Mulliken, R. S. Molecular Compounds and Their Spectra. II. *J. Am. Chem. Soc.* **1952**, *74*, 811–824.
280. Gritsenko, O.; Baerends, E. J. Asymptotic Correction of the Exchange-Correlation Kernel of Time-Dependent Density Functional Theory for Long-Range Charge-Transfer Excitations. *J. Chem. Phys.* **2004**, *121*, 655–660.

281. Bernasconi, L.; Sprik, M.; Hutter, J. Time Dependent Density Functional Theory Study of Charge-Transfer and Intramolecular Electronic Excitations in Acetone-Water Systems. *J. Chem. Phys.* **2003**, *119*, 12417–12431.
282. Bernasconi, L.; Sprik, M.; Hutter, J. Hartree-Fock Exchange in Time Dependent Density Functional Theory: Application to Charge Transfer Excitations in Solvated Molecular Systems. *Chem. Phys. Lett.* **2004**, *394*, 141–146.
283. Besley, N. A. Calculation of the Electronic Spectra of Molecules in Solution and on Surfaces. *Chem. Phys. Lett.* **2004**, *390*, 124–129.
284. Neugebauer, J.; Louwerse, M. J.; Baerends, E. J.; Wesołowski, T. A. The Merits of the Frozen-Density Embedding Scheme to Model Solvatochromatic Shifts. *J. Chem. Phys.* **2005**, *122*, 094115.
285. Bernasconi, L.; Sprik, M. Time-Dependent Density Functional Theory Description of On-Site Electron Repulsion an Ligand Field Effects in the Optical Spectrum of Hexaaquoruthenium(II) in Solution. *J. Phys. Chem. B* **2005**, *109*, 12222–12226.
286. Neugebauer, J.; Gritsenko, O.; Baerends, E. J. Assessment of a Simple Correction for the Long-Range Charge-Transfer Problem in Time-Dependent Density Functional Theory. *J. Chem. Phys.* **2006**, *124*, 214102.
287. Lange, A.; Herbert, J. M. Simple Methods to Reduce Charge-Transfer Contamination in Time-Dependent Density-Functional Calculations of Clusters and Liquids. *J. Chem. Theory Comput.* **2007**, *3*, 1680–1690.
288. Isborn, C. M.; Mar, B. D.; Curchod, B. F. E.; Tavernelli, I.; Martínez, T. J. The Charge Transfer Problem in Density Functional Theory Calculations of Aqueously Solvated Molecules. *J. Phys. Chem. B* **2013**, *117*, 12189–12201.
289. Dreuw, A.; Head-Gordon, M. Failure of Time-Dependent Density Functional Theory for Long-Range Charge-Transfer Excited-States: The Zincbacteriochlorin-Bacteriochlorin and Bacteriochlorophyll-Spheroidene Complexes. *J. Am. Chem. Soc.* **2004**, *126*, 4007–4016.
290. Magyar, R. J.; Tretiak, S. Dependence of Spurious Charge-Transfer Excited States on Orbital Exchange in TDDFT: Large Molecules and Clusters. *J. Chem. Theory Comput.* **2007**, *3*, 976–987.
291. Maitra, N. T. Charge-Transfer in Time-Dependent Density Functional Theory. *J. Phys. Condens. Matt.* **2017**, *29*, 423001.
292. Igumenshchev, K. I.; Tretiak, S.; Chernyak, V. Y. Excitonic Effects in a Time-Dependent Density Functional Theory. *J. Chem. Phys.* **2007**, *127*, 114902.
293. Mewes, S. A.; Plasser, F.; Dreuw, A. Universal Exciton Size in Organic Polymers is Determined by Nonlocal Orbital Exchange in Time-Dependent Density Functional Theory. *J. Phys. Chem. Lett.* **2017**, *8*, 1205–1210.
294. Peach, M. J. G.; Benfield, P.; Helgaker, T.; Tozer, D. J. Excitation Energies in Density Functional Theory: An Evaluation and a Diagnostic Test. *J. Chem. Phys.* **2008**, *128*, 044118.
295. Guido, C. A.; Cortona, P.; Mennucci, B.; Adamo, C. On the Metric of Charge Transfer Molecular Excitations: A Simple Chemical Descriptor. *J. Chem. Theory Comput.* **2013**, *9*, 3118–3126.
296. Guido, C. A.; Cortona, P.; Adamo, C. Effective Electron Displacements: A Tool for Time-Dependent Density Functional Theory Computational Spectroscopy. *J. Chem. Phys.* **2014**, *140*, 104101.
297. Plötner, J.; Tozer, D. J.; Dreuw, A. Dependence of Excited State Potential Energy Surfaces on the Spatial Overlap of the Kohn-Sham Orbitals and the Amount of Nonlocal Hartree-Fock Exchange in Time-Dependent Density Functional Theory. *J. Chem. Theory Comput.* **2010**, *6*, 2315–2324.
298. Moore, B., II; Sun, H.; Govind, N.; Kowalski, K.; Autschbach, J. Charge-Transfer Versus Charge-Transfer-Like Excitations Revisited. *J. Chem. Theory Comput.* **2015**, *11*, 3305–3320.
299. Marshburn, R. D.; Ashley, D. C.; Curtin, G. M.; Sultana, N.; Liu, C.; Vinueza, N. R.; Ison, E. A.; Jakubikova, E. Are All Charge-Transfer Parameters Created Equally? A Study of Functional Dependence and Excited-State Charge-Transfer Quantification Across Two Dye Families. *Phys. Chem. Chem. Phys.* **2021**, *23*, 20583–20597.
300. Le Bahers, T.; Adamo, C.; Ciofini, I. A Qualitative Index of Spatial Extent in Charge-Transfer Excitations. *J. Chem. Theory Comput.* **2011**, *7*, 2498–2506.
301. Jacquemin, D.; Le Bahers, T.; Adamo, C.; Ciofini, I. What Is the "Best" Atomic Charge Model to Describe Through-Space Charge-Transfer Excitations? *Phys. Chem. Chem. Phys.* **2012**, *14*, 5383–5388.
302. Ehara, M.; Fukuda, R.; Adamo, C.; Ciofini, I. Chemically Intuitive Indices for Charge-Transfer Excitation Based on SAC-CI and TD-DFT Calculations. *J. Comput. Chem.* **2013**, *34*, 2498–2501.
303. Savarese, M.; Guido, C. A.; Brémond, E.; Ciofini, I.; Adamo, C. Metrics for Molecular Electronic Excitations: A Comparison Between Orbital- and Density-Based Descriptors. *J. Phys. Chem. A* **2017**, *121*, 7543–7549.
304. Campetella, M.; Maschietto, F.; Frisch, M. J.; Scalmani, G.; Ciofini, I.; Adamo, C. Charge Transfer Excitations in TDDFT: A Ghost-Hunter Index. *J. Comput. Chem.* **2017**, *38*, 2151–2156.
305. García, J. S.; Maschietto, F.; Campetella, M.; Ciofini, I. Using Density Based Indexes and Wave Function Methods for the Description of Excited States: Excited State Proton Transfer Reactions as a Test Case. *J. Phys. Chem. A* **2018**, *122*, 375–382.
306. Campetella, M.; Perfetto, A.; Ciofini, I. Quantifying Partial Hole-Particle Distance at the Excited State: A Revised Version of the $D_{CT}$ Index. *Chem. Phys. Lett.* **2019**, *714*, 81–86.
307. Plasser, F.; Thomitzni, B.; Bäppler, S. A.; Wenzel, J.; Rehn, D. R.; Wormit, M.; Dreuw, A. Statistical Analysis of Electronic Excitation Processes: Spatial Location, Compactness, Charge Transfer, and Electron-Hole Correlation. *J. Comput. Chem.* **2015**, *36*, 1609–1620.
308. Mewes, S. A.; Dreuw, A. Density-Based Descriptors and Exciton Analyses for Visualizing and Understanding the Electronic Structure of Excited States. *Phys. Chem. Chem. Phys.* **2019**, *21*, 2843–2856.
309. Mester, D.; Kállay, M. Charge-Transfer Excitations Within Density Functional Theory: How Accurate Are the Most Recommended Approaches? *J. Chem. Theory Comput.* **2022**, *18*, 1646–1662.

310. Casanova-Páez, M.; Goerigk, L. Global Double Hybrids to Not Work for Charge Transfer: A Comment on "Double Hybrids And Time-Dependent Density Functional Theory: An Implementation and Benchmark on Charge Transfer Excited States". *J. Comput. Chem.* **2021**, *42*, 528–533.
311. Casanova-Páez, M.; Dardis, M. B.; Goerigk, L. ωB2PLYP and ωB2GPPLYP: The First Two Double-Hybrid Density Functionals With Long-Range Correction Optimized for Excitation Energies. *J. Chem. Theory Comput.* **2019**, *15*, 4735–4744.
312. Stein, T.; Kronik, L.; Baer, R. Reliable Prediction of Charge Transfer Excitations in Molecular Complexes Using Time-Dependent Density Functional Theory. *J. Am. Chem. Soc.* **2009**, *131*, 2818–2820.
313. Stein, T.; Kronik, L.; Baer, R. Prediction of Charge-Transfer Excitations in Coumarin-Based Dyes Using a Range-Separated Functional Tuned From First Principles. *J. Chem. Phys.* **2009**, *131*, 244119.
314. Baer, R.; Livshits, E.; Salzner, U. Tuned Range-Separated Hybrids in Density Functional Theory. *Annu. Rev. Phys. Chem.* **2010**, *61*, 85–109.
315. Kümmel, S. Charge-Transfer Excitations: A Challenge for Time-Dependent Density Functional Theory That Has Been Met. *Adv. Energy Mater.* **2017**, *7*, 1700440.
316. Perdew, J. P.; Parr, R. G.; Levy, M.; Balduz, J. L., Jr. Density-Functional Theory for Fractional Particle Number: Derivative Discontinuities of the Energy. *Phys. Rev. Lett.* **1982**, *49*, 1691–1694.
317. Zhang, Y.; Yang, W. Perspective on "Density-Functional Theory for Fractional Particle Number: Derivative Discontinuities of the Energy". *Theor. Chem. Acc.* **2000**, *103*, 346–348.
318. Refaely-Abramson, S.; Baer, R.; Kronik, L. Fundamental and Excitation Gaps in Molecules of Relevance for Organic Photovoltaics From an Optimally Tuned Range-Separated Hybrid Functional. *Phys. Rev. B* **2011**, *84*, 075144.
319. Kronik, L.; Stein, T.; Refaely-Abramson, S.; Baer, R. Excitation Gaps of Finite-Sized Systems From Optimally-Tuned Range-Separated Hybrid Functionals. *J. Chem. Theory Comput.* **2012**, *8*, 1515–1531.
320. Körzdörfer, T.; Sears, J. S.; Sutton, C.; Brédas, J. L. Long-Range Corrected Hybrid Functionals for $\pi$-Conjugated Systems: Dependence of the Range-Separation Parameter on Conjugation Length. *J. Chem. Phys.* **2011**, *135*, 204107.
321. Körzdörfer, T.; Brédas, J. L. Organic Electronic Materials: Recent Advances in the DFT Description of the Ground and Excited States Using Tuned Range-Separated Hybrid Functionals. *Acc. Chem. Res.* **2014**, *47*, 3284–3291.
322. Uhlig, F.; Herbert, J. M.; Coons, M. P.; Jungwirth, P. Optical Spectroscopy of the Bulk and Interfacial Hydrated Electron From Ab Initio Calculations. *J. Phys. Chem. A* **2014**, *118*, 7507–7515.
323. Gray, M.; Herbert, J. M. Simplified Tuning of Long-Range Corrected Density Functionals for Symmetry-Adapted Perturbation Theory. *J. Chem. Phys.* **2021**, *155*, 034103.
324. Modrzejewski, M.; Rajchel, Ł.; Chalasinski, G.; Szczesniak, M. M. Density-Dependent Onset of the Long-Range Exchange: A Key to Donor-Acceptor Properties. *J. Phys. Chem. A* **2013**, *117*, 11580–11586.
325. Lao, K. U.; Herbert, J. M. Atomic Orbital Implementation of Extended Symmetry-Adapted Perturbation Theory (XSAPT) and Benchmark Calculations for Large Supramolecular Complexes. *J. Chem. Theory Comput.* **2018**, *14*, 2955–2978.
326. Levine, B. G.; Ko, C.; Quenneville, J.; Martínez, T. J. Conical Intersections and Double Excitations in Time-Dependent Density Functional Theory. *Mol. Phys.* **2006**, *104*, 1039–1051.
327. Yue, L.; Liu, Y.; Zhu, C. Performance of TDDFT With and Without Spin-Flip in Trajectory Surface Hopping Dynamics: *Cis-Trans* Azobenzene Photoisomerization. *Phys. Chem. Chem. Phys.* **2018**, *20*, 24123–24139.
328. Shao, Y.; Head-Gordon, M.; Krylov, A. I. The Spin-Flip Approach Within Time-Dependent Density Functional Theory: Theory and Applications to Diradicals. *J. Chem. Phys.* **2003**, *118*, 4807–4818.
329. Huix-Rotllant, M.; Natarajan, B.; Ipatov, A.; Wawire, C. M.; Deutsch, T.; Casida, M. E. Assessment of Noncollinear Spin-Flip Tamm-Dancoff Approximation Time-Dependent Density-Functional Theory for the Photochemical Ring-Opening of Oxirane. *Phys. Chem. Chem. Phys.* **2010**, *12*, 12811–12825.
330. Zhang, X.; Herbert, J. M. Spin-Flip, Tensor Equation-of-Motion Configuration Interaction With a Density-Functional Correction: A Spin-Complete Method for Exploring Excited-State Potential Energy Surfaces. *J. Chem. Phys.* **2015**, *143*, 234107.
331. Harabuchi, Y.; Keipert, K.; Zahariev, F.; Taketsugu, T.; Gordon, M. S. Dynamics Simulations With Spin-Flip Time-Dependent Density Functional Theory: Photoisomerization and Photocyclization Mechanisms of *Cis*-Stilbene in $\pi\pi^*$ States. *J. Phys. Chem. A* **2014**, *118*, 11987–11998.
332. Lee, S.; Filatov, M.; Lee, S.; Choi, C. H. Eliminating Spin-Contamination of Spin-Flip Time Dependent Density Functional Theory Within Linear Response Formalism by the Use of Zeroth-Order Mixed-Reference (MR) Reduced Density Matrix. *J. Chem. Phys.* **2018**, *149*, 104101.
333. Lee, S.; Shostak, S.; Filatov, M.; Choi, C. H. Conical Intersections in Organic Molecules: Benchmarking Mixed-Reference Spin-Flip Time-Dependent DFT (MSRF-TD-DFT) vs Spin-Flip TD-DFT. *J. Phys. Chem. A* **2019**, *123*, 6455–6462.
334. Horbatenko, Y.; Lee, S.; Filatov, M.; Choi, C. H. Performance Analysis and Optimization of Mixed-Reference Spin-Flip Time-Dependent Density Functional Theory (MRSF-TDDFT) for Vertical Excitation Energies and Singlet-Triplet Energy Gaps. *J. Phys. Chem. A* **2019**, *123*, 7991–8000.
335. Lee, S.; Kim, E. E.; Nakata, H.; Lee, S.; Choi, C. H. Efficient Implementations of Analytic Energy Gradient for Mixed-Reference Spin-Flip Time-Dependent Density Functional Theory (MRSF-TDDFT). *J. Chem. Phys.* **2019**, *150*, 184111.
336. Lee, S.; Horbatenko, Y.; Filatov, M.; Choi, C. H. Fast and Accurate Computation of Nonadiabatic Coupling Matrix Elements Using the Truncated Leibniz Formula and Mixed-Reference Spin-Flip Time-Dependent Density Functional Theory. *J. Phys. Chem. Lett.* **2021**, *12*, 4722–4728.
337. Horbatenko, Y.; Sadiq, S.; Lee, S.; Filatov, M.; Choi, C. H. Mixed-Reference Spin-Flip Time-Dependent Density Functional Theory (MRSF-TDDFT) as a Simple Yet Accurate Method for Diradicals and Diradicaloids. *J. Chem. Theory Comput.* **2021**, *17*, 848–859.
338. Tretiak, S.; Igumenshchev, K.; Chernyak, V. Exciton Sizes of Conducting Polymers Predicted by Time-Dependent Density Functional Theory. *Phys. Rev. B* **2005**, *71*, 033201.

339. Hait, D.; Head-Gordon, M. Orbital Optimized Density Functional Theory for Electronic Excited States. *J. Phys. Chem. Lett.* **2021**, *12*, 4517–4529.
340. Vandaele, E.; Mališ, M.; Luber, S. The ΔSCF Method for Non-Adiabatic Dynamics of Systems in the Liquid Phase. *J. Chem. Phys.* **2022**, *156*, 130901.
341. Hanson-Heine, M. W. D.; George, M. W.; Besley, N. A. Calculating Excited State Properties Using Kohn-Sham Density Functional Theory. *J. Chem. Phys.* **2013**, *138*, 064101.
342. Morrison, R. C. Electron Correlation and Noninteracting *v*-Representability in Density Functional Theory: The Be Isoelectronic Series. *J. Chem. Phys.* **2002**, *117*, 10506–10511.
343. Gilbert, A. T. B.; Besley, N. A.; Gill, P. M. W. Self-Consistent Field Calculations of Excited States Using the Maximum Overlap Method (MOM). *J. Phys. Chem. A* **2008**, *112*, 13164–13171.
344. Besley, N. A.; Gilbert, A. T. B.; Gill, P. M. W. Self-Consistent-Field Calculations of Core Excited States. *J. Chem. Phys.* **2009**, *130*, 124308.
345. Barca, G. M. J.; Gilbert, A. T. B.; Gill, P. M. W. Simple Models for Difficult Electronic Excitations. *J. Chem. Theory Comput.* **2018**, *14*, 1501–1509.
346. Corzo, H. H.; Taka, A. A.; Pribam-Jones, A.; Hratchian, H. P. Using Projection Operators With Maximum Overlap Methods to Simplify Challenging Self-Consistent Field Optimization. *J. Comput. Chem.* **2022**, *43*, 382–390.
347. Ye, H. Z.; Welborn, M.; Ricke, N. D.; Van Voorhis, T. *σ*-SCF: A Direct Energy-Targeting Method to Mean-Field Excited States. *J. Chem. Phys.* **2017**, *147*, 214104.
348. Hait, D.; Head-Gordon, M. Excited State Orbital Optimization Via Minimizing the Square of the Gradient: General Approach and Application to Singly and Doubly Excited States Via Density Functional Theory. *J. Chem. Theory Comput.* **2020**, *16*, 1699–1710.
349. Carter-Fenk, K.; Herbert, J. M. State-Targeted Energy Projection: A Simple and Robust Approach to Orbital Relaxation of Non-Aufbau Self-Consistent Field Solutions. *J. Chem. Theory Comput.* **2020**, *16*, 5067–5082.
350. Jacobson, L. D.; Herbert, J. M. A Simple Algorithm for Determining Orthogonal, Self-Consistent Excited-State Wave Functions for a State-Specific Hamiltonian: Application to the Optical Spectrum of the Aqueous Electron. *J. Chem. Theory Comput.* **2011**, *7*, 2085–2093.
351. Barca, G. M. J.; Gilbert, A. T. B.; Gill, P. M. W. Excitation Number: Characterizing Multiply Excited States. *J. Chem. Theory Comput.* **2018**, *14*, 9–13.
352. Kitagawa, Y.; Saito, T.; Ito, M.; Shoji, M.; Koizumi, K.; Yamanaka, S.; Kawakami, T.; Okumura, M.; Yamaguchi, K. Approximately Spin-Projected Geometry Optimization Method and Its Application to Di-Chromium Systems. *Chem. Phys. Lett.* **2007**, *442*, 445–450.
353. Thompson, L. M.; Hratchian, H. P. On Approximate Projection Models. *Mol. Phys.* **2019**, *117*, 1421–1429.
354. Kitagawa, Y.; Saito, T.; Yamaguchi, K. Approximate Spin Projection for Broken-Symmetry Method and Its Application. In *Symmetry (Group Theory) and Mathematical Treatment in Chemistry*; Akitsu, T., Ed.; IntechOpen, 2018; pp. 121–139. Chapter 7.
355. Nair, N. N.; Schreiner, E.; Pollet, R.; Staemmler, V.; Marx, D. Magnetostructural Dynamics With the Extended Broken Symmetry Formalism: Antiferromagnetic [2Fe-2S] Complexes. *J. Chem. Theory Comput.* **2008**, *4*, 1174–1188.
356. Daul, C. Density Functional Theory Applied to the Excited States of Coordination Compounds. *Int. J. Quantum Chem.* **1994**, *52*, 867–877.
357. Ziegler, T.; Rauk, A.; Baerends, E. J. On the Calculation of Multiplet Energies by the Hartree-Fock-Slater Method. *Theor. Chem. Acc.* **1977**, *43*, 261–271.
358. Frank, I.; Hutter, J.; Marx, D.; Parrinello, M. Molecular Dynamics in Low-Spin Excited States. *J. Chem. Phys.* **1998**, *108*, 4060–4069.
359. Filatov, M.; Shaik, S. A Spin-Restricted Ensemble-References Kohn-Sham Method and Its Application to Diradicaloid Situations. *Chem. Phys. Lett.* **1999**, *304*, 429–437.
360. Kowalczyk, T.; Tsuchimochi, T.; Chen, P. T.; Top, L.; Van Voorhis, T. Excitation Energies and Stokes Shifts From a Restricted Open-Shell Kohn-Sham Approach. *J. Chem. Phys.* **2013**, *138*, 164101.
361. Kowalczyk, T.; Yost, S. R.; Van Voorhis, T. Assessment of the ΔSCF Density Functional Theory Approach for Electronic Excitations in Organic Dyes. *J. Chem. Phys.* **2011**, *134*, 054128.
362. Besley, N. A. Theoretical Study of Electronically Excited States. In *International Conference of Computational Methods in Sciences and Engineering 2014 (ICCMSE 2014)*; Simos, T. E., Kalogiratou, Z., Monovasilis, T., Eds.; AIP Conference Proceedings, Vol. 1618; American Institute of Physics, 2014; pp. 576–584.
363. Briggs, E. A.; Besley, N. A.; Robinson, D. QM/MM Excited State Molecular Dynamics and Fluorescence Spectroscopy of BODIPY. *J. Phys. Chem. A* **2013**, *117*, 2644–2650.
364. Briggs, E. A.; Besley, N. A. Density Functional Theory Based Analysis of Photoinduced Electron Transfer in a Triazacryptand Based $K^+$ Sensor. *J. Phys. Chem. A* **2015**, *119*, 2902–2907.
365. Hanson-Heine, M. W. D.; Wriglesworth, A.; Uroos, M.; Calladine, J. A.; Murphy, T. S.; Hamilton, M.; Clark, I. P.; Towrie, M.; Dowden, J.; Besley, N. A.; George, M. W. Calculating Singlet Excited States: Comparison With Fast Time-Resolved Infrared Spectroscopy of Coumarins. *J. Chem. Phys.* **2015**, *142*, 154119.
366. Jiao, L.; Yu, C.; Wang, J.; Briggs, E. A.; Besley, N. A.; Robinson, D.; Ruedas-Rama, M. J.; Orte, A.; Crovetto, L.; Talavera, E. M.; Alvarez-Pez, J. M.; Van der Auweraer, M.; Boens, N. Unusual Spectroscopic and Photophysical Properties of *Meso-Tert*-ButylBODIPY in Comparison to Related Alkylated BODIPY Dyes. *RSC Adv.* **2015**, *5*, 89375–89388.
367. Kowalczyk, T.; Le, K.; Irle, S. Self-Consistent Optimization of Excited States Within Density-Functional Tight-Binding. *J. Chem. Theory Comput.* **2016**, *12*, 313–323.
368. Angelani, L.; Di Leonardo, R.; Ruocco, G.; Scala, A.; Sciortino, F. Saddles in the Energy Landscape Probed by Supercooled Liquids. *Phys. Rev. Lett.* **2000**, *85*, 5356–5359.
369. Angelani, L.; Di Leonardo, R.; Ruocco, G.; Scala, A.; Sciortino, F. Quasisaddles as Relevant Points of the Potential Energy Surface in Dynamics of Supercooled Liquids. *J. Chem. Phys.* **2002**, *116*, 10297–10306.

370. Doye, J. P. K.; Wales, D. J. Saddle Points and Dynamics of Lennard-Jones Clusters, Solids, and Supercooled Liquids. *J. Chem. Phys.* **2002**, *116*, 3777–3788.
371. Doye, J. P. K.; Wales, D. J. Comment on "Quasisaddles as Relevant Points of the Potential Energy Surface in the Dynamics of Supercooled Liquids". *J. Chem. Phys.* **2003**, *118*, 5263–5264.
372. Slater, J. C.; Wood, J. H. Statistical Exchange and the Total Energy of a Crystal. *Int. J. Quantum Chem.* **1971**, *5*, 3–34.
373. Slater, J. C. Statistical Exchange-Correlation in the Self-Consistent Field. *Adv. Quantum Chem.* **1972**, *6*, 1–92.
374. Cavalleri, M.; Odelius, M.; Nordlund, D.; Nilsson, A.; Pettersson, L. G. M. Half or Full Core Hole in Density Functional Theory X-Ray Absorption Spectrum Calculations of Water? *Phys. Chem. Chem. Phys.* **2005**, *7*, 2854–2858.
375. Leetmaa, M.; Ljungberg, M. P.; Lyubartsev, A.; Nilsson, A.; Pettersson, L. G. M. Theoretical Approximations to X-Ray Absorption Spectroscopy of Liquid Water and Ice. *J. Electron Spectrosc.* **2010**, *177*, 135–157.
376. Fransson, T.; Zhotobriukh, I.; Coriani, S.; Wikfeldt, K. T.; Norman, P.; Pettersson, L. G. M. Requirements of First-Principles Calculations of X-Ray Absorption Spectra of Liquid Water. *Phys. Chem. Chem. Phys.* **2016**, *18*, 566–583.
377. Zhang, Y.; Hua, W.; Bennett, K.; Mukamel, S. Nonlinear Spectroscopy of Core and Valence Excitations Using Short X-Ray Pulses: Simulation Challenges. In *Density-Functional Methods for Excited States*; Ferré, N., Filatov, M., Huix-Rotllant, M., Eds.; Topics in Current Chemistry, Vol. 368; Springer International Publishing: Cham, 2016; pp. 273–346.
378. Michelitsch, G. S.; Reuter, K. Efficient Simulation of Near-Edge X-Ray Absorption Fine Structure (NEXAFS) in Density-Functional Theory: Comparison of Core-Level Constraining Approaches. *J. Chem. Phys.* **2019**, *150*, 074104.
379. Jana, S; Herbert, J. M. Slater transition methods for core-level electron binding energies. *J. Chem. Phys.* **2023**, *158*, 094111.
380. Jana, S; Herbert, J. M. Fractional-electron and transition-potential methods for core-to-valence excitation energies using density functional theory. *ChemRxiv* **2023**,. https://doi.org/10.26434/chemrxiv-2023-2v4cx-v2.
381. Janak, J. F. Proof That $\partial E/\partial n_i = \epsilon_i$ in Density-Functional Theory. *Phys. Rev. B* **1978**, *18*, 7165–7168.
382. Stener, M.; Lisini, A.; Decleva, P. Density Functional Calculations of Excitation Energies and Oscillator Strengths for C1s $\rightarrow \pi^*$ and O1s $\rightarrow \pi^*$ Excitations and Ionization Potentials in Carbonyl Containing Molecules. *Chem. Phys.* **1995**, *191*, 141–154.
383. Hu, C. H.; Chong, D. P. Density Functional Computations for Inner-Shell Excitation Spectroscopy. *Chem. Phys. Lett.* **1996**, *262*, 729–732.
384. Triguero, L.; Pettersson, L. G. M.; Ågren, H. Calculations of Near-Edge X-Ray-Absorption Spectra of Gas-Phase and Chemisorbed Molecules by Means of Density-Functional and Transition-Potential Theory. *Phys. Rev. B* **1998**, *58*, 8097–8110.
385. Triguero, L.; Pettersson, L. G. M.; Ågren, H. Calculations of X-Ray Emission Spectra of Molecules and Surface Adsorbates by Means of Density Functional Theory. *J. Phys. Chem. A* **1998**, *102*, 10599–10607.
386. Williams, A. R.; deGroot, R. A.; Sommers, C. B. Generalization of Slater's Transition State Concept. *J. Chem. Phys.* **1975**, *63*, 628–631.
387. Chong, D. P. Accurate Calculation of Core-Electron Binding Energies by the Density-Functional Method. *Chem. Phys. Lett.* **1995**, *232*, 486–490.
388. Hirao, K.; Nakajima, T.; Chan, B. An Improved Slater's Transition State Approximation. *J. Chem. Phys.* **2021**, *155*, 034101.
389. Hirao, K.; Chan, B.; Song, J. W.; Bhattarai, K.; Tewary, S. Excitation Energies Expressed as Orbital Energies of Kohn-Sham Density Functional Theory With Long-Range Corrected Functionals. *J. Comput. Chem.* **2020**, *41*, 1368–1383.
390. Chan, B.; Dawson, W.; Nakajima, T.; Hirao, K. Taking Advantage of a Systematic Energy Non-Linearity Error in Density Functional Theory for the Calculation of Electronic Energy Levels. *J. Phys. Chem. A* **2022**, *125*, 10507–10513.
391. Prendergast, D.; Galli, G. X-Ray Absorption Spectra of Water From First Principles Calculations. *Phys. Rev. Lett.* **2006**, *96*, 215502.
392. Liang, Y.; Vinson, J.; Pemmaraju, S.; Drisdell, W. S.; Shirley, E. L.; Prendergast, D. Accurate X-Ray Spectral Predictions: An Advanced Self-Consistent-Field Approach Inspired by Many-Body Perturbation Theory. *Phys. Rev. Lett.* **2017**, *118*, 096402.
393. Liang, Y.; Prendergast, D. Taming Convergence in the Determinant Approach for X-Ray Excitation Spectra. *Phys. Rev. B* **2019**, *100*, 075121.
394. Liu, J.; Zhang, Y.; Bao, P.; Yi, Y. Evaluating Electronic Couplings for Excited State Charge Transfer Based on Maximum Occupation Method ΔSCF Quasi-Adiabatic States. *J. Chem. Theory Comput.* **2017**, *13*, 843–851.
395. Subotnik, J. E. Configuration Interaction Singles Has a Large Systematic Bias Against Charge-Transfer States. *J. Chem. Phys.* **2011**, *135*, 071104.
396. Kumar, C.; Luber, S. Robust ΔSCF Calculations With Direct Functional Minimization Methods and STEP for Molecules and Materials. *J. Chem. Phys.* **2022**, *156*, 154104.
397. Balevičius, V., Jr.; Abramavicius, D.; Polívka, T.; Pour, A. G.; Hauer, J. A Unified Picture of S* in Carotenoids. *J. Phys. Chem. Lett.* **2016**, *7*, 3347–3352.
398. Llansola-Portoles, M. J.; Pascal, A. A.; Robert, B. Electronic and Vibrational Properties of Carotenoids: From *in vitro* to *in vivo*. *J. R. Soc. Interface* **2017**, *14*, 20170504.
399. Hashimoto, H.; Uragami, C.; Yukihira, N.; Gardiner, A. T.; Cogdell, R. J. Understanding/Unravelling Carotenoid Excited Singlet States. *J. R. Soc. Interface* **2018**, *15*, 20180026.
400. Serrano-Andrés, L.; Merchán, M.; Nebot-Gil, I.; Lindh, R.; Roos, B. O. Towards an Accurate Molecular Orbital Theory for Excited States: Ethene, Butadiene, and Hexatriene. *J. Chem. Phys.* **1993**, *98*, 3151–3162.
401. Nakayama, K.; Nakano, H.; Hirao, K. Theoretical Study of the $\pi \rightarrow \pi^*$ Excited States of Linear Polyenes: The Energy Gap Between $1^1B_u^+$ and $2^1A_g^-$ States and Their Character. *Int. J. Quantum Chem.* **1998**, *66*, 157–175.
402. Cave, R. J.; Zhang, F.; Maitra, N. T.; Burke, K. A Dressed TDDFT Treatment of the $2\,^1A_g$ States of Butadiene and Hexatriene. *Chem. Phys. Lett.* **2004**, *389*, 39–42.
403. Starcke, J. H.; Wormit, M.; Schirmer, J.; Dreuw, A. How Much Double Excitation Character Do the Lowest Excited States of Linear Polyenes have? *Chem. Phys.* **2006**, *329*, 39–49.
404. Watson, M. A.; Chan, G. K. L. Excited States of Butadiene to Chemical Accuracy: Reconciling Theory and Experiment. *J. Chem. Theory Comput.* **2012**, *8*, 4013–4018.

405. Loos, P. F.; Boggio-Pasqua, M.; Scemama, A.; Caffarel, M.; Jacquemin, D. Reference Energies for Double Excitations. *J. Chem. Theory Comput.* **2019**, *15*, 1939–1956.
406. Koch, H.; Christiansen, O.; Jørgensen, P.; Sanchez de Merás, A. M.; Helgaker, T. The CC3 Model: An Iterative Coupled Cluster Approach Including Connected Triples. *J. Chem. Phys.* **1997**, *106*, 1808–1818.
407. Paul, A. C.; Myhre, R. H.; Koch, H. New and Efficient Implementataion of CC3. *J. Chem. Theory Comput.* **2021**, *17*, 117–126.
408. Stockett, M. H.; Musbat, L.; Kjær, C.; Houmøller, J.; Toker, Y.; Rubio, A.; Milne, B. F.; Nielsen, S. B. The Soret Absorption Band of Isolated Chlorophyll *a* and *b* Tagged With Quaternary Ammonium Ions. *Phys. Chem. Chem. Phys.* **2015**, *17*, 25793–25798.
409. Milne, B. F.; Toker, Y.; Rubio, A.; Nielsen, S. B. Unraveling the Intrinsic Color of Chlorophyll. *Angew. Chem. Int. Ed. Engl.* **2015**, *54*, 2170–2173.
410. Gouterman, M.; Wagnière, G. H.; Snyder, L. C. Spectra of Porphyrins: Part II. Four Orbital Model. *J. Mol. Spectrosc.* **1963**, *11*, 108–127.
411. Hait, D.; Head-Gordon, M. Highly Accurate Prediction of Core Spectra of Molecules at Density Functional Theory Cost: Attaining Sub-Electronvolt Error From a Restricted Open-Shell Kohn-Sham Approach. *J. Phys. Chem. Lett.* **2020**, *11*, 775–786.
412. Gupta, R. P.; Sen, S. K. Calculation of Multiplet Structure of Core *p*-Vacancy Levels. II. *Phys. Rev. B* **1975**, *12*, 15–19.
413. Yamashita, T.; Hayes, P. Analysis of XPS Spectra of $Fe^{2+}$ and $Fe^{3+}$ Ions in Oxide Materials. *Appl. Surf. Sci.* **2008**, *254*, 2441–2449.
414. Cunha, L. A.; Hait, D.; Kang, R.; Mao, Y.; Head-Gordon, M. Relativistic Orbital-Optimized Density Functional Theory for Accurate Core-Level Spectroscopy. *J. Phys. Chem. Lett.* **2022**, *13*, 3438–3449.
415. Imamura, Y.; Nakai, H. Analysis of Self-Interaction Correction for Describing Core Excited States. *Int. J. Quantum Chem.* **2007**, *107*, 23–29.
416. Imamura, Y.; Nakai, H. Description of Core-Ionized and Core-Excited States by Density Functional Theory and Time-Dependent Density Functional Theory. In *Quantum Systems in Chemistry and Physics*; Nishikawa, K., Maruani, J., Brändas, E. J., Delgado-Barrio, G., Piecuch, P., Eds.; Progress in Theoretical Chemistry and Physics, Vol. 26; Spring Science+Business Media: Dordrecht, 2012; pp. 275–308. Chapter 14.
417. Jorstad, J. V.; Xie, T.; Morales, C. M. Δ-SCF Calculations of Core Electron Binding Energies in First-Row Transition Metal Atoms. *Int. J. Quantum Chem.* **2022**, *122*, e26881.
418. Kahk, J. M.; Lischner, J. Predicting Core Electron Binding Energies in Elements of the First Transition Series Using the Δ-Self-Consistent-Field Method. *Faraday Discuss.* **2022**, *236*, 364–373.
419. Bellafont, N. P.; Bagus, P. S.; Illas, F. Prediction of Core Level Binding Energies in Density Functional Theory: Rigorous Definition of Initial and Final State Contributions and Implications on the Physical Meaning of Kohn-Sham Energies. *J. Chem. Phys.* **2015**, *142*, 214102.
420. Kubas, A.; Verkamp, M.; Vura-Weis, J.; Neese, F.; Maganas, D. Restricted Open-Shell Configuration Interaction Singles Study on M- and L-Edge X-Ray Absorption Spectroscopy of Solid Chemical Systems. *J. Chem. Theory Comput.* **2018**, *14*, 4320–4334.
421. Bellafont, N. P.; Saiz, G. A.; Viñes, F.; Illas, F. Performance of Minnesota Functionals on Predicting Core-Level Binding Energies of Molecules Containing Main-Group Elements. *Theor. Chem. Acc.* **2016**, *135*, 35.
422. Roemelt, M.; Beckwith, M. A.; Duboc, C.; Collomb, M. N.; Neese, F.; DeBeer, S. Manganese K-Edge X-Ray Absorption Spectroscopy as a Probe of Metal-Ligand Interactions in Coordination Compounds. *Inorg. Chem.* **2012**, *51*, 680–687.
423. Chantzis, A.; Kowalska, J. K.; Maganas, D.; DeBeer, S.; Neese, F. Ab Initio Wave Function-Based Determination of Element Specific Shifts for the Efficient Calculation of X-Ray Absorption Spectra of Main Group Elements and First Row Transition Metals. *J. Chem. Theory Comput.* **2018**, *14*, 3686–3702.
424. do Couto, P. C.; Hollas, D.; Slavíček, P. On the Performance of Optimally Tuned Range-Separated Hybrid Functionals for X-Ray Absorption Modeling. *J. Chem. Theory Comput.* **2015**, *11*, 3234–3244.
425. Fransson, T.; Brumboiu, I. E.; Vidal, M. L.; Norman, P.; Coriani, S.; Dreuw, A. XABOOM: An X-Ray Absorption Benchmark of Organic Molecules Based on Carbon, Nitrogen, and Oxygen 1s $\rightarrow \pi^*$ Transitions. *J. Chem. Theory Comput.* **2021**, *17*, 1618–1637.
426. Capano, G.; Penfold, T. J.; Besley, N. A.; Milne, C. J.; Reinhard, M.; Rittmann-Frank, H.; Glatzel, P.; Abela, R.; Rothlisberger, U.; Chergui, M.; Tavernelli, I. The Role of Hartree-Fock Exchange in the Simulation of X-Ray Absorption Spectra: A Study of Photoexcited $[Fe(bpy)_3]^{2+}$. *Chem. Phys. Lett.* **2013**, *580*, 179–184.
427. Carter-Fenk, K.; Mundy, C. J.; Herbert, J. M. Natural Charge-Transfer Analysis: Eliminating Spurious Charge-Transfer States in Time-Dependent Density Functional Theory Via Diabatization, With Application to Projection-Based Embedding. *J. Chem. Theory Comput.* **2021**, *17*, 4195–4210.
428. Casas, F.; Iserles, A. Explicit Magnus Expansions for Nonlinear Equations. *J. Phys. A: Math. Gen.* **2006**, *39*, 5445.
429. Blanes, S.; Casas, F.; Oteo, J. A.; Ros, J. The Magnus Expansion and Some of Its Applications. *Phys. Rep.* **2009**, *470*, 151–238.
430. Zhu, Y.; Herbert, J. M. Self-Consistent Predictor/Corrector Algorithms for Stable and Efficient Integration of the Time-Dependent Kohn-Sham Equation. *J. Chem. Phys.* **2018**, *148*, 044117.
431. Castro, A.; Marques, M. A. L.; Rubio, A. Propagators for the Time-Dependent Kohn-Sham Equations. *J. Chem. Phys.* **2004**, *121*, 3425–3433.
432. Li, X.; Smith, S. M.; Markevitch, A. N.; Romanov, D. A.; Levis, R. J.; Schlegel, H. B. A Time-Dependent Hartree-Fock Approach for Studying the Electronic Optical Response of Molecules in Intense Fields. *Phys. Chem. Chem. Phys.* **2005**, *7*, 233–239.
433. Williams-Young, D.; Goings, J. J.; Li, X. Accelerating Real-Time Time-Dependent Density Functional Theory With a Nonrecursive Chebyshev Expansion of the Quantum Propagator. *J. Chem. Theory Comput.* **2016**, *12*, 5333–5338.
434. Pueyo, A. G.; Marques, M. A. L.; Rubio, A.; Castro, A. Propagators for the Time-Dependent Kohn-Sham Equations: Multistep, Runge-Kutta, Exponential Runge-Kutta, and Commutator Free Magnus Method. *J. Chem. Theory Comput.* **2018**, *14*, 3040–3052.
435. Ye, L.; Wang, H.; Zhang, Y.; Liu, W. Self-Adaptive Real-Time Time-Dependent Density Functional Theory for Core Excitations. *J. Chem. Phys.* **2022**, *157*, 074106.
436. Yabana, K.; Sugiyama, T.; Shinohara, Y.; Otobe, T.; Bertsch, G. F. Time-Dependent Density Functional Theory for Strong Electromagnetic Fields in Crystalline Solids. *Phys. Rev. B* **2012**, *85*, 045134.

437. Fuks, J. I.; Elliott, P.; Rubio, A.; Maitra, N. T. Dynamics of Charge-Transfer Processes With Time-Dependent Density Functional Theory. *J. Phys. Chem. Lett.* **2013**, *4*, 735–739.
438. Luo, K.; Fuks, J. I.; Maitra, N. T. Studies of Spuriously Shifting Resonances in Time-Dependent Density Functional Theory. *J. Chem. Phys.* **2016**, *145*, 044101.
439. Fischer, S. A.; Cramer, C. J.; Govind, N. Excited State Absorption From Real-Time Time-Dependent Density Functional Theory. *J. Chem. Theory Comput.* **2015**, *11*, 4294–4303.
440. Klinkusch, S.; Saalfrank, P.; Klamroth, T. Laser-Induced Electron Dynamics Including Photoionization: A Heuristic Model Within Time-Dependent Configuration Interaction Theory. *J. Chem. Phys.* **2009**, *131*, 114304.
441. Karamatskou, A.; Pabst, S.; Chen, Y. J.; Santra, R. Calculation of Photoelectron Spectra Within the Time-Dependent Configuration-Interaction Singles Scheme. *Phys. Rev. A* **2014**, *89*, 033415.
442. Krause, P.; Schlegel, H. B. Strong Field Ionization Rates of Linear Polyenes Simulated With Time-Dependent Configuration Interaction and an Absorbing Potential. *J. Chem. Phys.* **2014**, *141*, 174104.
443. Krause, P.; Sonk, J. A.; Schlegel, H. B. Strong Field Ionization Rates Simulated With Time-Dependent Configuration Interaction and an Absorbing Potential. *J. Chem. Phys.* **2014**, *140*, 174113.
444. Krause, P.; Schlegel, H. B. Angle-Dependent Ionization of Small Molecules by Time-Dependent Configuration Interaction and an Absorbing Potential. *J. Phys. Chem. Lett.* **2015**, *6*, 2140–2146.
445. Krause, P.; Schlegel, H. B. Angle-Dependent Ionization of Hydrides $AH_n$ Calculated by Time-Dependent Configuration Interaction With an Absorbing Potential. *J. Phys. Chem. A* **2015**, *119*, 10212–10220.
446. Hoerner, P.; Schlegel, H. B. Angular Dependence of Strong Field Ionization of $CH_3X$ (X = F, Cl, Br, or I) Using Time-Dependent Configuration Interaction With an Absorbing Potential. *J. Phys. Chem. A* **2017**, *121*, 5940–5946.
447. Hoerner, P.; Schlegel, H. B. Angular Dependence of Ionization by Circularly Polarized Light Calculated With Time-Dependent Configuration Interaction With an Absorbing Potential. *J. Phys. Chem. A* **2017**, *121*, 1336–1343.
448. Hoerner, P.; Schlegel, H. B. Angular Dependence of Strong Field Ionization of Haloacetylenes HCCX (X = F, Cl, Br, I) Using Time-Dependent Configuration Interaction With an Absorbing Potential. *J. Phys. Chem. C* **2018**, *122*, 13751–13757.
449. Hoerner, P.; Li, W.; Schlegel, H. B. Angular Dependence of Strong Field Ionization of 2-Phenylethyl-*n*,*n*-Dimethylamine (PENNA) Using Time-Dependent Configuration Interaction With an Absorbing Potential. *J. Phys. Chem. A* **2020**, *124*, 4777–4781.
450. Lee, M. K.; Hoerner, P.; Li, W.; Schlegel, H. B. Effect of Spin-Orbit Coupling on Strong Field Ionization Simulated With Time-Dependent Configuration Interaction. *J. Chem. Phys.* **2020**, *153*, 244109.
451. Hoerner, P.; Li, W.; Schlegel, H. B. Sequential Double Ionization of Molecules by Strong Laser Fields Simulated With Time-Dependent Configuration Interaction. *J. Chem. Phys.* **2021**, *155*, 114103.
452. Luppi, E.; Head-Gordon, M. The Role of Rydberg and Continuum Levels in Computing High Harmonic Generation Spectra of the Hydrogen Atom Using Time-Dependent Configuration Interaction. *J. Chem. Phys.* **2013**, *139*, 164121.
453. White, A. F.; Heide, C. J.; Saalfrank, P.; Head-Gordon, M.; Luppi, E. Computation of High-Harmonic Generation Spectra of the Hydrogen Molecule Using Time-Dependent Configuration-Interaction. *Mol. Phys.* **2016**, *114*, 947–956.
454. Coccia, E.; Mussard, B.; Labeye, M.; Caillat, J.; Taïeb, R.; Toulouse, J.; Luppi, E. Gaussian Continuum Basis Functions for Calculating High-Harmonic Generation Spectra. *Int. J. Quantum Chem.* **2016**, *116*, 1120–1131.
455. Labeye, M.; Zapata, F.; Coccia, E.; Véniard, V.; Toulouse, J.; Caillat, J.; Taïeb, R.; Luppi, E. Optimal Basis Set for Electron Dynamics in Strong Laser Fields: The Case of Molecular Ion $H_2^+$. *J. Chem. Theory Comput.* **2018**, *14*, 5846–5858.
456. Coccia, E.; Luppi, E. Detecting the Minimum in Argon High-Harmonic Generation Using Gaussian Basis Sets. *Theor. Chem. Acc.* **2019**, *138*, 96.
457. Pauletti, C. F.; Coccia, E.; Luppi, E. Role of Exchange and Correlation in High-Harmonic Generation Spectra of $H_2$, $N_2$, and $CO_2$: Real-Time Time-Dependent Electronic Structure Approaches. *J. Chem. Phys.* **2021**, *154*, 014101.
458. Witzorky, C.; Paramonov, G.; Bouakline, F.; Jaquet, R.; Saalfrank, P.; Klamroth, T. Gaussian-Type Orbital Calculations for High Harmonic Generation in Vibrating Molecules: Benchmarks for $H_2^+$. *J. Chem. Theory Comput.* **2021**, *17*, 7353–7365.
459. Coccia, E.; Luppi, E. Time-Dependent *Ab Initio* Approaches for High-Harmonic Generation Spectroscopy. *J. Phys. Condens. Matt.* **2022**, *34*, 073001.
460. Zhu, Y.; Herbert, J. M. High Harmonic Spectra Computed Using Time-Dependent Kohn-Sham Theory With Gaussian Orbitals and a Complex Absorbing Potential. *J. Chem. Phys.* **2022**, *156*, 204123.
461. Kawashita, Y.; Nakatsukasa, T.; Yabana, K. Time-Dependent Density-Functional Theory Simulation for Electron-Ion Dynamics in Molecules Under Intense Laser Pulses. *J. Phys. Condens. Matt.* **2009**, *21*, 064222.
462. Tussupbayev, S.; Govind, N.; Lopata, K.; Cramer, C. J. Comparison of Real-Time and Linear-Response Time-Dependent Density Functional Theories for Molecular Chromophores Ranging From Sparse to High Densities of States. *J. Chem. Theory Comput.* **2015**, *11*, 1102–1109.
463. Repisky, M.; Konecny, L.; Kadek, M.; Komorovsky, S.; Malkin, O. L.; Malkin, V. G.; Ruud, K. Excitation Energies From Real-Time Propagation of the Four-Component Dirac-Kohn-Sham Equation. *J. Chem. Theory Comput.* **2015**, *11*, 980–991.
464. Kaduk, M.; Konecny, L.; Gao, B.; et al. X-Ray Absorption Resonances Near $L_{2,3}$-Edges From Real-Time Propagation of the Dirac-Kohn-Sham Density Matrix. *Phys. Chem. Chem. Phys.* **2015**, *17*, 22566–22570.
465. Bruner, A.; LaMaster, D.; Lopata, K. Accelerated Broadband Spectra Using Transition Dipole Decomposition and Padé Approximants. *J. Chem. Theory Comput.* **2016**, *12*, 3741–3750.

466. Rossi, T. P.; Kuisma, M.; Puska, M. J.; Nieminen, R. M.; Erhart, P. Kohn-Sham Decomposition in Real-Time Time-Dependent Density-Functional Theory: An Efficient Tool for Analyzing Plasmonic Excitations. *J. Chem. Theory Comput.* **2017**, *13*, 4779–4790.
467. Sinha-Roy, R.; García-González, P.; Lozano, X. L.; Whetten, R. L.; Weissker, H. C. Identifying Electronic Modes by Fourier Transform From $\delta$-Kick Time-Evolution TDDFT Calculations. *J. Chem. Theory Comput.* **2018**, *14*, 6417–6426.
468. Zhou, R.; Kanai, Y. Dynamical Transition Orbitals: A Particle-Hole Description in Real-Time TDDFT Dynamics. *J. Chem. Phys.* **2021**, *154*, 054107.
469. Fernando, R. G.; Balhoff, M. C.; Lopata, K. X-Ray Absorption in Insulators With Non-Hermitian Real-Time Time-Dependent Density Functional Theory. *J. Chem. Theory Comput.* **2015**, *11*, 646–654.
470. Li, D.; Bancroft, G. M.; Kasrai, M.; Fleet, M. E.; Secco, R. A.; Feng, X. H.; Tan, K. H.; Yang, B. X. X-Ray Absorption Spectroscopy of Silicon Dioxide ($SiO_2$) Polymorphs: The Structural Characterization of Opal. *Am. Mineral.* **1994**, *79*, 622–632.
471. Lopata, K.; Govind, N. Near and Above Ionization Electronic Excitations With Non-Hermitian Real-Time Time-Dependent Density Functional Theory. *J. Chem. Theory Comput.* **2013**, *9*, 4939–4946.
472. Yang, M.; Sissay, A.; Chen, M.; Lopata, K. Intruder Peak-Free Transient Inner-Shell Spectra Using Real-Time Simulations. *J. Chem. Theory Comput.* **2022**, *18*, 992–1002.
473. Fischer, S. A.; Cramer, C. J.; Govind, N. Excited-State Absorption From Real-Time Time-Dependent Density Functional Theory: Optical Limiting in Zinc Phthalocyanine. *J. Phys. Chem. Lett.* **2016**, *7*, 1387–1391.
474. Cavaletto, S. M.; Nascimento, D. R.; Zhang, Y.; Govind, N.; Mukamel, S. Resonant Stimulated X-Ray Raman Spectroscopy of Mixed-Valence Manganese Complexes. *J. Phys. Chem. Lett.* **2021**, *12*, 5925–5931.
475. Liekhus-Schmaltz, C. E.; Ho, P. J.; Weakly, R. B.; Aquila, A.; Schoelein, R. W.; Khalil, M.; Govind, N. Ultrafast X-Ray Pump X-Ray Probe Transient Absorption Spectroscopy: A Computational Study and Proposed Experiment Probing Core-Valence Electronic Correlations in Solvated Complexes. *J. Chem. Phys.* **2021**, *154*, 214107.
476. Loe, C. M.; Liekhus-Schmaltz, C.; Govind, N.; Khalil, M. Spectral Signatures of Ultrafast Excited-State Intramolecular Proton Transfer From Computational Multi-Edge Transient X-Ray Absorption Spectroscopy. *J. Phys. Chem. Lett.* **2021**, *12*, 9840–9847.
477. Liekhus-Schmaltz, C.; Fox, Z. W.; Andersen, A.; Kjaer, K. S.; Alonso-Mori, R.; Biasin, E.; Carlstad, J.; Chollet, M.; Gaynor, J. D.; Glownia, J. M.; Hong, K.; Kroll, T.; Lee, J. H.; Poulter, B. I.; Reinhard, M.; Sokaras, D.; Zhang, Y.; Doumy, G.; March, A. M.; Southworth, S. H.; Mukamel, S.; Cordones, A. A.; Schoelein, R. W.; Govind, N.; Khalil, M. Femtosecond X-Ray Spectroscopy Directly Quantities Transient Excited-State Mixed-Valency. *J. Phys. Chem. Lett.* **2022**, *13*, 378–386.